CHARACTERIZING EUKARYOTIC SINGLE CELL MOTILITY VIA BIMODAL ANALYSIS

By

Alka A. Potdar

Dissertation

Submitted to the Faculty of the

Graduate School of Vanderbilt University

in partial fulfillment of the requirements

for the degree of

DOCTOR OF PHILOSOPHY

in

Chemical Engineering

December 2009

Nashville, Tennessee

Approved:

Peter T. Cummings

Alissa M. Weaver

Clare McCabe

G. Kane Jennings

Scott A. Guelcher

To my parents, Suman and Anand Potdar

ACKNOWLEDGEMENTS

This work would not have been possible without the kindness and encouragement from several people. First of all, I would like to thank my doctoral advisor, Dr. Peter T. Cummings, for his guidance, encouragement and support throughout this research and giving me this opportunity. It has been truly a great learning experience having worked under his guidance, made enjoyable by his trademark humor and enthusiasm. I would like to thank all my other committee members, Dr. Clare McCabe, Dr. Scott Guelcher, Dr. Kane Jennings and Dr. Alissa Weaver for their kind help and guidance in this research work. I would like to thank Dr. Vito Quaranta for his encouragement and providing the resources for this research. A special thank you to Dr. Junhwan Jeon for his help and contribution to this research work.

I would like to thank all the current and past members of the Cummings Research Group and thanks to all the members of the Quaranta lab with whom I interacted while doing experiments. Thanks to fellow graduate students, Scott Gruver for his contribution to this research and Manisha Tripathi for helpful discussions. I thank the undergraduate students, Jenny Lu and Sesha Pinnaduwage for their help in the experiments.

Above all, I thank my family for their constant love and encouragement and supporting me in all my endeavors. Thanks to all my friends for their help and always being there for me in good and bad times.

Lastly, I would like to acknowledge the funding source, NCI grant: Multiscale Mathematical Modeling of Cancer Invasion. Grant number: 5U54CA113007-02

TABLE OF CONTENTS

Page

LIST OF TABLES

LIST OF FIGURES

CHAPTER I

INTRODUCTION

1.1 Overview

With the advent of new technologies in the field of life sciences, there has been an increasing emphasis on applying quantitative and mathematical approaches to biology and medicine in order to comprehend the vast amount of data generated. A successful solution to a problem relies upon a synergistic feedback between experimental and modeling approaches. Modeling cancer invasion is one example where the influence of several factors (such as cell phenotype (mutation, cell cycle stage), cell-cell adhesion, etc) in different manners needs to be considered. A particularly relevant example in relation to this thesis, in the realm of basic biology, is the phenomenon of cell migration. Cell motility (particularly, directed motility, such as, chemotaxis) is thought to be an essential element of metastasis, which is the prime cause of mortality and morbidity associated with cancer.

Cell migration research has evolved into a well-developed subject area with a steadily growing number of papers being published over years (Fig. 1.1), that include measurement of cell motility parameters for different cell lines, as well as mathematical modeling at scales ranging from sub-cellular motility (signaling networks); cellular and population levels. In this work, we have developed a cellular scale approach to study eukaryotic cell migration by performing a model-based analysis of single cell migration experimental data, which can then be used to predict population properties. The focus

will be on cellular-level migration with no particular emphasis on any sub-cellular or molecular detail. We have applied this analysis technique for both random and directed single cell migration in *amoeba* and in the process have tried to connect the two forms of motility that have often been studied separately. The phenotype-specific migration parameters of mammary epithelial cells were used to perform cellular dynamics simulations of these cells in order to predict population properties. Also, the search strategy of these cells in random motility conditions was explored to arrive at a bimodal-correlated random walk model. Lastly, the possibility of a temporal gradient sensing in mammary epithelial cells was briefly examined.

1.2 Biological background

1.2.1 Cell migration

1.2.1.1 Background

Cell migration is an essential phenomenon for both unicellular and multi-cellular organisms. Unicellular organisms [1, 2] such as *E.coli* or *Paramecium* frequently migrate by swimming through a fluid using flagella or cilia respectively or by crawling along surfaces using structures such as pseudopods as is the case in amoeba. The objective of migration for unicellular organisms could be simply survival by migrating towards some food source or away from harmful conditions or to escape from predators. In multicellular organisms, however, cell migration is a key element in complex behaviors depending on cell type, such as inflammation (migration of neutrophils), tumor metastasis (migration of tumor cells) and wound healing (migration of fibroblasts). This is illustrated pictorially in Fig. 1.2. The importance of cell migration in human body is

amply illustrated by Table 1.1 reproduced from [2] where the role of different cell types in specific physiological processes is listed. Of particular note is the process of embryogenesis where migrating embryonic cells lead to the development of structures within an embryo.

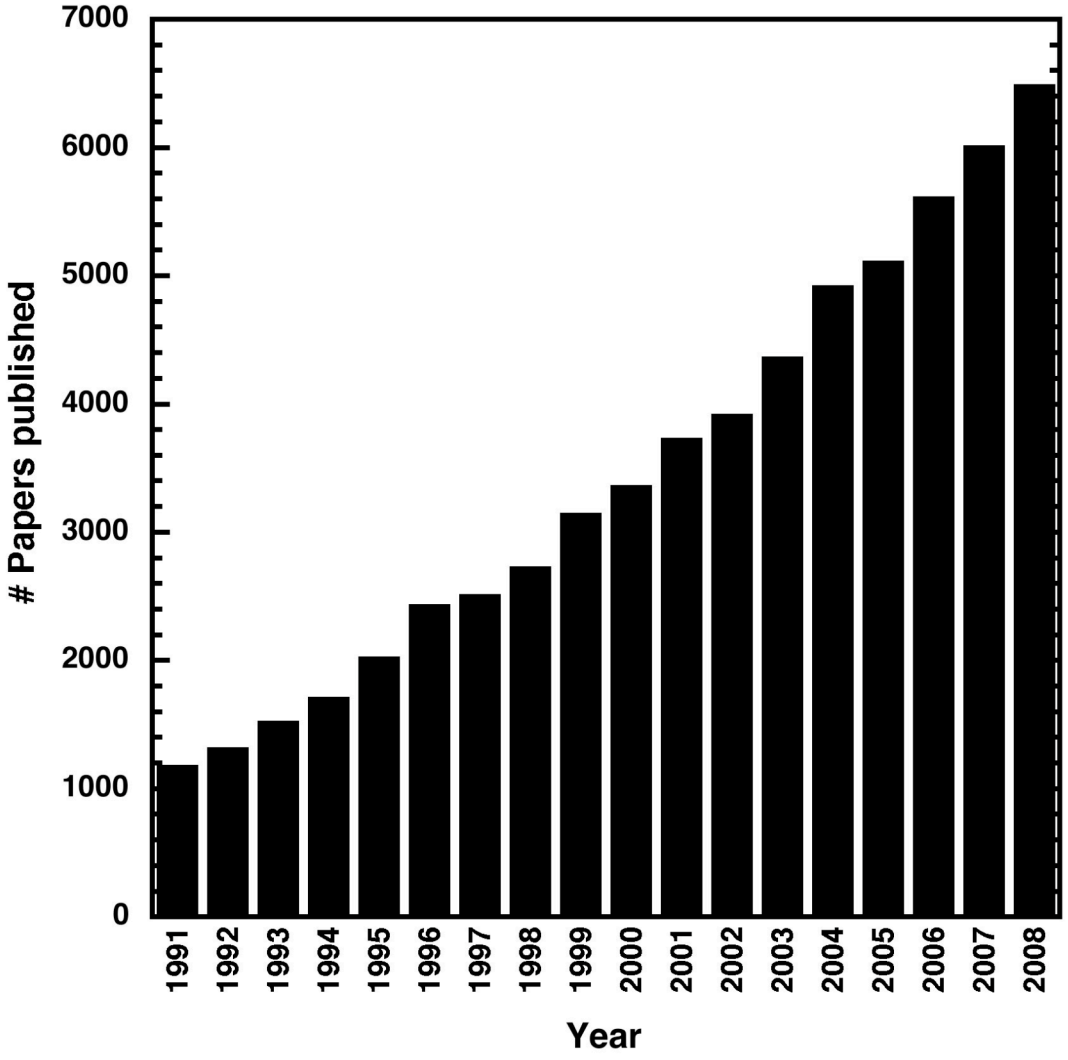

Figure 1.1 Number of publications with keyword, 'cell migration' or 'cell motility' from web of science indicating a steady increase in cell migration literature.

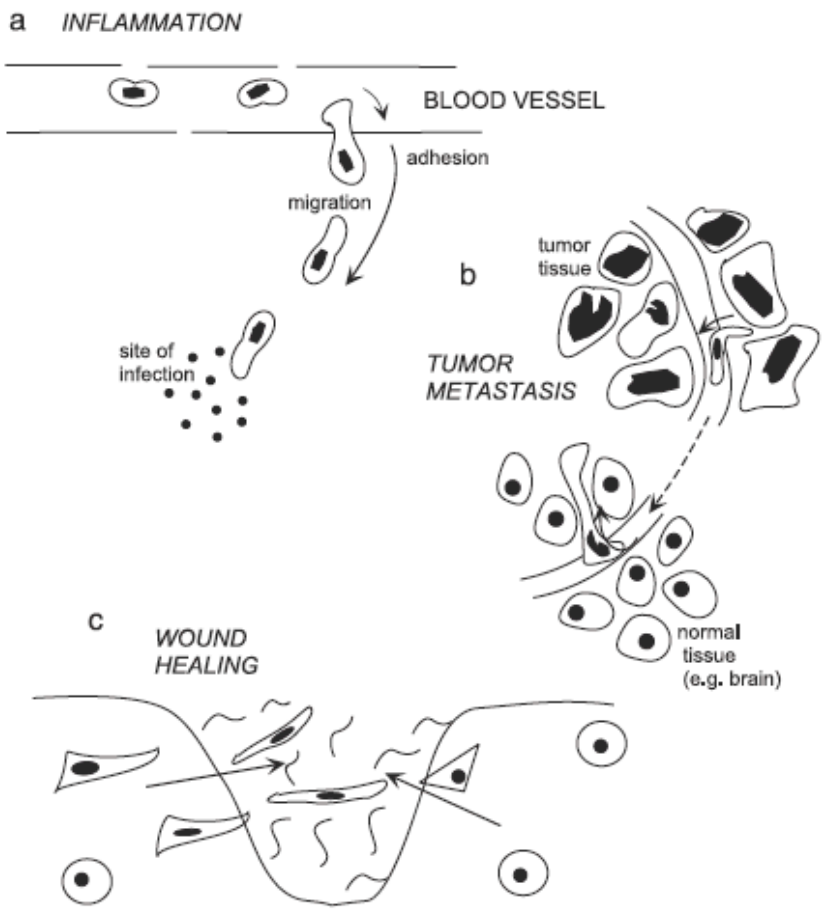

Figure 1.2 Role of cell migration in different physiological processes in eukaryotic cells [2]. Migration of a) neutrophils during immune response; b) tumor cells during metastasis and c) fibroblasts during wound healing.

Table 1.1: Importance of cell migration in human physiology[2].

Type of Migrating Cell	Role of Migrating Cell
Neutrophils	Phagocytosis of bacteria
Lymphocytes	Destruction of infected cells
Macrophages	Antigen presentation
Endothelial cells	Angiogenesis
Epidermal cells and fibroblasts	Wound healing
Tumor cells	Metastasis
Neurons and axons	Development and regeneration in the nervous system
Embryonic cells	Embryogenesis

1.2.1.2 Salient Features of eukaryotic cell migration

Eukaryotic cell migration is believed to be a "physically integrated molecular process", which is characterized by distinct features such as morphological polarization, membrane extension, formation and subsequent release of cell-substrate attachments and contractile and traction forces [3]. Much of this information comes from *in vitro* studies; however, it is thought to be useful in understanding *in vivo* characteristics. All of motile eukaryotic cells such amoeba, neutrophils, fibroblasts and epithelial cells share several general features (as mentioned above) with differences in cell-type specific motility (such as speed) arising as a result of differences in physico-chemical properties of the cell type.

Nonetheless, cell migration can be broadly thought of as a cyclic process that starts with polarization in the direction of migration by extension of membrane protrusions such as a broad lamellipodia or spike-like filopodia. Polarization results with a break in the cellular symmetry leading to a distinct cellular front and rear and this can happen even in homogeneous stimulus concentrations [4]. The membrane extensions have been associated with pronounced local actin polymerization and F-actin has been found to be distributed asymmetrically in a polarized cell [5] among other molecular asymmetries between back and front. The protrusions at the front are stabilized by attaching to the substrate underneath using receptors called integrins that facilitate adhesion to the extra-cellular matrix (ECM) by linking via adapters with actin filaments inside the cell [6]. Adhesions are formed at the rear too but preferentially located at the leading edge. Rapid migration requires efficient mechanisms to release the rear of the cell and could play an important role in the overall migration rate.

Apart from the protrusive forces provided by actin-polymerization at the front, the cell needs a contractile force to move the cell body forward that is believed to be provided by myosin-based motors. An illustration of various forces involved in a motile cell is shown in Fig. 1.3 adapted from the review by Lauffenburger *et. al.* [3]. The magnitude of traction is greater than the rearward contractive pull during translocation while during detachment of the rear, the magnitude of the traction is less than the contraction force.

Depending on the composition of the local environment, cells respond by modulating their migration pattern, exhibiting either directed or non-directed (i.e., random) migration. This is achieved via cell surface receptors that can bind to the soluble factors such as hormones, growth factors and nutrients or surface bound factors in ECM. Non-directed or random migration occurs if the composition of local vicinity is uniform. However, in the presence of any gradients (spatial or temporal) in the soluble or insoluble factors, cells move in response to the gradients by a process called taxis (i.e., the directed cell migration). A well-known example of directed migration is chemotaxis, which is the biased migration of cells in response to gradients of soluble attractants.

1.2.1.3 Experimental techniques

The importance of cell migration (as illustrated in Table 1.1) has led to many experimental studies. Various imaging techniques have been used to study cell migration *in vitro* as well as *in vivo* with newer microscopy techniques. Time-lapse microscopy of cells on 2-D substrates has been a popular method that permits the observation of cells over a long period of time (days). Unlike the end-point cell migration assays such as Boyden chambers [7] or filter assays, time-lapse videomicroscopy permits quantitative

analysis of individual cell movements. Newer imaging techniques such as 2-photon microscopy enables imaging of cells within thick specimens. MRI techniques have been used to track cells during embryogenesis [2]. Techniques such as confocal microscopy, FRAP (fluorescence recovery after photobleaching) and TIRF (total internal reflection microscopy) have been used to study the sub-cellular, cytoskeletal features of a cell [8].

1.2.2 Motivation

Apart from the normal physiological functions, studying cell migration is important to understand pathological conditions such as cancer. Cancer can be defined as a group of diseases that involve uncontrolled growth and spread of abnormal cells which if not controlled can lead to death. According to American Cancer society statistics [9], cancer is the second most common cause of death in the US after heart disease and about 1.43 million new cancer cases were expected to be diagnosed in 2008. One in two men and one in three women will get cancer in their lifetime and the overall cost burden for cancer in 2007 was estimated by the National Institutes of Health to be $219.2 billion.

Cancer metastasis (spread and eventual growth of cancer cells from primary tumors to secondary sites) resulting in secondary tumors is the main cause of morbidity and mortality associated with human cancer. The ability of invasive motility and metastasis is one of the hallmarks of cancerous cells [10]. The various steps involved in the metastatic process are: *angiogenesis* (formation of blood vessels) of the primary tumor; *intravasation* of tumor cells into the circulatory blood system directly (see Fig. 1.4) using the blood vessels or indirectly through the lymphatic system; *arrest* of these cells into a new organ and finally *extravasation* into the new tissue [11, 12].

Mathematical modeling is imperative for understanding the complex cancer invasion process that involves the impact of several factors often in competing ways. Cell migration is an essential aspect of cancer metastasis; cancer invasion has been found to be enhanced by chemotaxis (the directed movement of cells in response to a spatial gradient of a chemokine/growth factor) [13]. Highly metastatic cells are found to possess chemotactic properties in the presence of factors such as epidermal growth factor and certain chemokines such as the CXCL12 [14-16] ligand, which has the CXCR4 receptor. Hence, the inclusion of cell motility and the effect of chemotaxis are very essential in any model for cancer.

Individual cell migration has been found to play a crucial role in organ morphogenesis [17]. Tumor cells are also thought to frequently down-regulate their cell-cell adhesions via epithelial-mesenchymal transition and migrate as individual cells during tumor metastasis [18]. In addition, understanding how cells behave on an individual level is also an essential element in predicting their population-level behavior. For example, the transport properties from the individual cellular level have been correlated to those at the population level [19-21] for both random and biased cell migration of bacteria and leukocytes. The knowledge of single cell level parameters in the presence and absence of chemo-attractants thus could be useful in quantifying the subtle differences in cell motility arising due to different genetic makeup such as comparing the invasive abilities of malignant cells compared to normal cells. The individual chemotactic parameters can then be included in existing mathematical models of cancer invasion such as the hybrid-discrete-continuous Anderson model [22, 23] to develop more realistic models of cancer invasion.

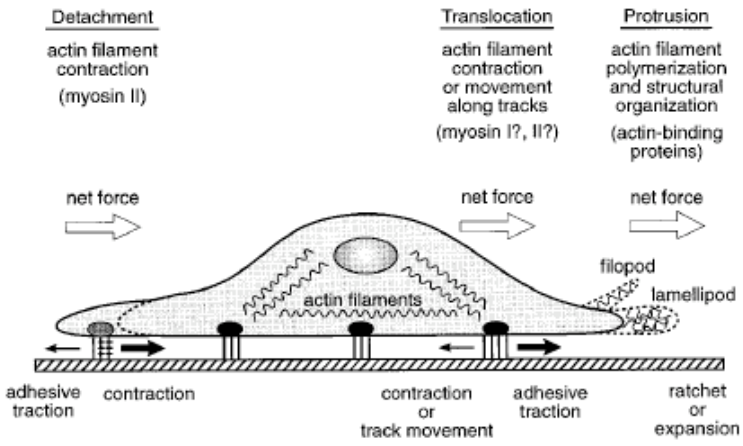

Figure 1.3: The different forces involved during cell migration that result in the protrusion, translocation and detachment cycle for a motile cell [3].

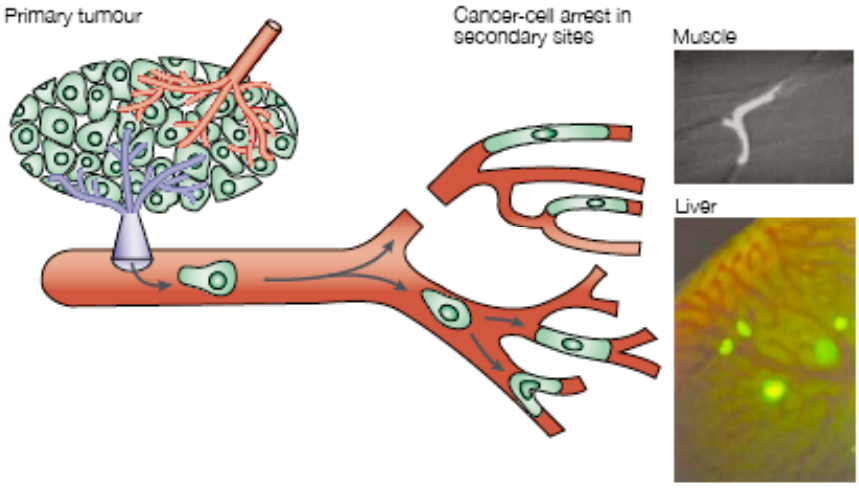

Figure 1.4: The metastatic process via blood circulation where cells from the primary tumor get arrested by size restriction in small capillaries of new organ [11].

1.3 Physical background

Random walk theories have been applied to model migration of cells because of resemblance to the random paths of particles in Brownian motion. Diffusion is the inherent random migration of particles due to thermal energy. Einstein showed that for a particle moving in one direction at an absolute temperature of T, the associated kinetic energy is $kT/2$, where k is the Boltzmann constant. We know that average kinetic energy associated with a particle of mass m and velocity v is $\langle mv^2/2 \rangle$, hence $kT = m\langle v^2 \rangle$ in one dimension. In N dimensions, the relationship is $NkT = m\langle v^2 \rangle$.

Non-directed cell migration is often described as a persistent random walk motion (PRW) [24] which is emergent from the Langevin equation [2, 25]:

$$m\frac{d\vec{v}(t)}{dt} = -\xi\vec{v}(t) + \vec{f}(t), \tag{1.1}$$

where m is the mass of a single cell, $\vec{v}(t)$ is the cell velocity, ξ is an effective friction coefficient, and $\vec{f}(t)$ is random force acting on the cell. The first term on the right-hand side denotes the friction force, which the cell experiences due to the motion in a given medium. The second term denotes the random stochastic force which has two characteristic properties: (i) a mean of zero $\langle \vec{f}(t) \rangle = 0$; and ($ii$) δ-function correlations, $\langle \vec{f}(t) \cdot \vec{f}(t') \rangle = 2N\xi kT\delta(t - t')$ [25], where k is the Boltzmann constant, T is the absolute temperature, and N is the dimensionality.

Uhlenbeck and Ornstein [26] showed that mean-squared displacement (MSD), $\langle d(t)^2 \rangle$, can be obtained by integrating the simplified stochastic differential equation (1.1) to yield the following equation in one dimension (N=1):

$$\left\langle d(t)^2 \right\rangle = \frac{2mkT}{\xi^2}\left(\frac{\xi}{m}t - 1 + \exp\left(-\xi t/m\right)\right). \tag{1.2}$$

Using the equipartition theorem, $kT = m\left\langle v^2 \right\rangle$ for N=1, and redefining m/ξ as P, we obtain a following equation:

$$\left\langle d(t)^2 \right\rangle = 2\left\langle v^2 \right\rangle P\left(t - P + P\exp\left(-t/P\right)\right), \tag{1.3}$$

Where P is the persistence time.

1.3.1 Diffusive motion

A pure random walk with diffusive motion is characterized by MSD increasing linearly with time. This relationship can be derived in the asymptotic limit as $t \to \infty$ in equation 1.3, giving $\left\langle d(t)^2 \right\rangle = 2\left\langle v^2 \right\rangle Pt = 2Dt$ where $D = \frac{\left\langle v^2 \right\rangle P}{N(=1)}$; is the diffusion coefficient in 1-D and N is the number of system dimensions. This relation can also be derived as follows [1, 27]: A one-dimensional random walk can be assumed for simplicity as illustrated in Fig. 1.5. Let a population of particles/cells diffuse out along a linear path from a same point, c. At each time point, τ, each particle moves either to left or right with equal probability by a distance δ. Let d_n be the distance of the particle from its starting point c after n steps, then

$d_n = d_{n-1} \pm \delta$. Squaring both sides gives,

$d_n{}^2 = d_{n-1}{}^2 + 2d_{n-1}\delta + \delta^2$ and $d_n{}^2 = d_{n-1}{}^2 - 2d_{n-1}\delta + \delta^2$

Averaging, the two values of $d_n{}^2$ over a large population of similar particles, the terms of the form $\pm 2d_{n-1}\delta$ would cancel out as the steps taking on both sides have equal probability. Hence the MSD after n steps is given by,

$$\left\langle d_n^{\,2} \right\rangle = \left\langle d_{n-1}^{\,2} \right\rangle + \delta^2$$

If the cells start at $c = 0$, $\left\langle d_0^{\,2} \right\rangle = 0; \left\langle d_1^{\,2} \right\rangle = \delta^2; \left\langle d_2^{\,2} \right\rangle = 2\delta^2; \left\langle d_3^{\,2} \right\rangle = 3\delta^2$
$\left\langle d_n^{\,2} \right\rangle = n\delta^2$

Since, $t = n\tau$, for any time t,

$$\left\langle d_t^{\,2} \right\rangle = (t/\tau)\delta^2 = (\delta^2/\tau)t \tag{1.4}$$

Substituting, $D = \delta^2/2\tau$, where D is the diffusion coefficient of the particle in equation 1.4,

$$\left\langle d_t^{\,2} \right\rangle = 2Dt \tag{1.5}$$

From equation 1.5, we can see that for a purely diffusive system the MSD is proportional to time. Hence, on a log-log scale, on plot of MSD versus time, a slope of 1 would indicate a diffusive regime. This linear regime can be used to estimate the diffusion coefficient, D. For a two and three-dimensional system, equation 1.5 can be written as, $\left\langle d_t^{\,2} \right\rangle = 4Dt$ and $\left\langle d_t^{\,2} \right\rangle = 6Dt$ respectively.

The MSD in equation 1.5 can also be derived by using the second moment of a Gaussian distribution, $p(x)$, $\left\langle d_t^{\,2} \right\rangle = \int_{-\infty}^{\infty} x^2 p(x)dx$. The scatter probability of particles in 1-D diffusive random walk starting from origin, is given by a Gaussian distribution with mean zero given by the following equation:

$$p(x) = \frac{1}{\sigma\sqrt{2\pi}} \exp\left(-\frac{(x)^2}{2\sigma^2}\right);$$

where the standard deviation $\sigma = \sqrt{2Dt}$ is root MSD that increases as the square root of time.

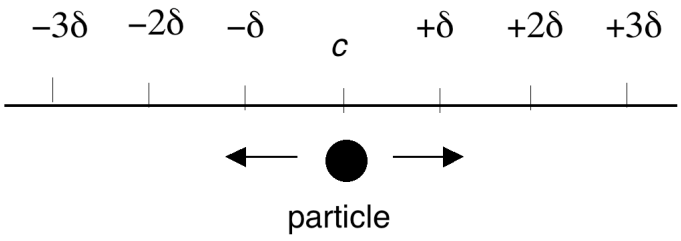

Figure 1.5: A one-dimensional random walk in which a particle starts from c and moves a distance of $+\delta$ or $-\delta$ at each step.

1.3.1 Ballistic motion

A ballistic motion is a case of anomalous diffusion that arises in the short-time regime where MSD increases as square of time and there is significant correlation in successive steps taken by a particle. On a log-log scale, a plot of MSD versus time would give a signature slope of 2. This relation can be derived from equation 1.3 for times much less than the persistence time ($t << P$).

Equation 1.3 can be written as $\left\langle d(t)^2 \right\rangle = 2\left\langle v^2 \right\rangle P\left(t - P + P(1 - t/P + t^2/2P^2)\right)$ by considering the first three terms of exponential series expansion as the higher terms can be ignored for $t << P$. The above equation then reduces to:

$$\left\langle d(t)^2 \right\rangle = \left\langle v^2 \right\rangle t^2 \tag{1.6}$$

Equation 1.6 is true for the short-time ballistic regime for any dimensionality with the square of the speed as the proportionality constant.

1.4 Research outline

1.4.1 Focus

The focus of this work is to model single cell migration of eukaryotic cells. Other phenomenon such as cell adhesion and cell division are excluded from the experimental data considered here. The dissertation research reported here has three main aspects. The first is the development of a simple model-based analysis method (*bimodal analysis)* for characterization of single cell migration data (presented in Chapter II).

The second aspect is to model mammary epithelial single cell migration (using the results from Chapter II) using the cellular dynamics simulation methodology (discussed in Chapter III) and also using a bimodal-correlated random walk model (Chapter IV). In Chapter IV, the search strategy of individual epithelial cells is also discussed.

The third aspect deals with application of bimodal analysis tool to various cell types in different motility assays/treatments to provide a common framework for studying eukaryotic single cell motility (application in Chapters V, VI and VII). A simple experimental setup for creating temporal gradients for epithelial cells is discussed in Chapter VI and the possibility of temporal gradient sensing by epithelial cells is investigated. The main conclusions and future directions are discussed in Chapter VIII.

1.4.2 Objectives

1. To develop a 'bimodal analysis' framework for mammalian cells inspired from bacterial migration and extract single cell dynamics of mammalian cells from the experimental cell tracking data of cells migrating in random motility conditions. (Covered in Chapter II).

2. To model mammary epithelial single cell migration using:
    a) The 'cellular dynamics' simulations for the motion of MCF-10A cells using the parameters extracted by bimodal analysis. The initial step was to develop simulations with negligible re-orientation time (same as the bacterial scenario) and then incorporate finite re-orientation time, i.e., a re-orientation phase corresponding to directional changes in the mammary epithelial cell path. The goal is to characterize random motility of the MCF-10A, Her-2 transformed cell lines on 2-D substrates. The outcomes from such an analysis would help differentiate between the benign and invasive cells. (Covered in Chapter III).
    b) The 'bimodal correlated random walk' model parameterized by the results obtained from bimodal analysis. The search strategy of migratory epithelial cells was examined using survival frequency plots, logarithmic binning with normalization and maximum likelihood estimates. A comparison with persistent random walk model is also made. (Covered in Chapter IV).
3. Application of bimodal analysis to different cell types in various treatments (directed migration) and assays.
    a) Application to wild type and several *Dictyostelium* mutants in vegetative, developed and chemotaxis (micropipette and microfluidic chambers) assays. The common framework of bimodal analysis was used to study motility in eclectic range of eukaryotic cells (*Dictyostelium,* neutrophils, fibrosarcoma and human mammary epithelial cells). This was done in

collaboration with Scott Gruver (Chung lab, Department of Pharmocology). (Covered in Chapter V).

b) Application to migration of MCF-10A cells (pBabe, neuN and neuT) in temporal gradients of EGF (Covered in Chapter VI).

c) Application to wild type and mutant prostrate cancer cells (low matriptase-expressing LNCaP cells and matriptase-overexpressing LNCaP cells) migrating on laminin-332. This was done in collaboration with Manisha Tripathi (Quaranta lab, Department of Cancer Biology). (Covered in Chapter VII).

CHAPTER II

BIMODAL ANALYSIS OF MAMMARY EPITHELIAL CELL MIGRATION

2.1 Abstract

Cell migration paths of mammary epithelial cells (expressing different versions of the promigratory tyrosine kinase receptor Her2/Neu) were analyzed within a bimodal framework that is a generalization of the run-and-tumble description applicable to bacterial migration. The mammalian cell trajectories were segregated into two types of alternating modes, namely, the "directional-mode" (*mode I*, the more persistent mode, analogous to the bacterial run phase) and the "re-orientation-mode" (*mode II,* the less persistent mode, analogous to the bacterial tumble phase). Higher resolution (more pixel information, relative to cell size) and smaller sampling intervals (time between images) were found to give a better estimate of the deduced single cell dynamics (such as directional-mode time and turn angle distribution) of the various cell types from the bimodal analysis. The bimodal analysis tool permits the deduction of short-time dynamics of cell motion such as the turn angle distributions and turn frequencies during the course of cell migration compared to standard methods of cell migration analysis. We find that the two-hour mammalian cell tracking data do not fall into the diffusive regime implying that the often-used random motility expressions for mammalian cell motion (based on assuming diffusive motion) are invalid over the time steps (fraction of minute) typically used in modeling mammalian cell migration.

2.2 Background

Cell migration is of crucial importance in cells ranging from simple bacteria to complex mammalian cells. Bacteria migrate towards a food source or move away from unfavorable environments [1] while eukaryotic cell migration forms the basis of many normal physiological processes such as embryogenesis [28] as well as pathogenic conditions like tumor metastasis [11, 12]. Individual cell migration has been found to play a crucial role in organ morphogenesis [17]. Tumor cells are also thought to frequently down regulate their cell-cell adhesions and migrate as individual cells during tumor metastasis [18]. In addition, understanding how cells behave on an individual level is an essential element in predicting their population-level behavior. The information of single cell level parameters can be useful in quantifying the subtle differences in cell motility arising due to different genetic makeup such as comparing the invasive abilities of malignant cells compared to normal cells.

The motion of an individual bacterium has been well described by a run-followed by-tumble framework [1, 29, 30]. The runs last for several seconds while tumbles last for a fraction of a second (~ 0.1s). The tumbling phase involves the reversal of the bacterial flagella from anticlockwise to clockwise, at which point forward motion of the cell comes to an end. After re-orientation, the flagella again revert to anticlockwise rotation, and the bacterium starts to move in a new direction. Berg's tracking microscope [29] has been used to follow bacteria rigorously as they migrate and 'run and tumble' parameters have been determined for *E. coli* both in the presence and absence of a chemoattractant [29]. A clear criterion was developed to identify the 'runs and tumbles' in bacterial motion and used to develop run time, tumble time and turn angle distributions for the bacteria from

the tracking data [29, 31]. This framework was extended for tracking migration of *E. coli* near solid planar surfaces [32] and study migration of other bacteria such as *Pseudomonas putida* [33, 34].

The incorporation of single-cell dynamics into a model for cell populations has been successfully done in the past for bacteria using the 'cellular dynamics' simulation methodology [35, 36] which will be discussed in the following Chapter. In order to extend this scheme to eukaryotic cells, similar parameters need to be extracted from the mammalian cell tracking data; the first step in doing so is to characterize the cell motion in the absence of a chemoattractant.

The bimodal model for mammalian cell motility, presented for the first time in the literature [37], contrasts with the persistent random walk (PRW) model that is based on a continuum version of Ornstein-Uhlenbeck process used to describe Brownian dynamics. The PRW model has been often used to study the motility of individual mammalian cells [38]. In the PRW model, a non-linear equation-involving mean squared displacement of the cell as a fit of two parameters namely, the mean speed and persistence time, is used to model the migration of mammalian cells [39]. The persistence time is described as a characteristic run-time incorporating the persistence displayed by a cell [40]. Several investigators have used this model to fit the time-lapse video-microscopy cell migration data and extract cell-specific parameters such as persistence time [24, 38, 41-51]. However, information regarding the short-time dynamics such as the turn angle distribution and turn frequency as the cell migrates cannot be deduced from the PRW model.

The availability of excellent data for the migration of individual bacteria over frequent sampling time intervals as well as the relatively faster time scale over which bacteria migrate have facilitated good characterization of bacterial motion in terms of run time (Poisson) and turn angle distributions. The tracking data of mammalian cell migration has been largely confined to taking frequent snapshots of a fixed field of view over several time points. The migrating cell must remain in this field of view for this purpose, unlike the three-dimensional tracking of bacteria where a given individual bacterium was tracked automatically so that it always remained in the center of the field of view. Some attempts have been made at modifying the tracking software to keep a given mammalian cell within the field of view [52] but fixed time-lapse video-microscopy still remains the most popular method to track mammalian cells on 2-D substrates in order to get cellular parameters [53, 54]. The 3-D tracking of mammalian cells (15-20 μm) is difficult to assess compared to the 3-D visualization of smaller-in-size bacterial cells (1 μm). Our experimental capabilities restrict us to collecting fixed time-lapse microscopy data of mammalian cells on 2-D tissue culture plastic substrates and we developed an analysis tool based on this data.

In this work, we have approached the problem of analyzing cell migration of individual mammalian cells, specifically MCF-10A cells (human mammary epithelial cells), within a bimodal (directional and re-orientation modes) framework similar in spirit to that used in the analysis of bacterial motility [29, 31]. We interpret the re-orientation phase in a mammalian cell migration as the time during which the actin polymerization machinery in the cell preferentially polymerizes actin at a new leading edge and the cell is propelled in the new direction [1, 55]. The cellular activity of proteins like Rac has

been found to regulate the random versus directionally persistent mode of migration in a cell [56]. The role of phosphoinositide (PI)-3 kinase signaling in actin motility in various chemotactic systems from *Dictyostelium discoideum* to fibroblasts has been discussed where directional bias in eukaryotic cells is said to arise due their spatial sensing of chemo-attractant gradients leading to heterogeneous distribution of this signaling [6, 57]. An attempt is made here to separately locate the directional-mode (mode I, the more persistent mode) analogous to a bacterial run and the re-orientation-mode (mode II, random or the less persistent mode) analogous to a bacterial tumble in a mammalian cell migration path by performing simple video-microscopy experiments.

A criterion for locating runs and tumbles in a cellular trajectory based on work by Berg and coworkers with bacterial migration was applied to MCF-10A cellular trajectories. Using this criterion, the turn angle distributions of control MCF-10A-pBabe, pre-malignant neuN and invasive neuT were generated. The single cell dynamics such as the mean directional-mode time, re-orientation-mode time and turn angle distributions were extracted for the MCF-10A cells from the tracking data. We have further discussed the effect of the sampling time interval of experimental data collection and also the resolution at which the data is collected.

2.3 Materials and methods

2.3.1 Cell culture

The cell lines used in the motility experiments were a kind gift of Dr. Joan Brugge and were derived from the MCF-10A human mammary epithelial cells to express the pBabe vector alone (pBabe), or the normal (neuN) or transforming (neuT) versions of the rat

Her 2/Neu oncogene [58, 59]. All the cells were cultured in DMEM/F-12 50/50 media (Mediatech, Herndon, VA) supplemented with horse serum (2%, GIBCO/Invitrogen, Carlsbad, CA), cholera toxin (0.1μg/mL, Calbiochem, La Jolla, CA), insulin (10μg/mL, GIBCO/Invitrogen, Carlsbad, CA), hydrocortisone (0.5μg/mL, Sigma, St. Louis, MO) and EGF (20ng/mL, GIBCO/Invitrogen, Carlsbad, CA) as described by protocol in work by Debnath and coworkers [60]. The cells were maintained in a humidified atmosphere supplemented with 5% CO_2 and were split every 3 to 4 days.

2.3.2 Cell motility assay

The migration of cells was followed under random motility conditions without the presence of any externally added chemo-attractant gradients. All the three cell types were plated overnight at a low density of approximately 5000 cells per cm^2 of growth area on tissue-culture plastic. The media was changed to Leibovitz's L-15 (GIBCO/Invitrogen, Carlsbad, CA) medium (because of an absence of CO_2 buffering in the microscope chamber) supplemented with horse serum (2%), cholera toxin (0.1μg/mL), insulin (10μg/mL), hydrocortisone (0.5μg/mL) and EGF (20ng/mL).

The cells were monitored using the phase-contrast optics in a Nikon Eclipse TE2000-E microscope equipped with temperature-controlled, humidified chamber and a motorized x-y stage for several samples. Cellular images were captured on a Hamamatsu Orca-ER camera using MetaMorph (Molecular Devices Corporation, Sunnyvale, CA) for data acquisition and analysis. The cells were followed with a magnification of 40x (1 pixel ≡ 0.163 μm) and a sampling time interval of 0.5 minutes. Figure 2.1 shows a frame of MCF-10A-neuT cells viewed at different resolutions of 10x (1 pixel ≡ 0.647 μm) and 40x (1 pixel ≡ 0.163 μm). All the cells were equilibrated in the humidified, temperature

controlled (37 ^{0}C) microscope chamber for an hour before data collection. The cells were followed for at least two hours in all the experiments. At least five sets of experiments were performed and on an average four movies were taken per well. We used a shorter time period of 2 hours for a smaller sampling time interval of 0.5 minutes because of constraints imposed by the available experimental set-up for data storage. We reduced the total time of the video-microscopy to 2 hours to opt for the more frequent sampling of data. Experiments have also been performed using this apparatus over longer periods with less frequent sampling; however, we do not use this experimental data for analysis in this work.

2.3.3 Trajectory data

Each cell was manually tracked by following the cell nucleus. Only single cells that never interacted with other cells were considered for the analysis. The cells were plated at low density to avoid interacting cell populations. Cells that remained stationary, or moved outside the viewing area, or that underwent cell division during the course of the experiment were excluded from the tracking procedure. A heuristic rule was used to further screen the data to be used for the analysis. A cell that did not cover considerable distance (at least 30 μm along one axis) was considered atypical, and thus not included in our analysis. Approximately, 50% of total tracked cells for each cell type fit this heuristic criterion. To address the impact of sampling frequency, the 0.5 minute data obtained using 40x was re-analyzed as 2.5 minute data by considering every fifth data point. This means that each trajectory at 0.5 minutes generates 5 trajectories at 2.5 minutes: one trajectory using the 1st, 6th, 11th, … positions, one using the 2nd, 7th, 12th,… positions, etc. In order to address the impact of resolution, we extracted 10x data from 40x data, which

we refer to as‘10x extracted data’. For this, the pixels at 40x are converted to the values they would have at 10x followed by computing the co-ordinates of the cell at 10x (by using the calibration at 10x (1pixel ≡ 0.647 μm)). That is, 16 pixels at 40x collapse to a single pixel at 10x.

2.3.4 Bimodal analysis

The individual cell paths from the motility assay were first plotted as wind rose (the origins of the trajectories are shifted to (0,0)) [50] plots on a constant plot area (200 μm X 200 μm). Example cell trajectories used in the analysis are shown in Figs. 2.2 a, b and c. The cell paths with repeated circular tracks were ignored as these cells were found to undergo division.

The method employed to determine the direction change (ϕ) at each frame (time point) required for the ‘bimodal analysis’ is illustrated in Fig. 2.2d. The direction change at each frame is defined as the difference in forward direction and the backward direction. At each frame, the change in direction of motion was determined by finding the forward direction and backward direction. The forward direction is determined from the slope of a vector formed from the current frame to the successive frame while the backward direction is given by the slope of a vector from the prior frame to the current frame. A two-point linear regression was used to determine each slope. A negative direction change represents a clockwise motion and vice-versa. The analysis of the two-dimensional (x-y) data gives a direction change (ϕ) range from $-\pi$ to $+\pi$.

Since the time between observations is fixed, the change of ϕ between one frame and the next is essentially the same as the angular speed (the time-rate of change in direction of motion) that was computed by Berg and co-workers in the run-tumble

analysis of bacterial migration [29]. The rules for scoring the start and an end of a directional phase were similar to the ones used in the run-and-tumble analysis of bacterial paths and have been elaborately stated for the analysis of the three-dimensional tracking data for *E. coli* [31]. The following algorithm was used to locate the directional and re-orientation modes in a cellular trajectory. Specifically, the start of the directional mode was scored at any frame J if the quantity ϕ was less than an empirical cut off value, say, ϕ_{cut}, for frames J, J+1 and J+2 each. The end of the directional mode (start of the re-orientation mode) was scored at any frame J under two circumstances: a) if $\phi > \phi_{cut}$ for both frames J and J+1 or b) if $\phi > \phi_{cut}$ for frame J only, provided that the value of ϕ for vectors formed by data points J, J+2 in forward direction and J, J-2 in the backward direction is greater than ϕ_{cut}. We call this as r3 criterion since the ϕ value at three successive frames determine a directional mode. Analogously, we can also define an r2 criterion, in which the ϕ value at two successive frames determine the start of a directional mode, and an r1 criterion in which the ϕ value at a single frame was examined to score the start of a directional mode.

A cut-off value of $\phi_{cut} = 35°$ was used in the run-tumble analysis of bacteria [31]. A visual inspection of several cellular trajectories of the three MCF-10A cell types revealed that a cut-off value of $\phi_{cut} = 45°$ for ϕ was appropriate for locating the transition between two mode types in the epithelial cellular trajectories. A value less than this cut-off (such as $\phi_{cut} = 35°$) would pick up fluctuations in the cell path as the start of a directional mode as indicated (by the square inset) in an example trajectory (Fig. 2.3a). The same trajectory (a neuT cell path) with $\phi_{cut} = 45°$ is shown in Fig. 2.3b. This cut-off value is heuristic in nature and may or may not be applicable for other cell types. A good

starting point to empirically determine the value of ϕ_{cut} is 35^0 as this is the value by which bacteria would change its direction due to Brownian motion [31].

The turn angle in a cell trajectory is the angle change between successive directional modes. A procedure similar to the one described above to calculate ϕ was used to determine the turn angle with the exception that, instead of performing two-point linear regression to determine the slope (and hence direction) along a directional mode, a multi-point linear regression was performed utilizing all the data points constituting a directional mode.

2.3.5 Statistical Analysis

The statistical significance was verified using SPSS, version 16 (SPSS, Inc., Chicago, IL). The Shapiro-Wilks test for normality ($\alpha = 0.05$) was applied to all data sets for distribution analysis. The Kolmogorov-Smirnov two-sample non-parametric test was subsequently applied to data to check for significant differences ($\alpha = 0.05$) across means of various groups (i.e., by pixel size, sampling interval) for all measurements. While reporting the mean values (speed, directional-mode times and re-orientation-mode times), the mean of each cell was weighted equally [29], and the standard deviation (error bars in all Figs. and Tables) is the standard deviation in the mean. At least 5 independent experiments were carried out for each cell type. The persistence index ψ value does not have any error bars as this value was calculated using equation 2.1 ($\psi = 2\int_0^{\pi} h(\phi)\cos(\phi)d\phi$) where $h(\phi)$ is the turn angle distribution for a population of specific cell type computed from data from all independent experiments. The value of ψ was one value representing a population type hence it does not have a p-value.

2.4 Results

The d/t ratios for the two modes of MCF-10A cell migration were calculated to verify the presence of the directionally persistent (mode I) and re-orientation (mode II) phases. These ratios have been referred to as the directionality ratios in literature [56]. The quantity 'd' is the shortest linear distance from start to the end of a particular mode I or mode II, while 't' is the total distance traversed by the cell from start to the end of that particular mode I or II (Fig. 2.4). The mean d/t ratio obtained during the mode I phase (analogous to runs) was found to be higher ($p < 0.001$ for all cell types, pBabe (n=214), neuN (n=187) and neuT (n=169)) than the mean d/t ratio during the mode II phase (analogous to tumbles) confirming the existence of two alternating modes in eukaryotic cell migration.

A point of difference between the proposed bimodal framework for a mammalian cell versus the run-tumble framework for a bacterium is the timescale of the re-orientation-mode (mode II), which is analogous to the tumble mode of a bacterium. The time spent in the tumble phase in a bacterial trajectory is on the order of 0.1 seconds, compared to a run that lasts for seconds or longer, i.e., the timescales differ by at least one order of magnitude. On the other hand, we find that the re-orientation-mode in a mammalian cell trajectory can last for several minutes. A bacterial tumble could be considered essentially instantaneous unlike the re-orientation phase in a cellular trajectory where the re-orientation-mode can last as long as directional-mode. The turn frequency for bacteria is simply the number of tumbles made by the bacteria divided by the total time. The turn frequency for a mammalian cell is defined as the total number of re-

orientation-modes divided by the total time spent in the directional-modes. For a single cell, this definition is the reciprocal of the mean directional-mode time for the cell.

$\left\langle t^{run} \right\rangle = \frac{1}{N}\sum_{i=1}^{N} t_i^{run}$ and $\left\langle f^{turn} \right\rangle = \frac{1}{N}\sum_{i=1}^{N} \frac{1}{t_i^{run}} = \frac{1}{N}\sum_{i=1}^{N} f_i^{turn} \neq \frac{1}{\left\langle t^{run} \right\rangle}$ where t_i^{run} and f_i^{turn} are the mean directional-mode time and mean turn frequency of the i^{th} cell, respectively, N total number of cells in a cell type and the brackets denote average value of quantities for a given cell type.

A representative distribution of direction change at each sampling point, that is, ϕ values obtained using the bimodal analysis (described in the methods section) is shown in Fig. 2.5. For the two-dimensional system under consideration, the range of ϕ lies between $-\pi$ to $+\pi$ as mentioned earlier. For a 3-D tracking data, this range would be between 0 to π [29]; however, in 3D the direction at each time point would be characterized by two types of angles. In a 3-D *in vivo* setup, the influence of the ECM (extra-cellular matrix) overlaid on the cells would come into picture. It can be expected that the frequency of re-orientations may be altered in 3-D. The algorithm described in the methods section was used to locate the two modes along a cell path in multiple cell trajectories. Using the cut-off of $\phi_{cut} = 45°$, and applying the 'r3 criteria' described in methods section, the start and end of a mode I for each of the directional-modes in a cell trajectory can be located. We find that there was approximately equal occurrence of a cell-entering mode II via any of the two described mode II criteria.

After locating the direction along each mode I using multi-point regression, the "mode I to mode I" turn angle distribution for each cell type can be determined by making a histogram of turn angles for a given cell type. One such turn angle distribution

(neuT cells), which essentially represents the change in direction between successive directional modes in a mammalian cell trajectory, is shown in Fig. 2.5. Representative directional-mode time and re-orientation-mode time distributions (pBabe cells) are displayed in Fig. 2.6. It can be seen that the smallest directional-mode time is of the order of 1.5 minutes as constrained by the criterion for location of this mode while the re-orientation-mode lasts at least for 0.5 minutes in accordance with the second re-orientation criterion listed in the methods section. The highest probability of directional-mode and re-orientation-mode times for the pBabe cells was around 2 minutes.

All the distributions are discrete probability distributions determined from the frequency distribution of the variables. The cell trajectory data at a sampling time interval ($\Delta t_{\exp}$) of 0.5 minutes and 40x magnification were used to construct the distributions shown in Figs. 2.5, 2.6 and 2.7. All the results shown here were obtained using r3 criteria and a $\phi_{cut} = 45°$. The location of the two alternating modes using bimodal analysis and hence directional-mode time, re-orientation-mode time and turn angle distributions are weakly sensitive to the criterion and the value of ϕ_{cut} used for the bimodal analysis.

Figure 2.7a compares the turn angle distributions for the three different cell types while the directional-mode time and re-orientation-mode time distributions are plotted in Fig. 2.7b and 2.7c respectively. The cumulative distribution functions of these turn angle distributions can be fitted and used to perform cellular dynamics simulations of the different cell types and elucidate the differences in the cell lines.

The turn angle distribution $h(\phi)$, of a bacterium could be used to calculate (equation 2.1) the persistence index (ψ) (defined as the mean of cosine of deviation in a cell path which is same as the mean cosine of the turn angle distribution [40]) since the

bacterial tumbles are instantaneous and bacterial motion can be generalized as a velocity-jump process with no relaxation time [40]. A value of ψ close to 1 indicates high persistence while a value close to 0 indicates random behavior. The PRW model (equation 2.2) occasionally used to fit mean squared displacement ($d^2(t)$) of mammalian cells using the parameters of persistence time (P) and random motility coefficient (μ), for a system with n dimensions, is based on negligible re-orientation/tumbling time which may not be true in the migration of mammalian cells such as the MCF-10A cells as has been shown in the results. Equation 2.3 connects the random motility coefficient μ, to P and mean speed S. The persistence time is related to the persistence index, ψ in this model by equation 2.4 where $<\tau>$ is the mean directional-mode time. We have used equation 2.1 to calculate ψ just to elucidate the effect of various conditions such as the sampling interval and resolution and we recognize that MCF-10A random migration is a velocity jump process with a finite resting phase [40].

$$\psi = 2\int_0^{\pi} h(\phi)\cos(\phi)d\phi \tag{2.1}$$

$$\left\langle d(t)^2 \right\rangle = 2n\mu\left[t - P(1 - e^{-t/P})\right] \tag{2.2}$$

$$\mu = S^2 P / n \tag{2.3}$$

$$P = <\tau> /(1-\psi) \tag{2.4}$$

Using the r3 criteria and a $\phi_{cut} = 45°$, the total number of mode Is and mode IIs, the mean directional-mode time and re-orientation-mode time was determined for each cell in a given cell type. The results of the bimodal analysis of cell path data obtained using an experimental time-step of 0.5 minutes and 40x magnification are shown in Table 2.1. The various parameters such as the mean directional-mode time, re-orientation-mode

time, mean speed and persistence index, were calculated. The parameters obtained for the control pBabe, pre-malignant neuN and invasive neuT cells are listed together.

This analysis was repeated by extracting data with $\Delta t_{exp} = 2.5$ minute from the 0.5 minute data. The number of data trajectories available with the 2.5 minute data extracted from the 0.5 minute data would be five times more but the number of frames (data points) in each trajectory would reduce by 5 times. For instance, for the tracking time of 2 hours, the 0.5 minute data with 15 data trajectories from 15 cells and 240 frames each would convert to 2.5 minute data with 75 data trajectories from 15 cells and 48 frames each. Similarly, 1 minute Δt_{exp} data can be extracted from 0.5 minute data by considering every other data point. The various parameters obtained from 2.5 minute data analysis are listed in Table 2.1. Figure 2.8 shows an example cell trajectory of the same data with different Δt_{exp} such as 0.5, 1 and 2.5 minute.

The effect of the resolution at which the images of migrating cells are recorded was studied by comparing data at two different magnifications, namely, 40x (1 pixel≡0.163 μm) and 10x (1 pixel≡0.647 μm) where 10x data was extracted from the acquired 40x data. The ϕ distribution, turn angle distribution, directional-mode time and re-orientation-mode time distributions for pBabe cell type determined at different resolutions or pixel sizes and at a constant $\Delta t_{exp} = 0.5$ minute are shown in Figs. 2.9 a, b, c and d. The same effect at a $\Delta t_{exp} = 2.5$ minute is illustrated in Figs 2.9 e, f, g and h. The influence of pixel size on various parameters obtained from 'bimodal analysis' was studied by comparing the results from data analysis at different magnifications (Table 2.1). The statistical significance of such comparisons for the different cell types is shown in Table 2.2.

The influence of sampling interval of data collection on the distributions keeping the pixel size constant is studied in Fig. 2.10. The parameters calculated at different $\Delta t_{\exp}$ but same pixel sizes are compared (Table 2.1). The results obtained from 0.5 minute data are compared with that of 2.5 minute data at constant magnification of 40x for statistical significance (Table 2.2). This comparison becomes especially important when extracting short time dynamics such as directional-mode time and re-orientation-mode time dynamics. One can realize that the sampling interval of data collection should be small enough (at least smaller than the mean time for the directional and the less persistent modes) to capture the bimodal framework of the mammalian cells.

2.5 Discussion

2.5.1 Empirical factors for 'bimodal' analysis

The two empirical factors in the bimodal analysis are the criterion (example r3, r2, r1 as described in methods section) and the cut-off value of ϕ used (ϕ_{cut}) to locate the two alternating modes in the cell path. The values of these two empirical factors (criterion and cut-off) need to be chosen by visualizing several trajectories of the cells under consideration. One can realize that a less stringent criterion defining a directional-mode such as the r1 criterion (Fig. 2.11) compared to a more stringent r3 criterion would decrease the observed mean directional-mode time. The less-stringent r1 criterion (directional-mode characterized by only one frame) reduces the duration of the re-orientation-mode and picks up more directional and re-orientation modes. The mean directional-mode time and re-orientation-mode times are reduced with r1 criterion. The same is found experimentally: for example for neuT cells with r1 criterion, the

directional-mode time is 2.42±0.63 minutes and re-orientation-mode time is 1.86±0.50 minutes, compared with 3.5±0.7 and 4.3±1.2 minutes respectively using the r3 criterion.

The $\phi_{cut} = 45°$, was chosen empirically as a cut-off value that best succeeded in flagging the re-orientation phase on the nucleus track of the cells. The bright-field images of cells that we collected are likely to be insufficient to relate the cut-off value to any molecular mechanism. However, it could be speculated that this cut-off may relate to actin-myosin pathway. This cut-off might represent a turn made by the cell due to pronounced actin activity in a specific direction in the leading lamellipodium. A value less than this cut-off may pick up fluctuations in the cell path arising from more minor cytoskeletal re-arrangements, such as smaller lamellopodia. The r3 criterion used here to locate the beginning and end of a re-orientation phase is similar to the one used to flag the bacterial tumbles [29]. The data acquisition conditions used to determine the cut-off, $\phi_{cut} = 45°$, was most frequent sampling (0.5 minutes) and spatial resolution of 40x. We have tested the applicability of the criteria established to locate bacterial runs and tumbles to the mammalian cells. We find that the same framework works for mammalian cells provided that the cells are tracked frequently using a small sampling interval (0.5 minute). The application of this criterion to a different temporal resolution (say, 10 minute) might still identify the cellular turns recorded at this large sampling interval, but details of cellular turns during the 10 minutes will be lost.

2.5.2 Influence of pixel size

a) **Distributions:**

The net observed position of a cell (by manually tracking the nucleus of a cell) as it moves, is affected by the pixel information available. When a cell moves from one position to another in time, it moves from one grid point to another in a 2-dimensional space formed by several small square grids. The length of the square grid depends on the pixel size calibration of the image. Under these circumstances, the value of direction change would be biased at certain angles (0, 45, -45, 90, -90, 180, -180, 135) because of division of space into square grids of the length of 1 pixel. This would be applicable under the circumstance that the cell moves by 1 pixel in each frame. This limitation of available pixel size leads to the increased probability of certain angles in the ϕ distribution. We call this as the 'pixelation effect' that leads to spikes at certain positions. It was seen that, collecting the data at higher resolution (lower pixel size in μm) could minimize this effect and relatively smoothen the ϕ distribution (Figs. 2.9a and e). The pixelation effect is more pronounced at $\Delta t_{\exp} = 0.5$ minute as the cell moves by 1 pixel unlike at $\Delta t_{\exp} = 2.5$ minutes.

A comparison of directional and re-orientation time distributions obtained from data at different resolutions at a given $\Delta t_{\exp}$, such as 0.5 minute or 2.5 minutes revealed that there was negligible influence of resolution (Figs. 2.9c, d, g and h). The distributions obtained from extracted 10x data have similar trend as the 40x distributions. The turn angle distribution from 40x is expected to have more pixel information compared to 10x because of pixelation effect in the ϕ distribution at lower resolution. Hence, the spatial resolution has a subtle influence on the turn angle distribution obtained (Figs 2.9b and f).

b) **Parameters:**

There was no statistically significant effect of pixel size on mean directional time and re-orientation times for all cell types (Table 2.2, $p>0.05$). The mean speed for all the cell types was found to be similar at both resolutions. The p-values from Kolmogorov-Smirnov test for comparison of mean speed at different resolutions were < 0.001 (significant) for all cell types even though the mean values are very similar. So, we ran Mann-Whitney test to confirm this and compared speed at different resolutions which gave p-values > 0.05 (not significant). Overall, there was negligible impact of resolution on the various parameters and distributions obtained.

2.5.3 *Influence of sampling interval,* $\Delta t_{\exp}$

a) Distributions:

The turn angle distribution obtained with 0.5 minute data appears less noisy and more spread out compared with the distribution from 2.5 minute data (Fig. 2.10a). This can be explained because of more directional modes being located on a given cell trajectory with sampling time interval of 0.5 minute compared with a cell trajectory with 2.5 minute sampling time interval. For instance, the average number of directional modes in a 0.5 minute data path is 10 compared to 3 in a 2.5 minute data. Thus, the availability of more data points to average over in the case of turn angle distribution from 0.5 minute data. The same logic holds true for the directional time and re-orientation time distributions (Figs 2.10b and c). Using the more frequently sampled data (0.5 minute), the detailed cellular turns at this smaller time scale can be detected whereas they would not be with sparsely sampled 2.5 minute data. Because more turns are flagged, this results in smaller mean directional-mode and re-orientation-mode times with a 0.5 minute sampling

interval. This shows the impact of using smaller sampling interval while collecting migration data for applying bimodal analysis.

b) Parameters:

The influence of sampling interval $\Delta t_{\exp}$ used for the data collection on cell parameters such as mean speed has been previously investigated [61]. The net displacement of a cell over a time interval, t, would be larger if the sampling time interval at which the cell position is recorded during the course of experiment becomes smaller. The mean speed variation with $\Delta t_{\exp}$ for pBabe cells is illustrated in Fig. 2.12. The squared difference in the measured speed at 0.5 minute sampling interval and speed at any higher sampling interval ($\Delta t_{\exp}$>0.5 minute) reduces as $\Delta t_{\exp}$ approaches 0.5 minutes. The measured speed would increase as the sampling time interval is decreased. This experimental observation was confirmed using simulations (Fig. 2.13).

The squared difference in the speed at $\Delta t_{sampling} = 0.5$ minute sampling interval and speed at any higher sampling interval ($\Delta t_{sampling} > 0.5$ minute) reduces as $\Delta t_{sampling}$ approaches 0.5 minutes. The measured speed is found to increase as the sampling time interval is decreased. A simple random walk simulation illustrates this observation. We performed a simulation with time step Δt_{sim}= 0.5 minute. The lattice spacing is $\ell = 0.5\mu$m, and in the random walk we move one lattice spacing per step, so the actual speed is $v_{actual} = \ell / \Delta t_{sim} = 0.5\mu m / 0.5$minute, or $v_{actual} = 1$ μm/minute. We know from the theory of random walks that the displacement of the random walker after n steps will be $r = A(n\Delta t_{sim})^{\alpha}\ell$, where at short enough times $\alpha = 1$ (corresponding to ballistic motion) and at long times $\alpha = 0.5$ (corresponding to diffusive motion) and A is a pre-factor to

match the units, which at long time is simply related to the diffusion coefficient. Let the measurement interval is $\Delta t_{sample} = m\Delta t_{sim}$. For example, a sampling time of 2.5 minutes corresponds to $m = 5$. We expect that the measured speed will be:

$$v_m^{measured} = \frac{r_m}{t_{sample}} = \frac{A(m\Delta t_{sim})^{\alpha}\ell}{m\Delta t_{sim}} = Am^{\alpha-1}(\Delta t_{sim})^{\alpha}\frac{\ell}{\Delta t_{sim}} = Am^{\alpha-1}(\Delta t_{sim})^{\alpha}v_{actual} \qquad (2.5)$$

If $m = 1$, we can assume we are in the ballistic regime, so equation 2.5 gives $v_1^{measured} = v_{actual}$. And, indeed, we see from Fig. 2.13 that the sampled speed is in fact the actual speed. However, for $m > 1$ (which in the experiment corresponds to sampling times greater than 0.5 minute, such as 2.5, 5 and 15 minutes), equation (2.5) predicts that the sampled speed will be less than the actual speed. In fact, the curve in Fig. 2.13 has the same characteristics as the experimental curve (Fig. 2.12). Thus we see from Fig. 2.13 that although the sampled speed does not appear to asymptote to a value at short sampling times, in fact it is becoming the exact result. This gives us some confidence that our measured speed at the 0.5 minute interval is a reasonable estimate of actual cell speed.

For the bimodal analysis of the cell trajectory data, the rate at which the data was collected can play a very critical role. This is evident from the comparisons of mean directional-mode times calculated from 0.5 and 2.5 minute data (Table 2.1). One can see that by using the same empirical factors for locating both mode I and mode II, the mean directional-mode time for pBabe cells was found to be ~3 minutes (using 0.5 minute data) and ~18 minutes (using 2.5 minute data) at 40x. Frequently sampled data can capture the re-orientations made by a mammalian cell on a smaller time scale, which may not involve locomotion of a cell body length. This information might be lost with

sparsely sampled data. We speculate that the description obtained from smaller sampling interval could be useful in getting some insight in the cytoskeletal re-arrangement arising due to more pronounced actin machinery in a specific direction. We find a statistically significant effect of sampling interval used on the values of directional-mode time, re-orientation-mode time and cell speed obtained ($p<<0.05$). Thus, we find that the impact of sampling time interval is more significant compared to the resolution (Table 2.2).

The single cell dynamics extracted here for the random migration of these epithelial cells will form the basis of performing cellular level simulations of these cells. The accuracy of the bimodal analysis technique can be assessed by identifying the re-orientation phase from a known artificially created cell trajectory using cellular dynamics simulation ([35], Chapter III) based on the bimodal model and parameters extracted from bimodal analysis (Fig. 2.14). The cellular dynamics simulation scheme used here has the same basic algorithm that was used to simulate bacterial migration [35], modified to have a bimodal motion with experimentally determined turn angle, directional-mode and re-orientation-mode distributions. We can see that all the turns (known independently from simulation) in the artificial trajectory are picked up by the r3 analysis technique.

A greater insight into the migration of cancer cells both in the absence and presence of attractant gradients will clarify the sensing mechanism (to be discussed in Chapter VI) and the effect on turn angle distributions of these eukaryotic cells, and provide the basis for incorporating individual eukaryotic cell motion into cell-based models for tissue, such as the Anderson model for tumor growth [62].

2.5.4 Random motility coefficient, persistence and invasiveness

Figure 2.15 shows the experimental mean squared displacement of the three cell types versus time on a log-log scale. We can see that the displacement lies between the slope 2 (the 'ballistic regime') and slope 1 (the 'diffusive regime'). This indicates that the two-hour experimental tracking time is not long enough for the cell motion to enter the diffusive regime, so that the random motility coefficient cannot be estimated for the relatively slow-moving MCF-10A cells and warrants the tracking of these cells for several hours to days in not so conducive conditions for cells. This problem can be circumvented by performing 'cellular-dynamics' simulations long enough to reach the diffusive regime, and will be discussed in details in Chapter III.

We have estimated the value of persistence indices for the various MCF-10A cell types using equation (2.1) just for the sake of getting some insight of the effect of increasing level of Her-2 expression that is, increasing invasiveness. We find that our highest resolution data (smallest sampling interval and highest spatial resolution) show an increasing persistence with increasing level of Her-2 expression from pBabe, neuN and neuT cells. This is consistent with the hallmark of cell migration in invasive tumors [63] and in cells with over expressed levels of Her-2 receptor which showed higher directional persistence in wound closure kind of assay [47].

2.6 Conclusions

The bimodal analysis of mammalian cell migration paths reveals that cellular re-orientation modes could last longer than directional modes. The scenario in bacterial migration is different where the tumbles are almost instantaneous. It is also clear that the sampling interval $\Delta t_{\exp}$ of observation during time-lapse microscopy should be chosen to

be small enough (< 1 minute for the cell/substrate combination studied here) to capture the directional and re-orientation framework in a mammalian cell migration path using bimodal analysis. Note, however, that some properties (such as the random motility coefficient) do not depend on the sampling frequency while others, such as the cell speed and turn angle distribution, are impacted by the sampling time interval of observation.

This bimodal cell migration scheme can be incorporated into the existing tumor models of cancer invasion to develop more realistic mathematical models of tumor that can help in accurate prognosis and treatment of cancer[22, 62, 64]. However, the important conclusion from this work is that the often-used random motility expressions for mammalian cell motion (based on assuming diffusive motion) are invalid over the time steps (order of few minutes[22]) typically used in modeling mammalian cell motility. The bimodal model correctly takes into account the time spent and the motion involved between directional runs, and so will lead to more appropriate quantification of the random motility of the cells, more accurately relating single-cell motion to macroscopic, population-level properties. Thus, it provides the basis for improved simulations of single-cell motion required in cell-based models of cancer growth.

Table 2.1: Parameters obtained from bimodal analysis of pBabe, neuN and neuT cell migration tracks at different Δt_{exp} and resolution for tracking time of 2 hours.

	Time interval[1]	$\Delta t_{exp} = 0.5$			$\Delta t_{exp} = 2.5$		
	Cell type	pBabe	neuN	neuT	pBabe	neuN	neuT
	No. of cells	15	15	12	15	15	12
	No. of trajectories	15	15	12	75	75	60
40x	Mean speed[2]	1.05±0.28	1.09±0.38	1.20±0.43	0.81±0.22	0.79±0.24	0.94±0.35
	Mean directional-mode time[1]	3.1±0.8	3.7±1.3	3.5±0.7	18.4±12.9	16.9±10.2	14.2±5.6
	Mean re-orientation-mode time[1]	4.5±1.0	5.0±2.2	4.3±1.2	20.6±13.8	20.3±13.9	18.0±13.2
	Persistence index, ψ	0.38	0.39	0.49	0.42	0.64	0.25
10x[3]	Mean speed[2]	1.05±0.28	1.09±0.39	1.21±0.43	0.8±0.22	0.78±0.23	0.93±0.35
	Mean directional-mode time[1]	3±0.4	3.29±1.08	3.84±1.13	18.5±12.3	13.7±6.8	13.9±7.4
	Mean re-orientation-mode time[1]	5.7±1.4	6.4±2.0	5.72±1.58	19.9±12.9	24.9±19.1	20.1±14.2
	Persistence index, ψ	0.28	0.34	0.29	0.37	0.59	0.29

[1] minute
[2] μm /minute
[3] Extracted 10x from 40x

Table 2.2: Statistical significance for effect of pixel size and sampling interval, Δt_{exp} on various parameters using Kolmogorov-Smirnov nonparametric test. A p-value <0.05 indicates significant difference.

Condition	Parameter	p-values (n1[3],n2[4])		
		pBabe	neuN	neuT
Constant Δt_{exp} (2.5 minute), compare 40x and extracted 10x	Mean directional-mode time[1]	0.943 (102,106)	0.548 (68,78)	0.990 (108,106)
	Mean re-orientation-mode time[1]	1 (102,106)	0.741(68,78)	0.989 (108,106)
	Mean speed[2]	< 0.001 (3525,3525)	<0.001(3525,3525)	< 0.001 (2820,2820)
Constant pixel (40x), compare 0.5 and 2.5 minute, Δt_{exp}	Mean directional-mode time[1]	< 0.001 (214,102)	< 0.001 (187,68)	< 0.001 (169,108)
	Mean re-orientation-mode time[1]	< 0.001 (214,102)	< 0.001 (187,68)	< 0.001 (169,108)
	Mean speed[2]	< 0.001 (3585,3585)	< 0.001 (3585,3585)	< 0.001 (2868,2868)

[1] minute
[2] μm /minute
[3] sample size at 40x (constant Δt_{exp}) or sample size at 0.5 minute (constant pixel)
[4] sample size at extracted 10x (constant Δt_{exp}) or sample size at 2.5 minutes (constant pixel)

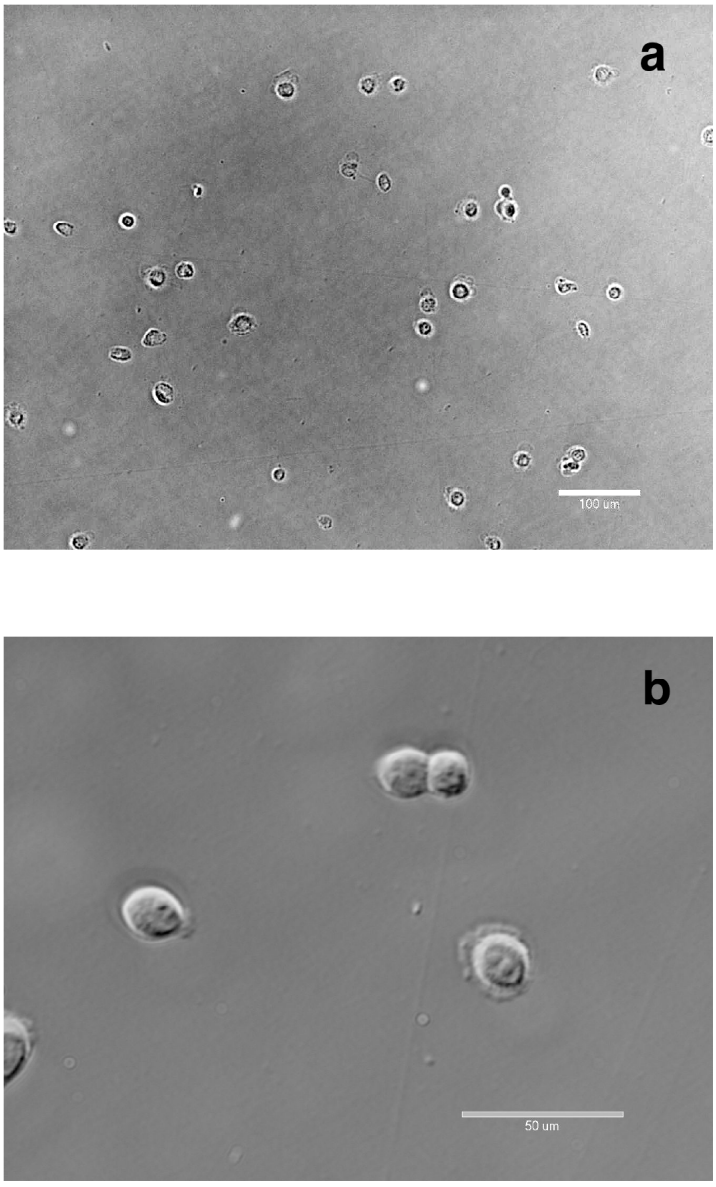

Figure 2.1: MCF-10A-neuT cells a) 10x resolution (1pixel≡0.647μm) and b) 40x resolution (1 pixel≡0.163μm).

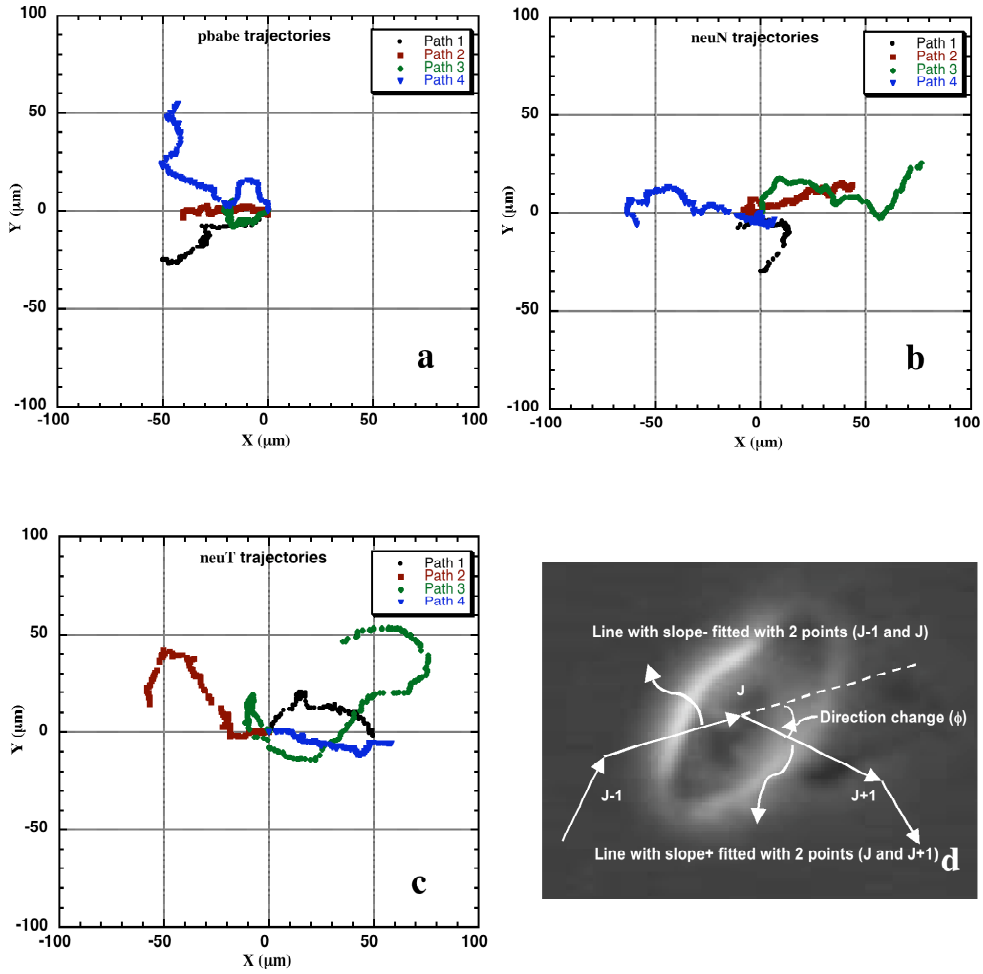

Figure 2.2: Example cell paths of MCF-10A-pBabe (a), neuN (b) and neuT (c) cells used for bimodal analysis re-plotted as wind rose plots. The data was collected with 40x magnification every 0.5 minutes. d) The direction change (ϕ) calculated at each frame in a cell path. The direction was determined by fitting slope using two-point linear regression.

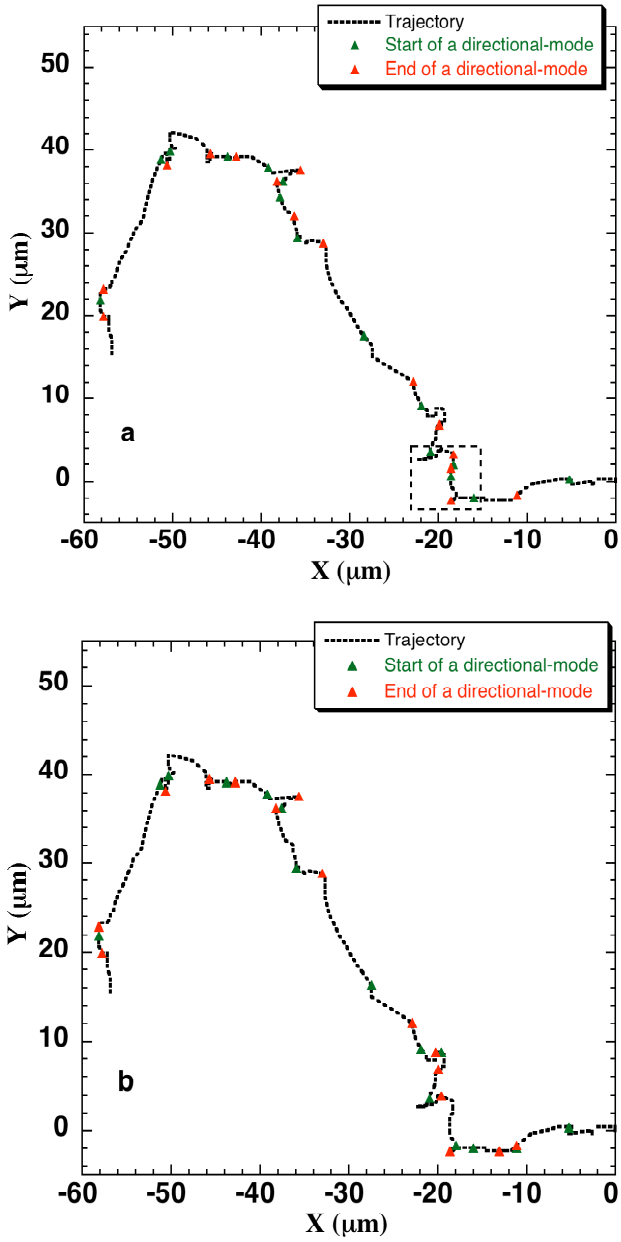

Figure 2.3: The directional-mode (mode I) and re-orientation-mode (mode II) located in a neuT cell trajectory using a) $\phi_{cut} = 35°$, b) $\phi_{cut} = 45°$. The 'r3 criteria' was used for locating the directional-modes in each case.

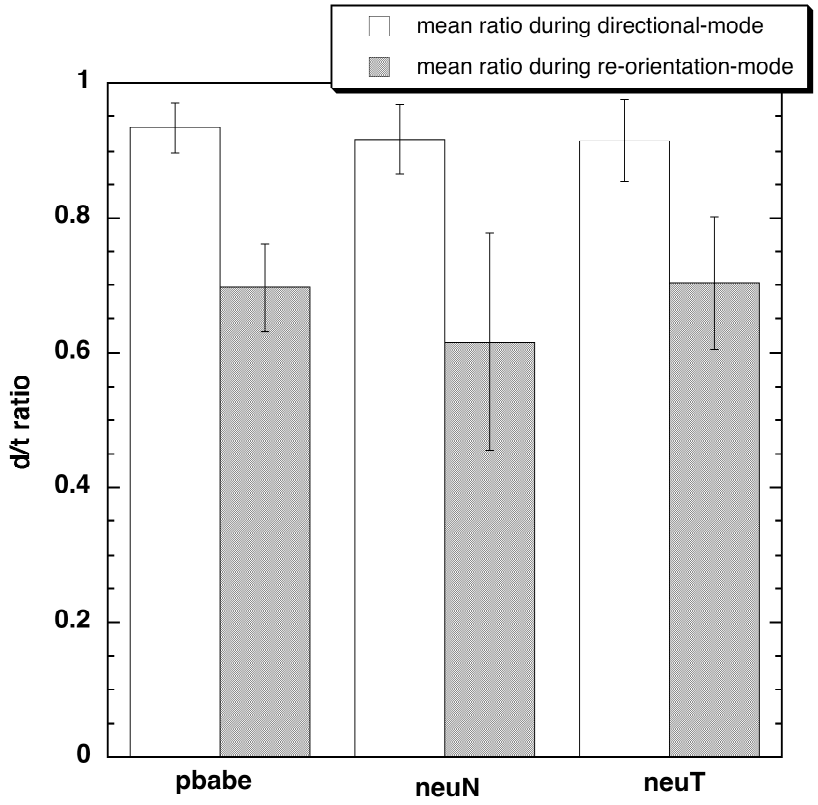

Figure 2.4: The mean d/t ratios for the cells located during the two phases indicating the presence of the mode I and mode II phases in a cell path (pBabe ($p < 0.001$, $n=214$), neuN ($p<0.001$, $n=187$) and neuT ($p<0.001$, $n=169$) using Kolmogorov-Smirnov nonparametric test).

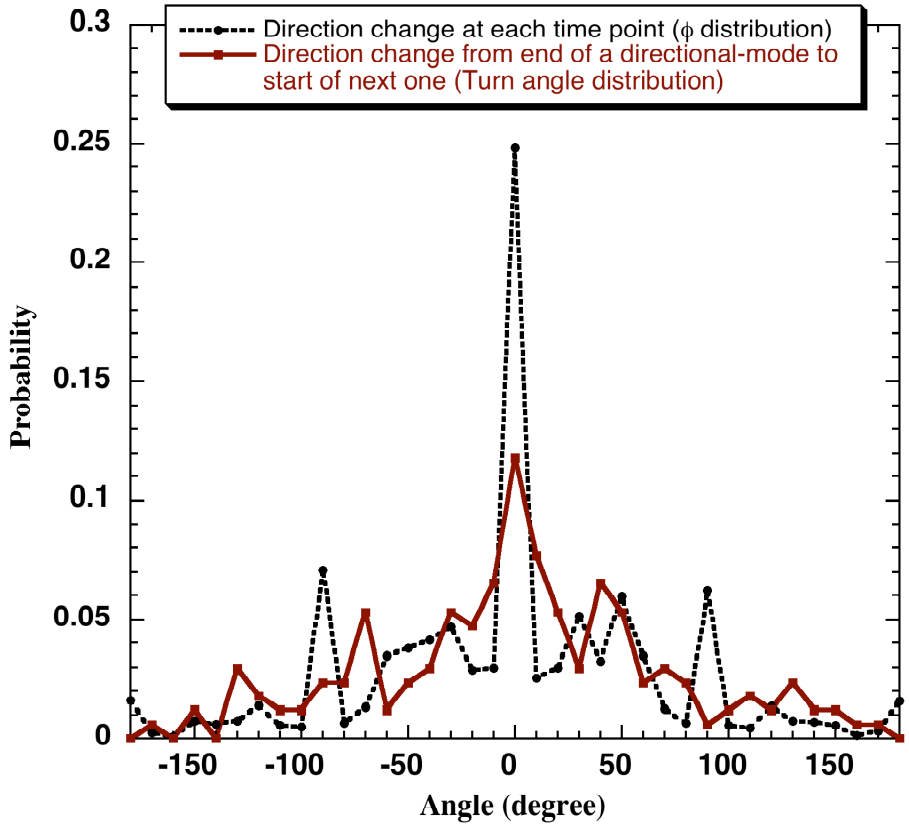

Figure 2.5: The discrete probability distribution of direction changes at each time step (distribution of ϕ values) and direction changes from end of one directional phase to the start of another (turn angle distribution) obtained using a bin size of 10 degrees for neuT cells tracked using $\Delta t_{exp} = 0.5$ minutes and 40x magnification for 2 hours.

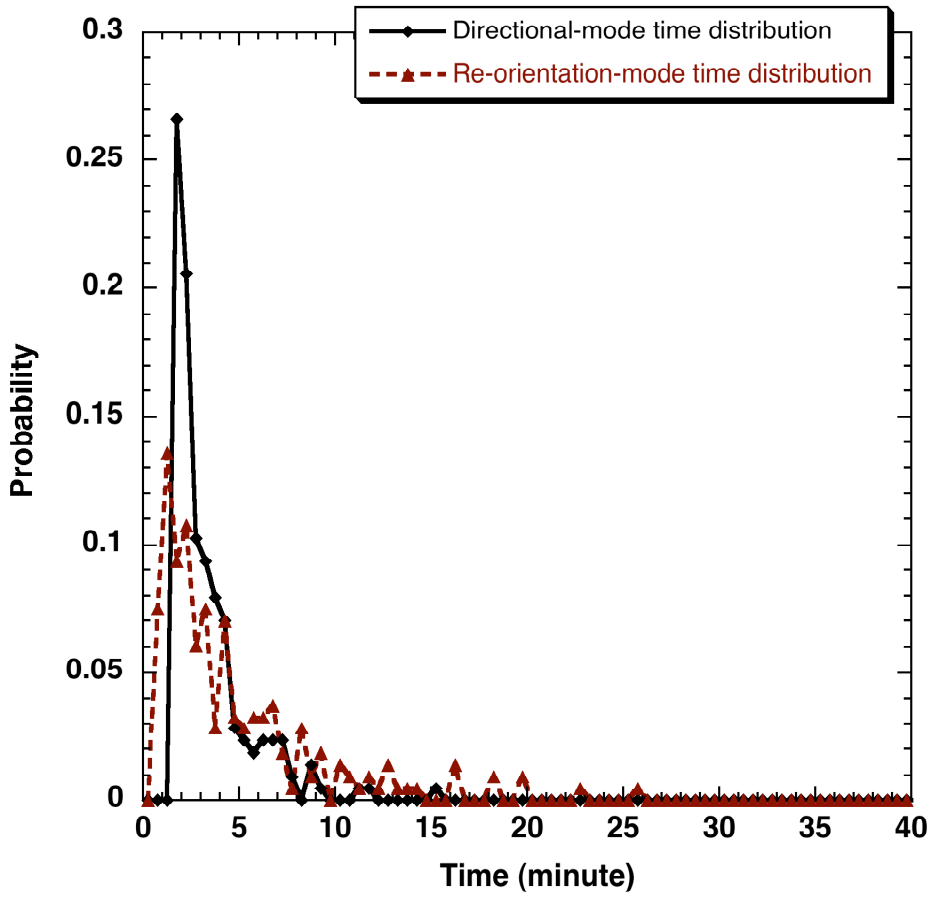

Figure 2.6: The discrete probability distributions of directional-mode times and re-orientation-mode times obtained using a bin size of 0.5 minutes for pBabe cells tracked using $\Delta t_{\exp} = 0.5$ minutes and 40x magnification for 2 hours.

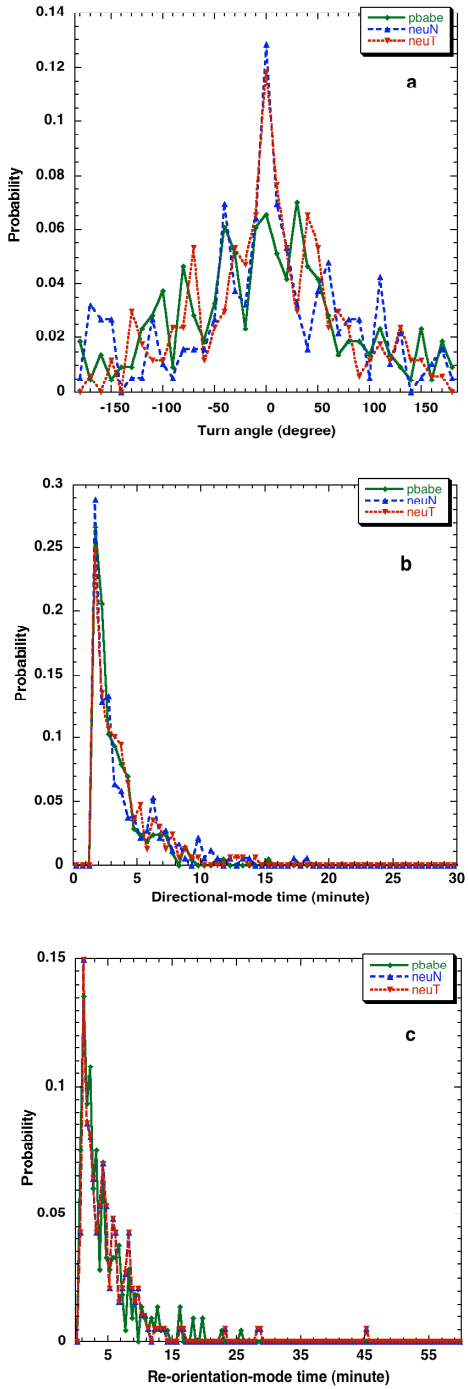

Figure 2.7: The discrete a) turn angle probability distributions for pBabe, neuN and neuT cells obtained using a bin size of 10 degrees for cells b) directional-mode time probability distributions of pBabe, neuN and neuT cells using bin size of 0.5 minute and c) re-orientation-mode time probability distributions of pBabe, neuN and neuT cells using bin size of 0.5 minute tracked using $\Delta t_{\exp} = 0.5$ minutes and 40x magnification for 2 hours.

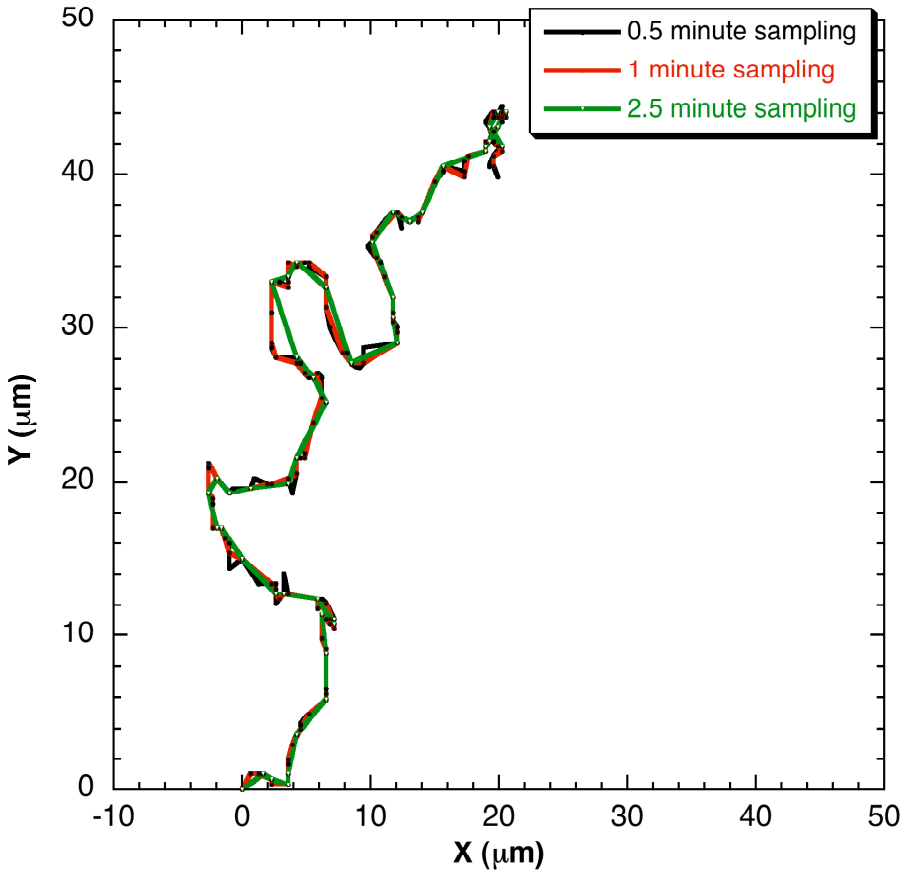

Figure 2.8: An example cell trajectory if the data were collected at 0.5, 1 and 2.5 minute of $\Delta t_{\exp}$.

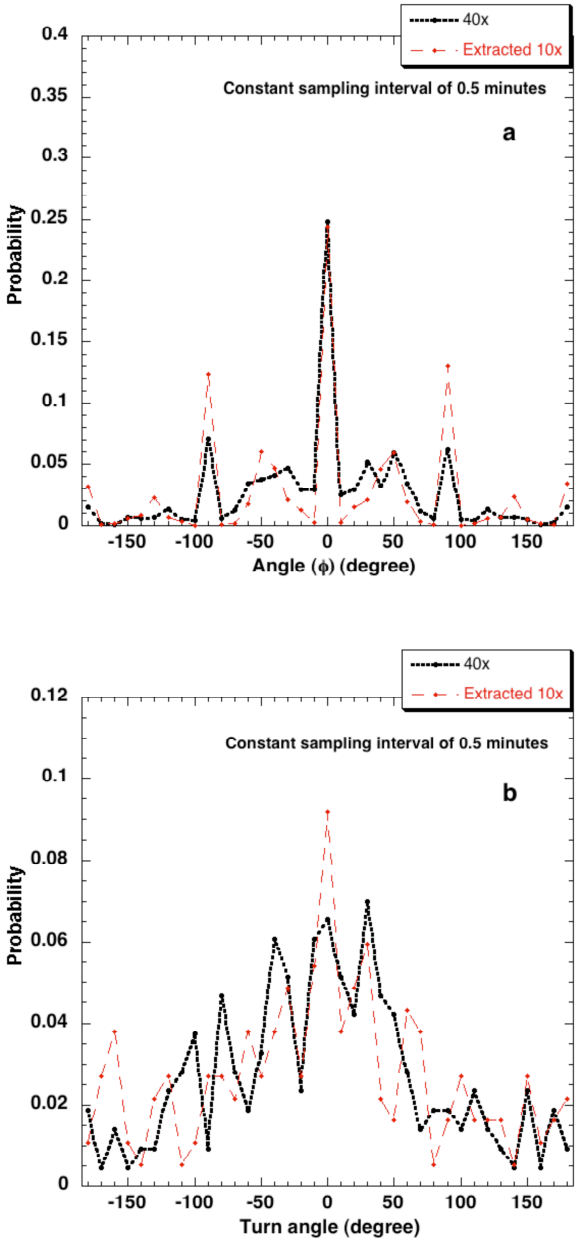

Figure 2.9 (a, b): Effect of pixel size at Δt_{exp} = 0.5 minutes on a) ϕ distribution, b) turn angle distribution.

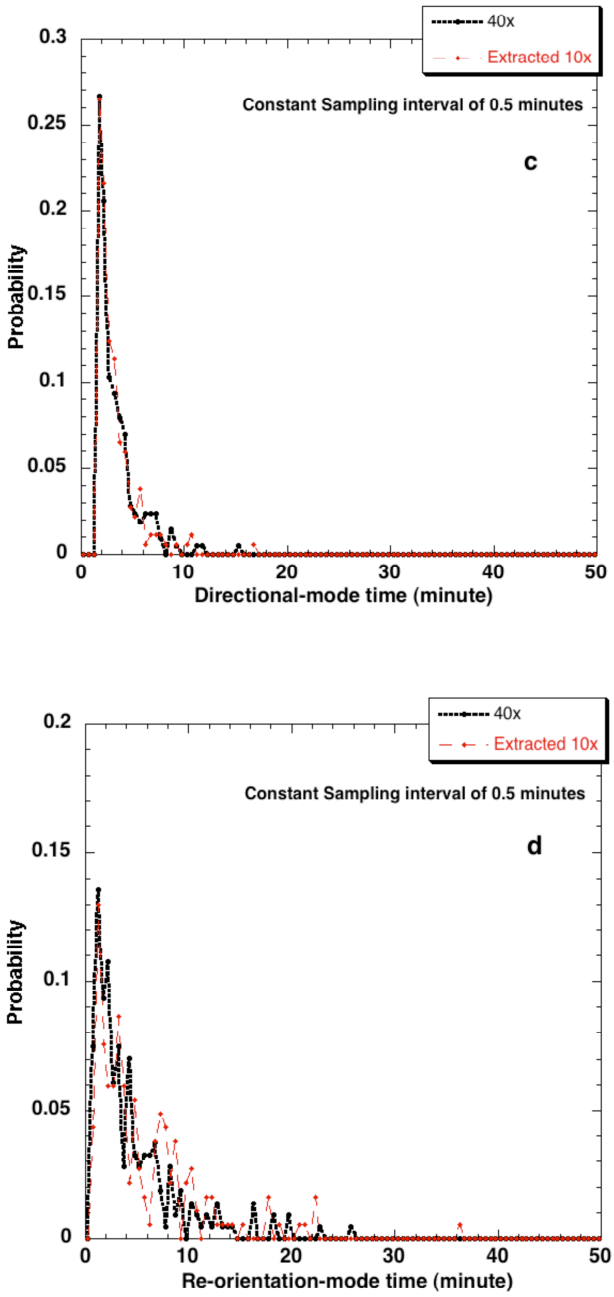

Figure 2.9 (c, d): Effect of pixel size at Δt_{exp} = 0.5 minutes on c) directional-mode time distribution and d) re-orientation-mode time distribution.

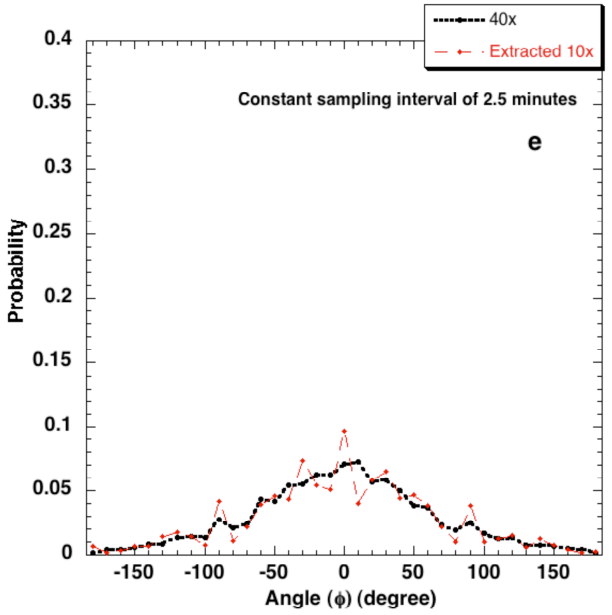

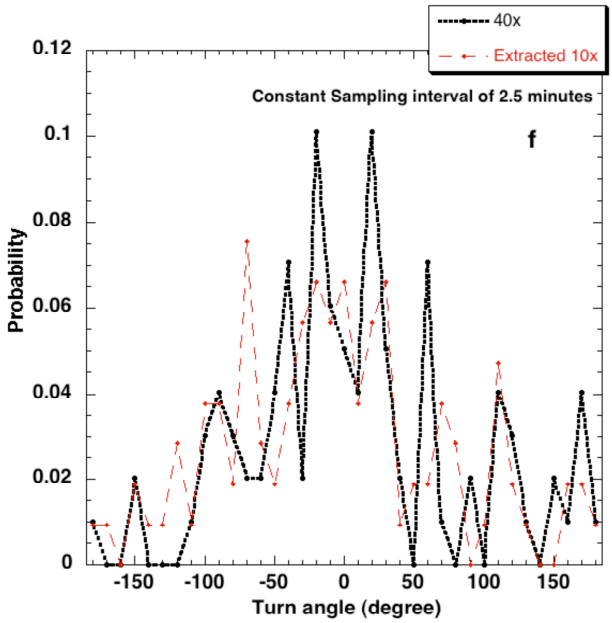

Figure 2.9 (e, f): Effect of pixel size at Δt_{exp} = 0.5 minutes on e) ϕ distribution, f) turn angle distribution.

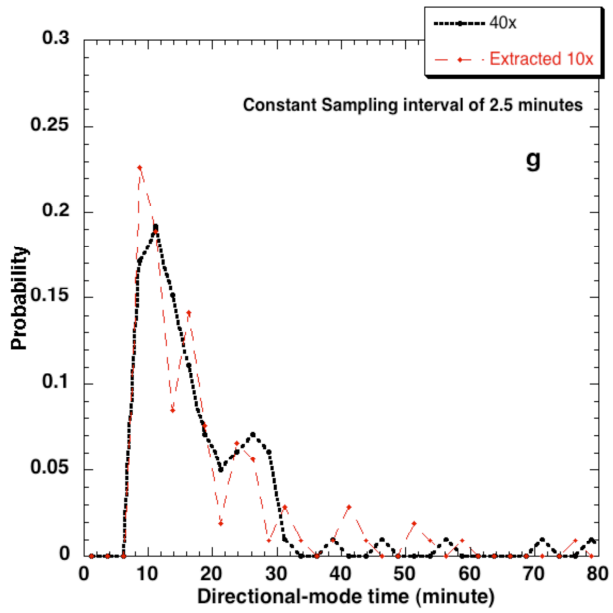

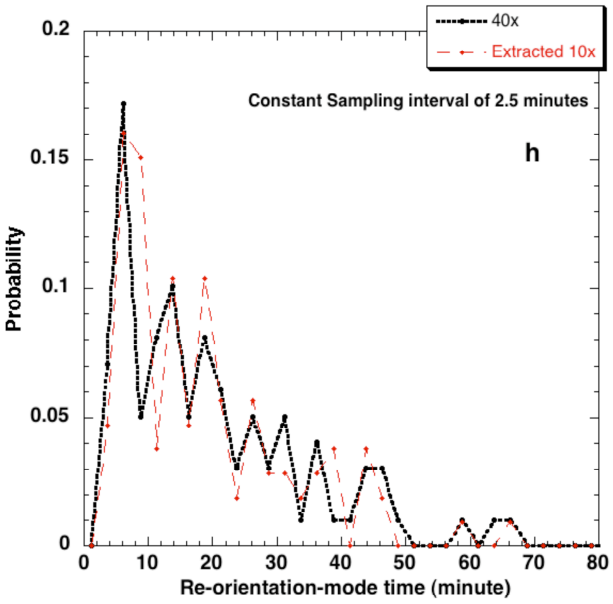

Figure 2.9 (g, h): Effect of pixel size at $\Delta t_{exp} = 0.5$ minutes on g) directional-mode time distribution and h) re-orientation-mode time distribution.

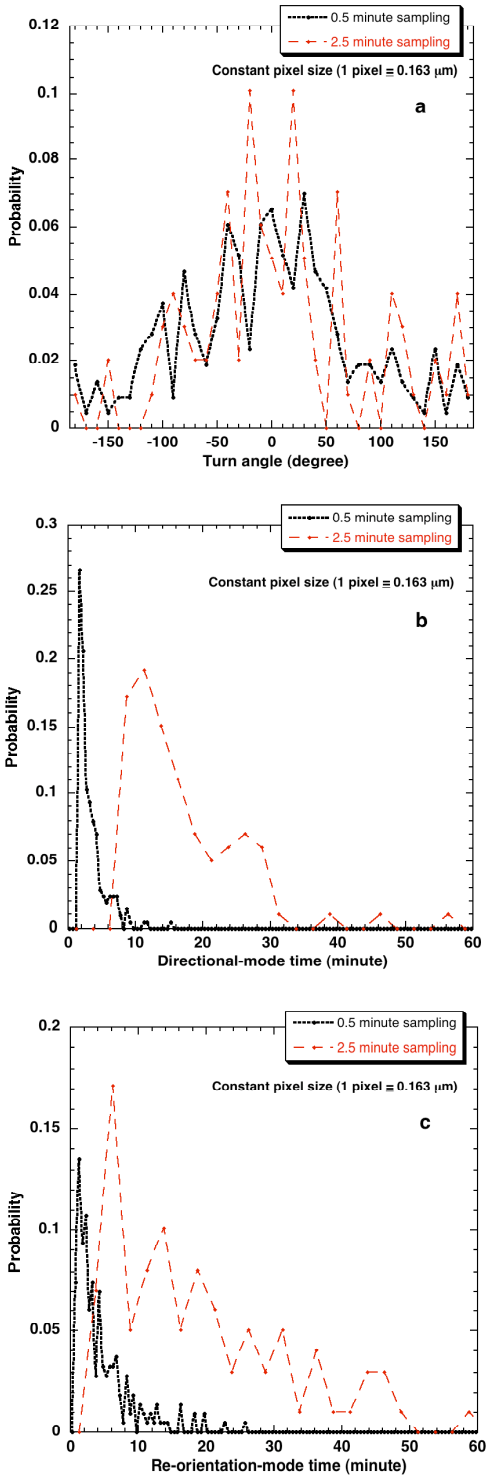

Figure 2.10: Effect of different Δt_{exp} on a) turn angle distribution b) directional-mode time distribution c) re-orientation-mode time distribution at 40x resolution.

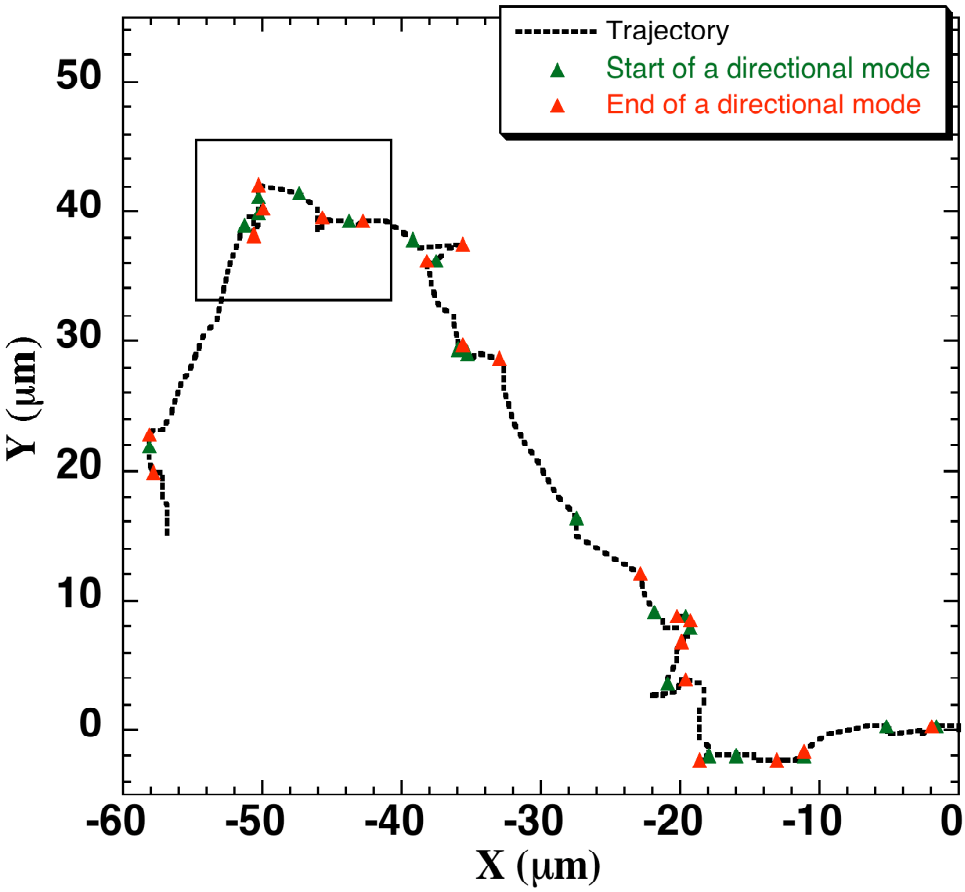

Figure 2.11: The directional-mode (mode I) and re-orientation-mode (mode II) located in a neuT cell trajectory using $\phi_{cut} = 45°$ and 'r1 criteria'. The change with respect to r3 criteria (Fig. 3b) has been highlighted in the square inset.

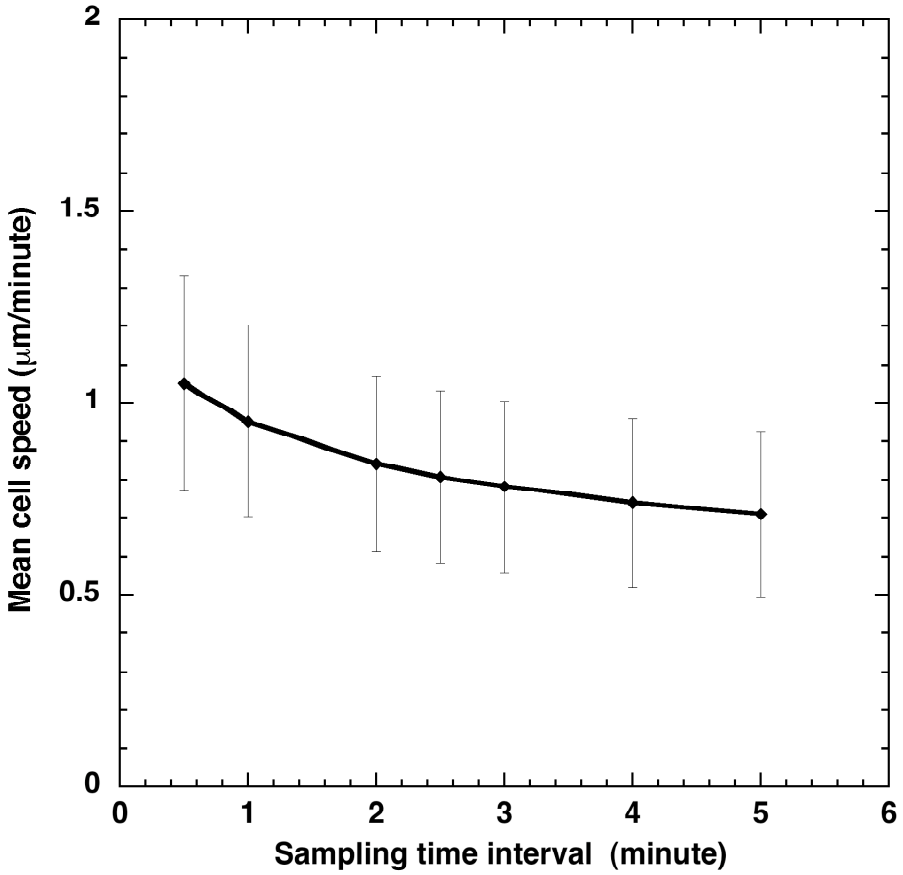

Figure 2.12: Influence of sampling time interval of observation on mean cell speed in pBabe cells.

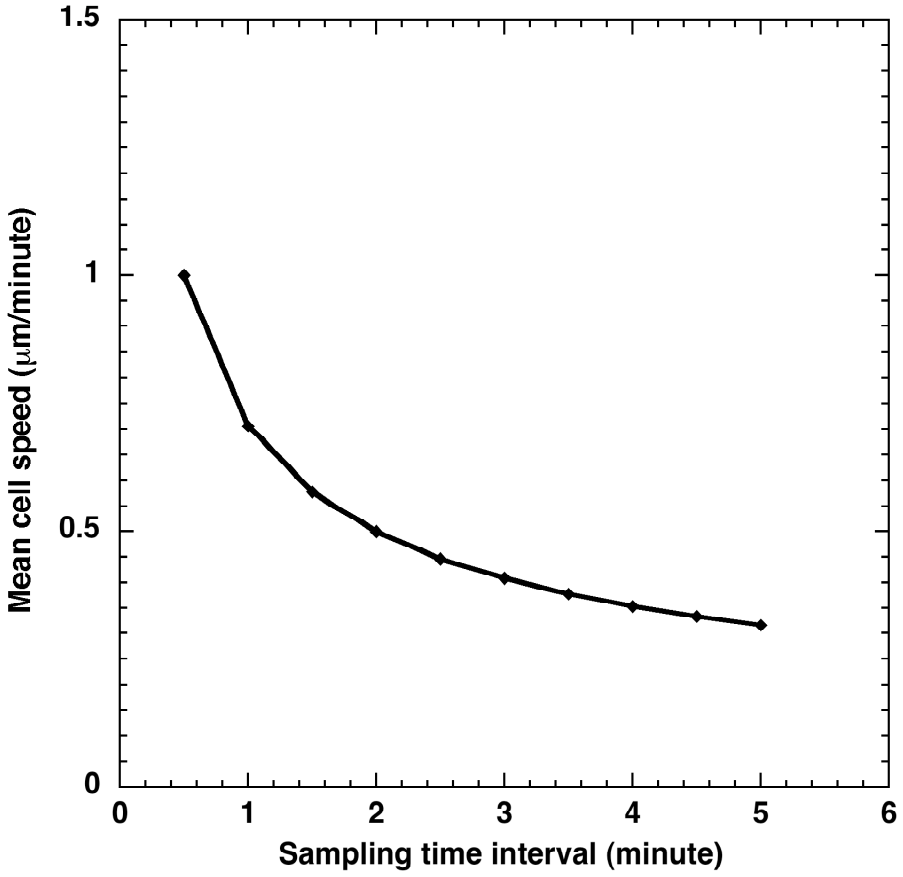

Figure 2.13: Mean speed versus time trend for a random walk simulation.

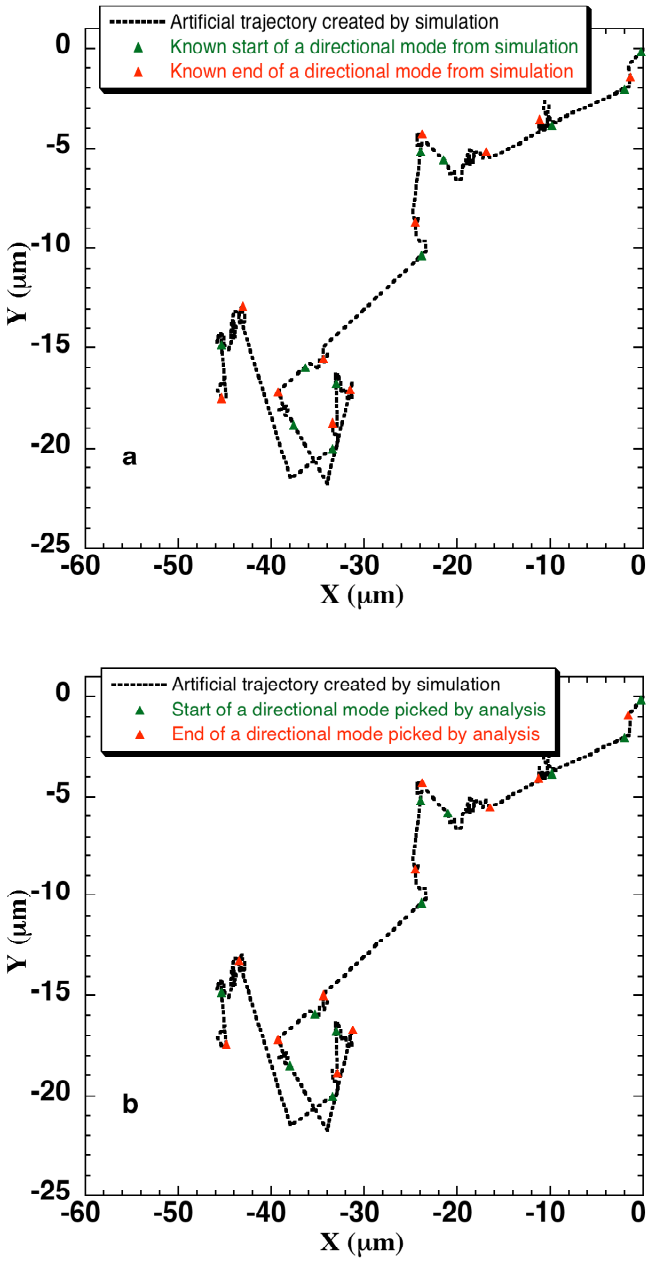

Figure 2.14: a) An artificial trajectory of a cell created using cellular dynamics simulation with the known directional and re-orientation modes indicated. b) Analyzed artificial trajectory with (r3 criterion and ϕ_{cut} = 45° cut-off) with the two modes indicated.

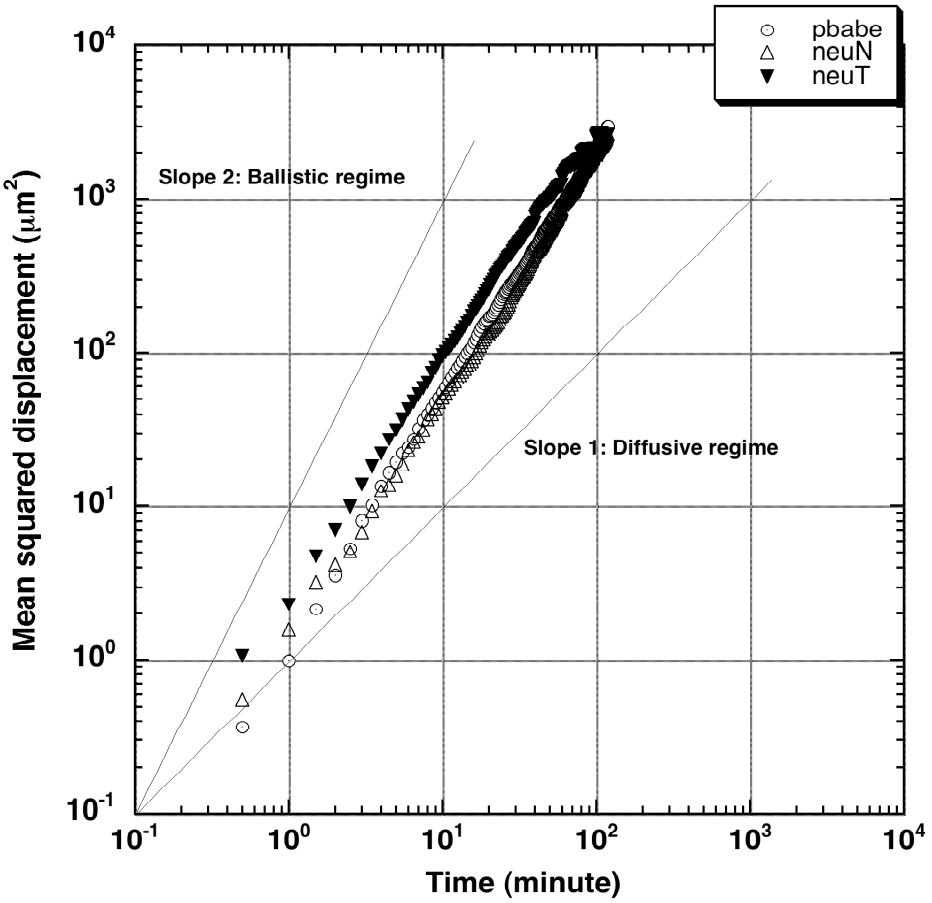

Figure 2.15: Experimental mean squared displacement versus time for the three cell types.

CHAPTER III

CELLULAR DYNAMICS SIMULATIONS OF MCF-10A CELL RANDOM MIGRATION

3.1 Abstract

We have implemented the cellular dynamics simulation methodology [35] (originally developed for bacterial migration) to describe the random migration of MCF-10A pBabe, neuN and neuT cells (expressing different versions of the pro-migratory tyrosine kinase receptor Her2/Neu). This simulation technique enables prediction of random motility coefficient of a given cell type by simulating large number of cells for a relatively long time using known single-cell dynamics. The experimental parameters extracted for each cell type, by the application of *bimodal analysis* technique developed by us, were used to perform these simulations. The bimodal framework inspired from the bacterial run-tumble scheme segregates mammalian cell tracks into alternating directional and re-orientation modes. The mean squared displacement of these epithelial cells reaches the diffusive regime after approximately 2 hours according to simulations. We find from simulations that the Her-2 transformed neuT cells have higher random motility coefficient compared to the control pBabe.

3.2 Background

Studying cell migration is a challenging problem that warrants a synergistic feedback between experimental and modeling approaches. We know that cells from all domains

such as prokaryotic bacteria to eukaryotic mammalian cells exhibit migration, for survival (moving towards a food source or migrating away from unfavorable scenarios) [65] to performing normal physiological functions (such as embryogenesis, tissue repair) respectively. Understanding how cells behave on an individual level is an essential element in predicting their population-level behavior. For example, the transport properties from the individual cellular level have been correlated to those at the population level [19, 21, 66] for both random and biased cell migration of bacteria and leukocytes.

The single cell level studies are typically done at lower densities of cells and may not necessarily encompass all the high-density features. Nonetheless, the knowledge of single cell level parameters can provide a good starting point to model and predict population level behavior. This information can be useful in quantifying the subtle differences in cell motility arising due to different genetic makeup such as predicting the phenotypic behavior due to an over-expressed gene via population level simulations.

Experimental single cell level dynamics have been successfully incorporated into a model for cell populations in the case of bacteria via cellular dynamics simulations [32, 35, 36]. Such an effort needs to be replicated for eukaryotic cells and is the premise of this work for the specific case of mammary epithelial cell random migration. We extracted the single cell level parameters of MCF-10A, human mammary epithelial cells, expressing different versions of pro-migratory tyrosine kinase receptor Her2/Neu using bimodal analysis [37]. We use the experimental parameters extracted from this analysis to perform cellular dynamics simulations of these epithelial cells.

3.2.1 Modeling cell migration

Computational model of any cellular process could range over a diverse spectrum from low-detail Bayesian networks (used to model interactions between different molecules in a given cellular pathway using conditional probabilities) to more-detailed differential equations incorporating different details at various levels [67]. Mathematical models of single-cell migration have been developed to represent either a macroscopic population level or microscopic individual level. Population models describe cell density via convective diffusion equations on a continuous level such as the Keller and Segel model [68] while the microscopic level models are based on individual cell dynamics on a discrete level and are described by stochastic equations of motion. There are also hybrid models where individual cells move on lattice while the extra-cellular matrix encompassing the cells is continuous [64]. The migration of individual mammalian cells has been often modeled using persistent random walk (PRW) model [41, 43, 45, 48-50]. However, a simple computational model for cell populations using experimental single cell dynamics needs to be described for mammalian cell migration.

3.2.2 Cellular dynamics simulations: Prior work-bacterial chemotaxis

The incorporation of single-cell dynamics into a model for cell populations has been successfully done in the past for bacteria [32, 35, 36]. Using the tumbling frequency and turn angle distributions from the 'run and tumble' analysis of the data collected from bacterial tracking experiments [29], as well as a quantitative relationship between chemoattractant concentration gradient and run-time extension, the 'cellular dynamics' simulation methodology [35, 36] was developed to predict the population level dynamics based on known individual bacterial information. Cellular dynamics was found to predict

cell motion through porous media [33, 69, 70]. In these simulations, a large number of bacteria are simulated based on known experimental single cell dynamics. To simulate bacterial motion within a porous media, the mathematical characterization of experimentally determined cell-surface dynamics [32] is also required. In order to extend this scheme to eukaryotic cells, similar parameters were extracted from the mammalian cell tracking data in our prior work [37].

The cellular dynamics simulation for bacteria starts with defining the initial position and direction for each bacterium. At each time step, it is determined if each bacterium tumbles or not. If it does tumble, its new direction of motion is chosen from the known turn angle distribution. If the bacterium does not tumble, it continues to move in the same direction. The new position of the bacterium is then determined based on its swimming speed, direction vector and the time step. This simulation scheme for bacteria is illustrated in the flowchart in Fig. 3.1 [35].

The simulation parameters required to do simulations of bacteria are: the turn probability which is related to the tumbling frequency of the bacteria and determines whether a bacteria tumbles or not at a given time step; the run-to-run turn angle distribution which gives the new direction of a run once the bacteria undergoes a tumble and finally, the mean speed of bacteria. These data were obtained using the 3-D tracking microscope developed by Berg [27, 29] and now in the Ford group at the University of Virginia [20, 32-34, 66, 70-74].

3.3 Model overview

3.3.1 Bimodal Analysis

Bimodal analysis (which segregates cell track into alternating directional and reorientation modes) is described in details in [37]. Briefly, the directional and reorientation modes were flagged by first computing instantaneous direction change (ϕ) at each frame (time point) and then applying a cut-off (ϕ_{cut}) to flag the modes. A cut-off value of $\phi_{cut} = 45°$ and 'r3 criterion' (ϕ value at three successive frames determines a directional mode) was used for all the data analysis. The turn angle, θ (the angle change between successive directional modes) was computed using multi-point linear regression of all the data points constituting a directional mode. The details of all the rules used to locate the modes can be found elsewhere [37] and were discussed in depth in the previous Chapter.

3.3.2 Mammalian cell migration scheme

The bimodal framework of cell motility of a mammalian cell involving the directional phase (mode I) and the re-orientation phase (mode II) is analogous to the run-tumble sequence exercised by a bacterium. Essentially, both the processes (bacterial and mammalian cell migration) are velocity-jump processes [40], the bacterial motility incorporating instantaneous tumbling while the mammalian cell migration can be defined as a process with a finite tumbling/re-orientation/relaxation time during which the cellular cytoskeleton is re-organized to polarize the actin-polymerization machinery in a new direction. Hence, the cellular dynamics methodology can be easily adapted to mammalian cell migration with minor modifications concerning the re-orientation time.

The modified simulation scheme proposed for mammalian cell migration is depicted in Fig. 3.2.

The simulation scheme for mammalian cells differs from the bacterial scheme in the following manner: 1) the re-orientation time is not instantaneous and an exponential distribution was used to pre-determine this time using experimentally determined mean re-orientation time; 2) The cell position is updated during re-orientations using overall mean cell speed (found similar to mean speed during re-orientations) and an empirical angle change distribution (see parameters); 3) the directional mode was assumed to be fairly straight and the minimum time spent in this phase was matched with the criterion used in bimodal analysis to at least three simulation time steps.

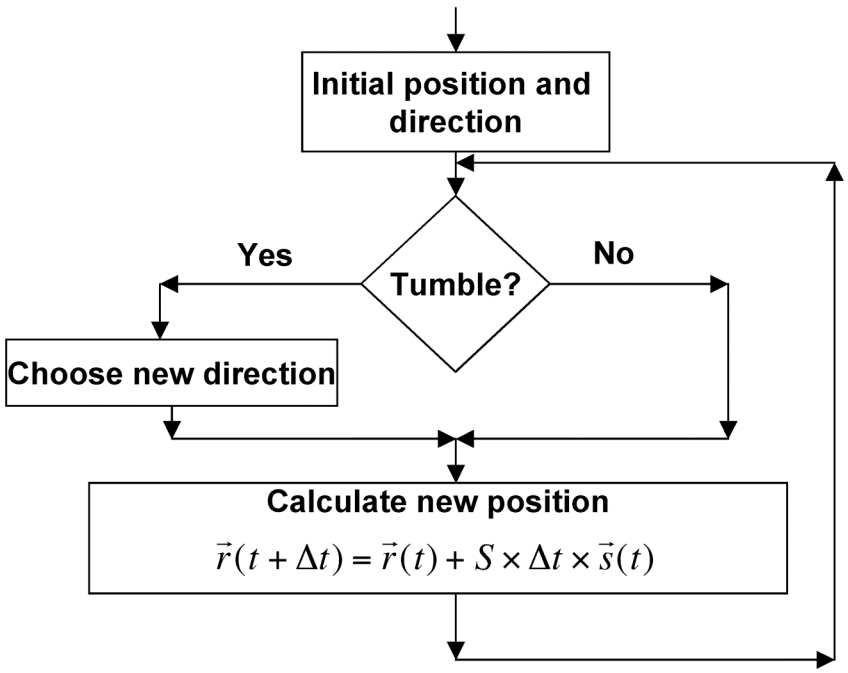

Figure 3.1: Logic diagram for cellular dynamics simulation of bacteria [35].

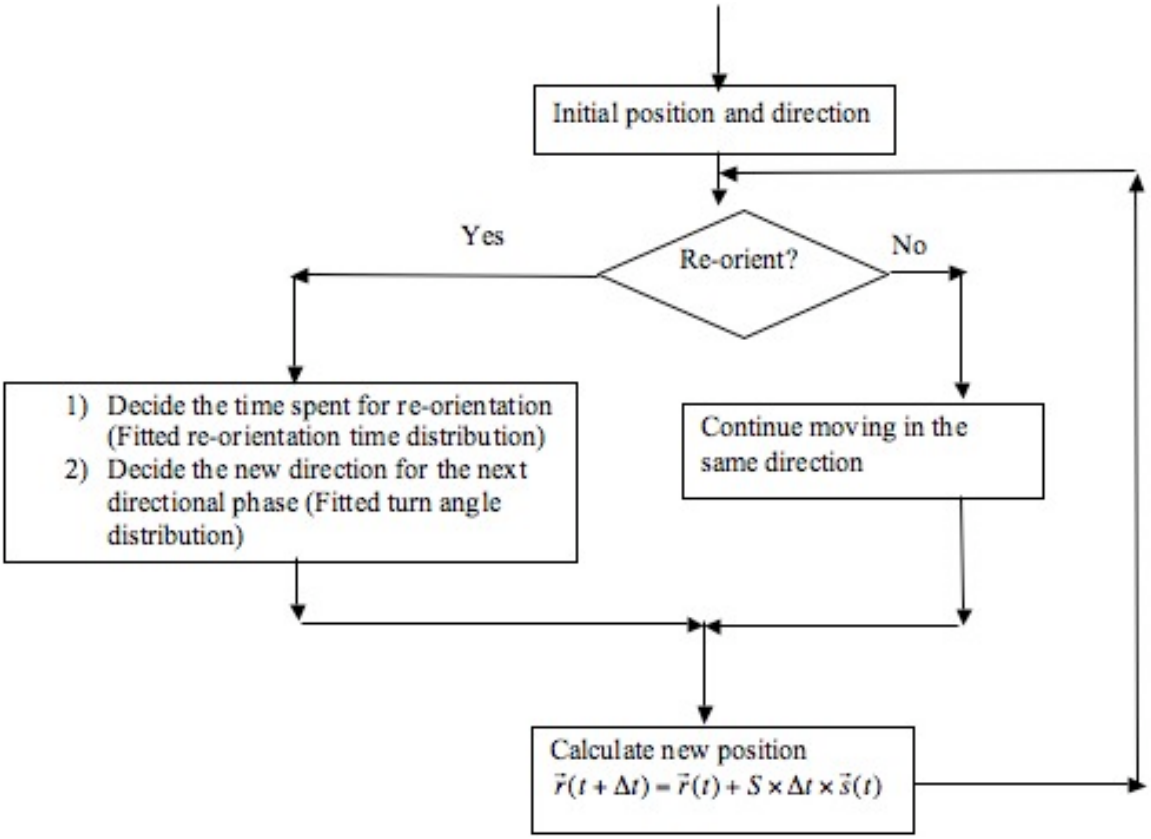

Figure 3.2: Modified logic diagram for cellular dynamics simulation of a mammalian cell.

3.3.3 Parameters

A simulation time step of 0.5 minute was used in all simulations which was also the time-resolution used to collect the cell migration data using video-microscopy. Each simulation was carried with at least 100 cells and 20000 simulation time steps. The simulation scheme was implemented in FORTRAN 95 and the "random_number" generator routine was used to generate random numbers between 0 and 1. The cellular dynamics simulations of MCF-10A cell random migration were performed based on experimental single cell dynamics using the scheme illustrated in Fig. 3.2. The parameters utilized to perform these simulations are defined below.

3.3.3.1 Re-orientation probability

The re-orientation probability ($p_{d\to r}$) is defined as the frequency of changing from directional to re-orientation mode (turn frequency, $f_{d\to r}$) times the simulation time step (Δt_{sim}). The frequency of changing from directional to re-orientation mode for a mammalian cell is defined as the total number of re-orientation modes ($n_{d\to r}$) divided by the total time spent in the directional modes ($T_{directional}$). A modified turn frequency (f_{sim}) was used in simulations in order to match the experimental frequency (see Results section).

$$f_{d\to r} = \frac{n_{d\to r}}{T_{directional}}$$

$$p_{d\to r} = f_{d\to r} \times \Delta t_{sim}$$

3.3.3.2 Re-orientation time ($t_{reorient}$)

The time spent for re-orientation ($t_{reorient}$) once the cell decides to re-orient is found from the re-orientation time distribution (modeled as an exponential distribution) of the

particular cell type. For an exponential re-orientation time distribution, $P(t_{reorient}) = \lambda e^{-\lambda t_{reorient}}$, the cumulative distribution from 0 to a value of $t_{reorient}$, is given by, $\int_0^{t_{reorient}} P(t_{reorient}) dt_{reorient}$.

Integrating, $F(t_{reorient}) = 1 - e^{-\lambda t_{reorient}}$

Taking logarithm of both sides, we get

$$t_{reorient} = \frac{\ln(1 - F(t_{reorient}))}{(-1/\bar{t}_{reorient})}$$

where, $F(t_{reorient})$ is the cumulative distribution function of the re-orientation times of the particular cell type; $\bar{t}_{reorient}$ is the mean re-orientation time. During the simulation, a random number picked between 0 and 1 is inserted in place of $F(t_{reorient})$ in the above equation.

3.3.3.3 Turn angle distribution (between runs)

The cumulative distribution function (*cdf*) values (from 0 to 1) are computed by summing the known probability density function (*pdf*) values of the turn angles ranging from $-\pi$ to $+\pi$. A third-order polynomial was found to give a good fit of the *cdf* of the turn angle *pdf* given as follows:

$$\phi = a \times F(\phi)^3 + b \times F(\phi)^2 + c \times F(\phi) + d$$

where, a,b,c,d are the fitting coefficients for the particular cell type; $F(\phi)$ is the *cdf* of the turn angle (ϕ) *pdf* and is equal to a random number between 0 and 1 during simulation. An example fit for the turn angle *cdf* is depicted in Fig. 3.3. The cumulative distribution function fit of the turn angle distribution for pBabe cell type used in the simulation is shown. The black filled circles is the experimental data and solid line is the polynomial curve-fit.

3.3.3.4 Angle change within the re-orientation phase

In order to update the position of a cell during a re-orientation phase, direction change at each time step during this phase is computed using the technique similar to the one used to find direction changes between directional modes. A sixth- order polynomial was a good fit of the *cdf* of the angle change *pdf* during the re-orientation phase.

$$\phi_t = a_t \times F(\phi_t)^6 + b_t \times F(\phi_t)^5 + c_t \times F(\phi_t)^4 + d_t \times F(\phi_t)^3 + e_t \times F(\phi_t)^2 + f_t \times F(\phi_t) + g_t$$

Where, $a_t, b_t, c_t, d_t, e_t, f_t, g_t$ are the fitting coefficients for the particular cell type; $F(\phi_t)$ is the *cdf* of the angle change during tumbles and is equal to a random number between 0 and 1 during simulation.

3.3.3.5 Cell speed

Using mean speed during re-orientation mode: The mean speed is simply defined as the total distance traversed by the cell divided by the time taken. The various parameters extracted from the bimodal analysis and used to perform random motility cellular dynamics simulations of different cell types are listed in Table 3.1.

Using speed versus directional mode time correlation during directional mode: We found a lot of variation in the experimental instantaneous cell speed. In order to incorporate this observed variability we used an empirical correlation table between cell speed and the given directional mode time. The correlation for the three cell types is shown in Fig. 3.4. One can see that smaller directional mode times are associated with a cell speed slightly higher than the overall mean cell speed. Since the directional mode time distribution was found to be exponentially distributed [37], the probability of smaller directional mode times is higher. Hence we found that the experimental mean squared displacement was

better matched by simulations when using a speed versus directional mode time correlation during directional mode rather than just using a mean overall cell speed. The use of a single mean overall speed underestimated the mean squared displacement (MSD) obtained from simulations when compared to experiments. The use of a single overall mean cell speed compared to using a speed versus re-orientation time correlation for re-orientation mode did not make any significant difference to the MSD trend.

Table 3.1: The parameter values used to perform the simulations of specific cell type.

Parameter	**Cell type**		
	pBabe	**neuN**	**neuT**
Turn frequency, $f_{d\to r}$	0.33	0.30	0.29
$\bar{t}_{reorient}$ (min)	4.55	5.07	4.34
Mean speed ($\mu m/\min$)	1.05	1.08	1.20
a,b,c,d	15.03, -21.99, 13.08, -3.03	17.69, -27.66, 16.41, -3.42	17.34, -25.96, 14.40, -2.86
$a_t,b_t,c_t,d_t,e_t,f_t,g_t$	-35.63, 242.36, -462.83, 372.92, -134.93, 24.81, -3.39	-33.33,181.84, -324.58, 262.39, -103.11, 23.67, -3.62	-36.86, 229.08, -419.68, 332.62, -122.61, 23.83, -3.24

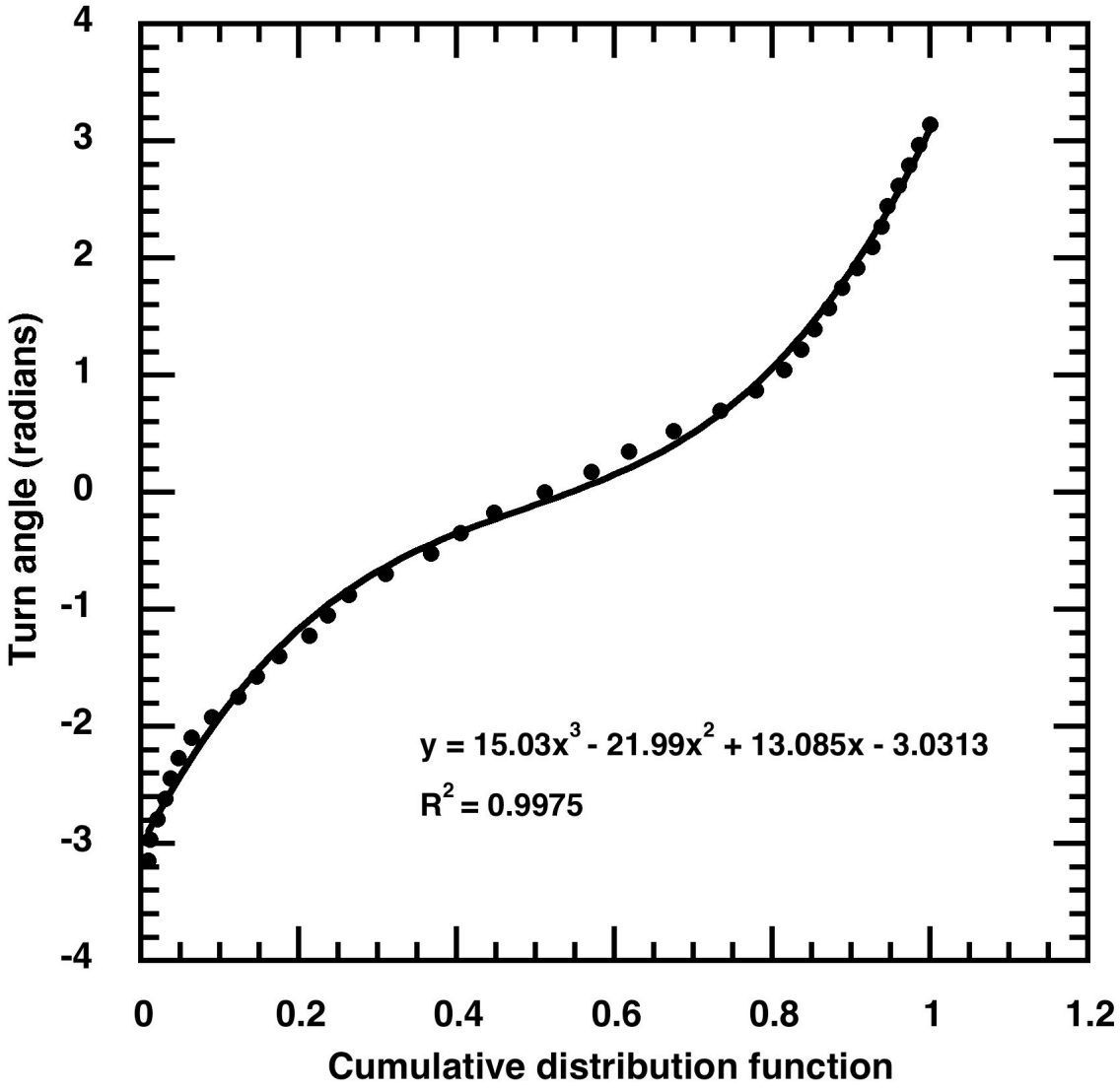

Figure 3.3: Cumulative distribution function fit of the turn angle distribution for pBabe cell type for use in the simulation. The black filled circles are the experimental data and solid line is the polynomial curve-fit.

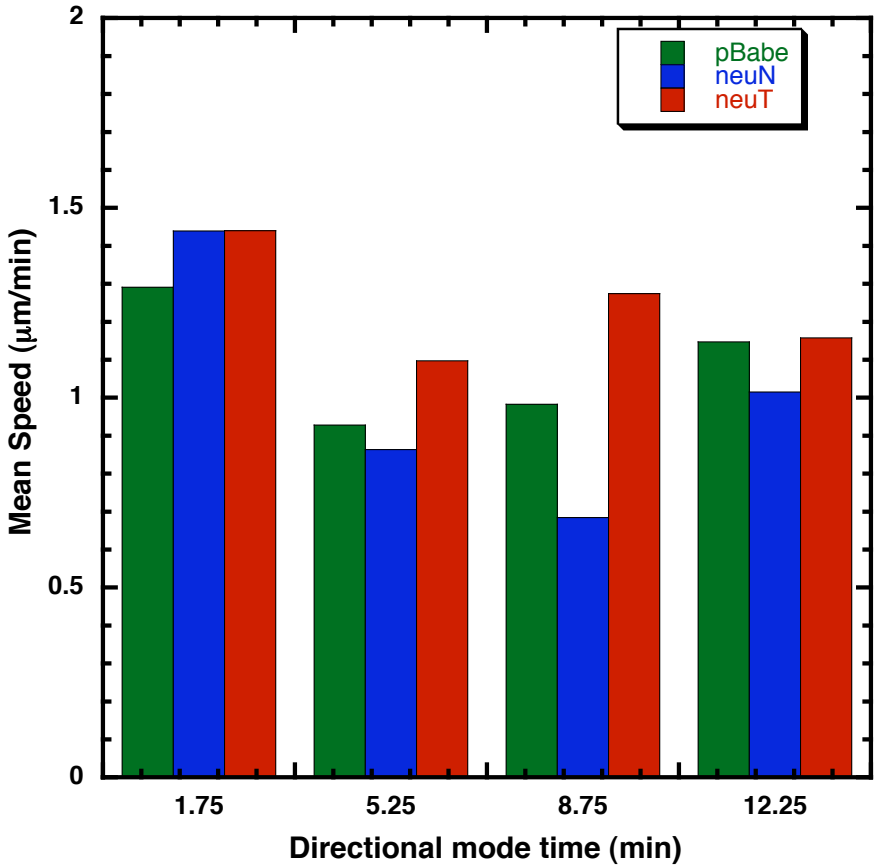

Figure 3.4: Speed versus directional time correlation for the three cell types. The variability in cell speed associated with different directional mode times is evident. Smaller directional mode times (bin of 1.75 minute and which are correlated with slightly higher cell speed (1.5 $\mu m/\min$) than the mean cell speed (~1 $\mu m/\min$)) are more probable since the mode times are exponentially distributed.

3.4 Simulations

The cellular dynamics simulation scheme presented here is based on a simple model for single cell migration (which involves alternating directional and re-orientation modes). We have not taken into account cell-cell adhesion or other types of interactions between cells; however this is consistent with the experimental data in which adhering and dividing cells were filtered. Furthermore, we only consider random migration of epithelial cells on 2-D substrates and incorporate the experimentally extracted parameters of random migration experiments of the concerned epithelial cells. The migration tracks of several single cells were recreated using the simulations for a timescale much greater than the 2 hours for which cells were tracked in experiments.

The main aim of these simulations was to investigate the diffusive properties of single epithelial cells (in the absence of any exogenous addition of a biasing component) by following the cells until the cells reach diffusive regime. We know that normal diffusion arises when mean squared displacement (MSD), $< \left(\vec{r}(t) - \vec{r}(0)\right)^2 >$ scales as t^{α} where, $\alpha = 1$) where $\vec{r}(t)$ is the position of the cell at time t. Anomalous diffusion arises when $\alpha \neq 1$, with $\alpha < 1$ corresponding to sub-diffusive motion, $\alpha > 1$ to super-diffusive motion and 'ballistic motion' for the case of $\alpha = 2$.

We compared the MSD of the simulated cells (for the three cell types, expressing different versions of Her-2 receptor) and performed simulations till a diffusive regime was reached. From the linear diffusive regime, the random motility coefficient for each cell type was estimated. Scatter plots were also used to qualitatively determine which cell type had faster diffusion characteristics.

3.5 Results and Discussion

3.5.1 Simulated trajectory

An example 2 hour simulated cell trajectory of a neuN cell is shown in Fig 3.5 (*left figure)*. The re-orientations are indicated by triangles. A cell is assumed to remain stationary during these re-orientations, which would be the case for bacterial tumbles. The directional modes are approximated as straight lines. The simulation was modified to incorporate cell motion during the re-orientation phases. The procedure described in section 3.3.3 was used to compute the direction change during re-orientation phases and the cell is updated using a mean overall cell speed during re-orientation mode. A simulated neuN cell trajectory from such a simulation is depicted in Fig 3.5 (*right figure)* and represents a mammalian cell track better than that on the left.

3.5.2 Matching the bimodal analysis scheme

The trajectories from the simulations were used as input for the bimodal analysis scheme described in Chapter II (i.e., the simulation results were treated as pseudo-experimental data) to see if the computational trajectories would yield directional and re-orientation data the same as was input to the simulation. To correctly match the turn angle distribution from simulated data to that from experimental, the simulation was modified to replicate the bimodal analysis scheme correctly, namely; the directional mode lasted for at least three simulation time steps (3 frames characterized a directional mode in bimodal analysis) and the transition between the directional and re-orientation mode was such that the absolute angle change was greater than or equal to 45^{o}.

Subsequently, it was found that in order to obtain a final turn frequency in a simulation close to that found in experiments for a given cell type, an input turn frequency higher than that found in experiment was required. The following relation was used to calculate the input frequency for the simulations: $f_{sim} = \frac{n_{d\to r}}{(T_{directional} - n_{d\to r} \times 2 \times \Delta t_{sim})}$, where the denominator represents the corrected total directional mode time in simulations.

3.5.3 Random motility coefficient

We found earlier that the experimental MSD of the three cell types versus time on a log-log scale lies between the slope 2 (the 'ballistic regime') and slope 1 (the 'diffusive regime'). Hence, the two-hour experimental tracking time is not long enough for the cell motion to enter the diffusive regime, so that the random motility coefficient cannot be estimated for the relatively slow-moving MCF-10A cells and warrants the tracking of these cells for several hours to days. This problem can be circumvented by performing 'cellular-dynamics' simulations long enough to reach the diffusive regime. This may also give us some insight into the differences in the diffusive characteristics between the control (pBabe) and the Her-2 over-expressing cell line (neuT). Fig. 3.6 shows the scattering of 100 cells of each cell type (green: pBabe, blue: neuN and red: neuT) starting from origin over a course of 12 hours (close to one proliferation time). The position of a cell after every 5 minutes has been shown. One can see that the neuT (red) cell type scatters farther compared to the pBabe (green) and neuN (blue) implying that Her-2 over-expressing cells have a higher random motiltiy coefficient. The MSD of the three cell types from the simulations are compared to those from experiments on log-log scale in

Fig. 3.7. We can see that the MSD enters the diffusive regime (slope 1) eventually (~2 hours). We used the data from >1000 minutes to estimate the diffusion/random motility coefficient (μ) of the cells. For the 2-D data under consideration, $< \left(\vec{r}(t) - \vec{r}(0)\right)^2 >= 4\mu t$ in the diffusive regime and hence the slope of MSD versus time would give an estimate of μ (Table 2).

We had also estimated the value of persistence indices for the various MCF-10A cell types using the turn angle distribution information and found increasing persistence with increasing level of Her-2 expression from pBabe, neuN and neuT cells consistent with the hallmark of cell migration in invasive tumors [63] and in cells with over expressed levels of Her-2 receptor which showed higher directional persistence in an *in vitro* wound closure assay [47]. We find through our simulations that the random motility coefficient of the neuT cell type (over expressing Her-2) to be twice as high compared to the control pBabe. The 2-hour experimental data is not enough for estimation of random motility coefficients and cells need to be tracked for longer times. Since the overall cell speed for the three cell types are not overwhelmingly different from each other (~ 1 $\mu m/\min$), it is the turn angle distribution (directional persistence), which contributes to the higher random motility of the neuT cell type.

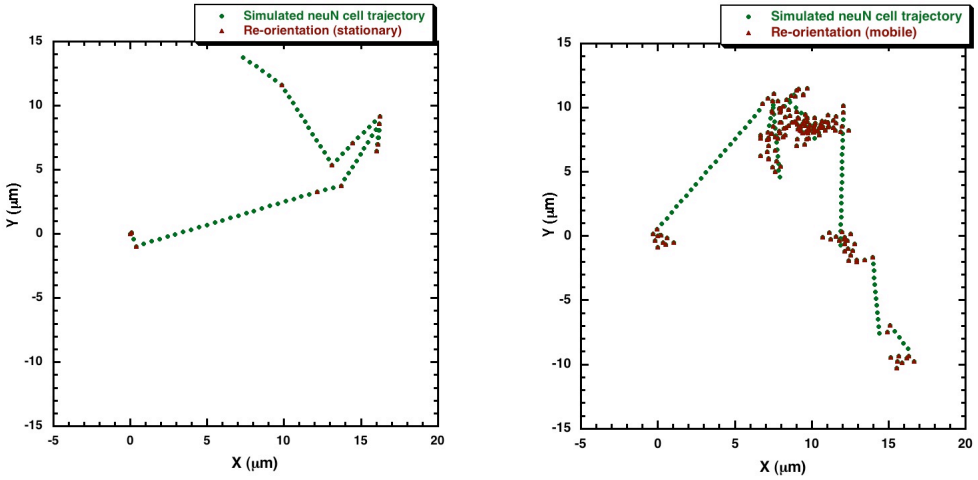

Figure 3.5: A simulated neuN cell using a simulation time step of 0.5 minute. The cell remains stationary during the re-orientation phase (*left*) and a cell is in motion during re-orientation (*right*).

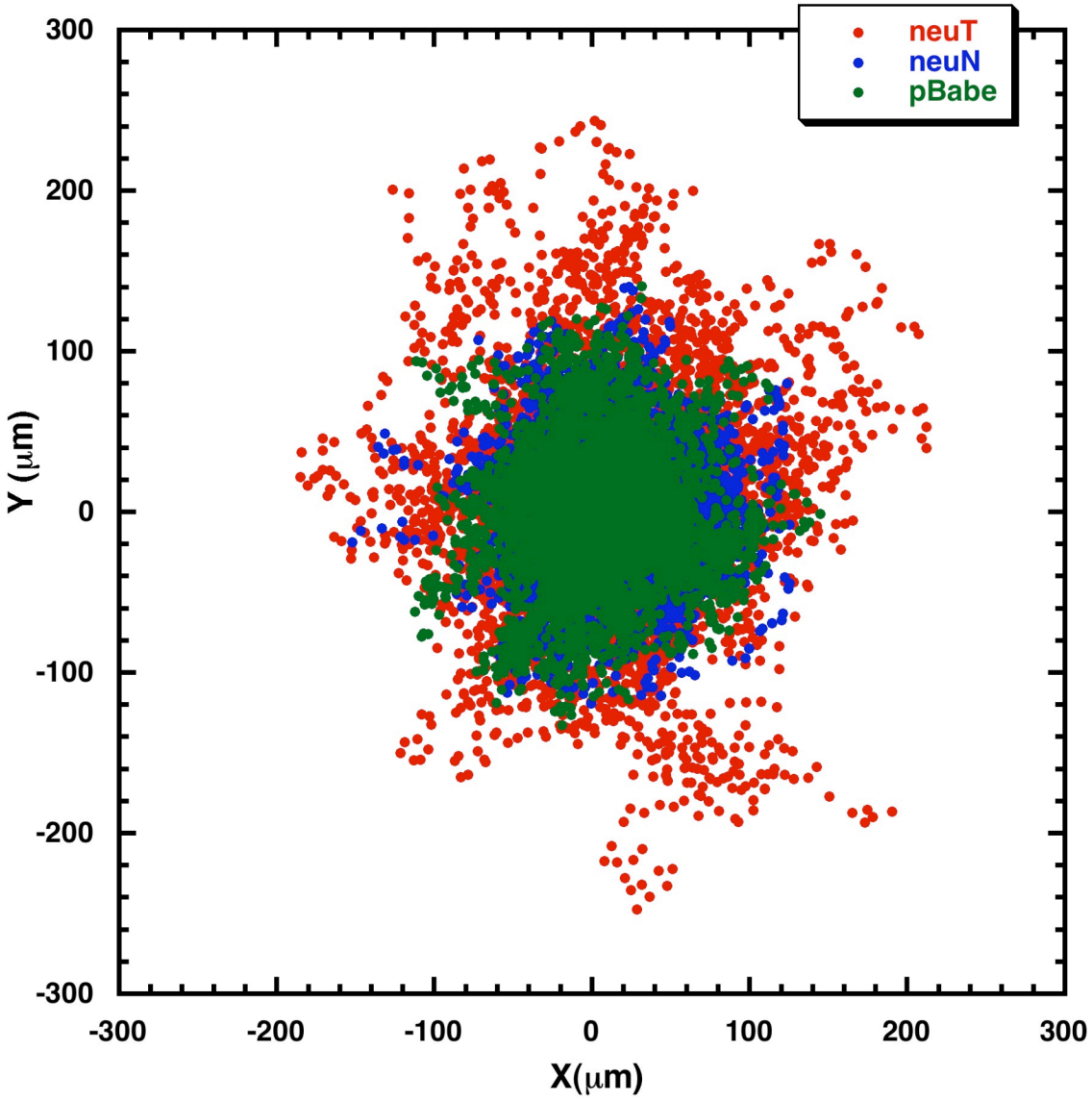

Figure 3.6: Evolution of 100 simulated cells of different cell types over 12 hours starting from origin. All the pBabe cells are denoted by green filled circles while neuN by blue and neuT cell types is denoted in red. The position of cell every 5 minutes has been plotted.

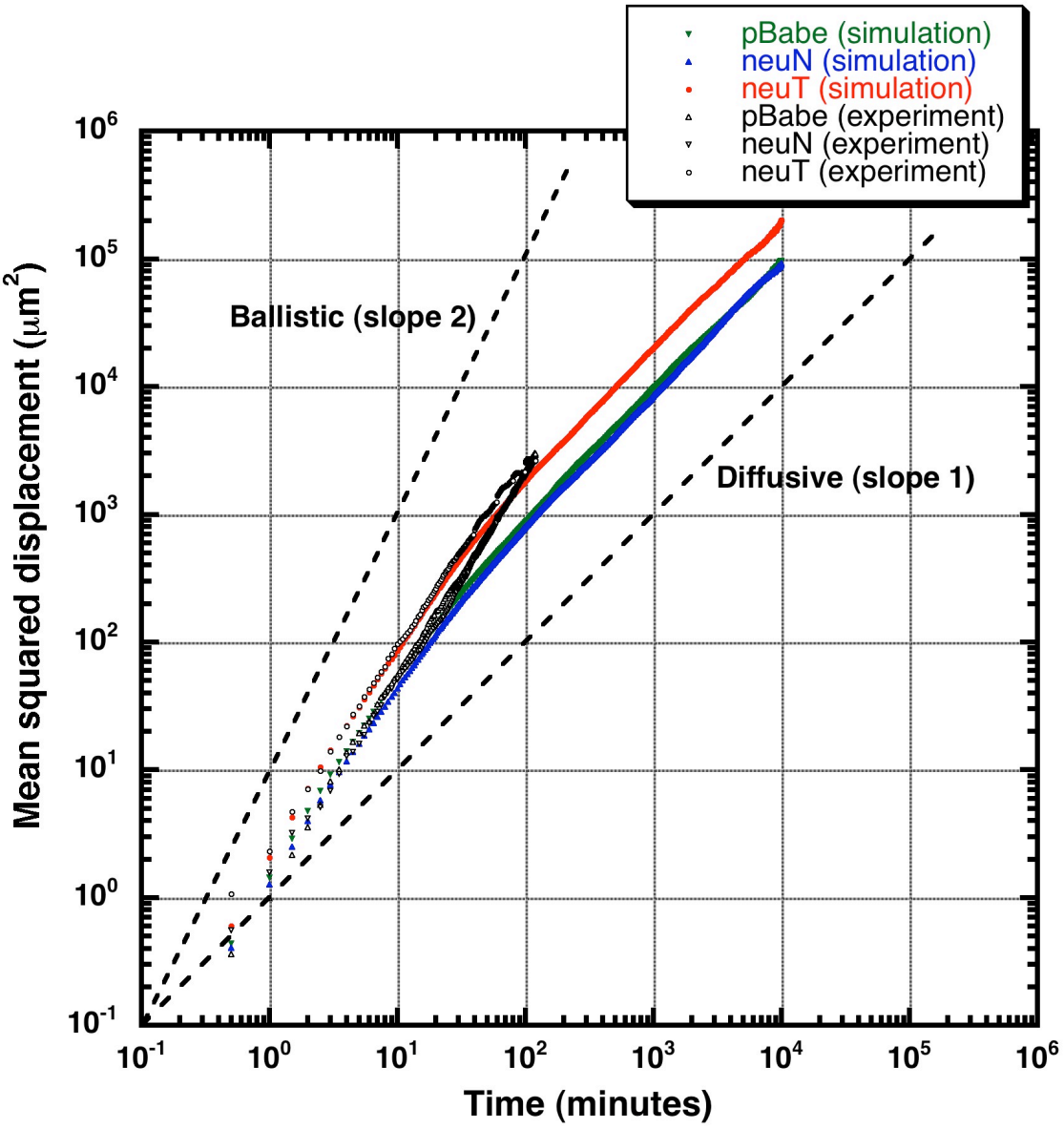

Figure 3.7: Comparison of mean squared displacement from experiment to that from simulations for the three cell types expressing different versions of Her-2 receptor.

Table 3.2: Random motility coefficient values of the three cell type as determined from the simulations.

Cell type	**Random motility coefficient** ($\mu m^2/\min$)
pBabe	2.31
neuN	2.28
neuT	4.60

We simulated the population level behavior of mammary epithelial cells expressing different versions of Her-2 using experimentally extracted parameters for each cell type. Although, the current model is based on single cell random migration, which excludes other phenomena such as cell-cell adhesion and chemotaxis, it provides a basic framework to which more complexities could be added. We estimated the random motility coefficient using cellular dynamics simulations (without making any prior model assumptions) incorporating more realistic experimental cell dynamics and looked into the effect of Her-2 over-expression on single cell motility. We find that the neuT cell type have higher random motility compared to the control, pBabe.

The experimental tracking data of MCF-10A cells chemotaxing in the presence of a chemokine such as EGF could be analyzed with the bimodal analysis to get individual cellular parameters of chemotaxis. We can then hope to extend the 'cellular dynamics' simulation strategy developed for bacterial migration for both the random migration and chemotaxis of the mammary epithelial cells using the individual cellular parameters developed from the bimodal analysis. This simulation strategy can also be modified to incorporate cell-cell adhesion, haptotaxis and other cell migration strategies to simulate

cell migration more accurately. These simulations can be performed in diffusive regime to get an estimate of the cancer cell parameters such as the random motility coefficient and then chemotaxis coefficient, which can then be fed, into an existing tissue scale model of tumor invasion [22, 62].

3.6 Conclusions

In summary, cellular dynamics simulation scheme (originally developed to simulate bacterial chemotaxis) was used to simulation random migration of mammary epithelial cells expressing different versions of Her-2 receptor and the neuT cell type (expressing oncogenic version of Her-2 receptor) was found to have higher random motility coefficient.

CHAPTER IV

HUMAN MAMMARY EPITHELIAL CELLS EXHIBIT A BIMODAL CORRELATED RANDOM WALK PATTERN

4.1 Abstract

Organisms, at scales ranging from unicellular to mammals, have been shown to exhibit foraging behavior by demonstrating that their migration can be described by random walks whose segments confirm to Lévy or exponential distributions. For the first time, we present evidence that single cells from multi-cellular organisms follow a similar foraging pattern. Cellular tracks of MCF-10A pBabe, neuN and neuT random migration on 2-D plastic substrates, analyzed using the *bimodal analysis* described in Chapter II, were found to reveal a bimodal correlated random walk (BCRW). We find two types of exponentially distributed correlated flights (corresponding to what we refer to as the directional and re-orientation phases). These flights each have a specific form of turn angle distribution representing the correlation between move step-lengths within flights. We analyzed these flights using different methods (logarithmic binning with normalization, survival frequency plots and maximum likelihood method) to determine the presence of any Lévy modulation in the flights versus exponential model. We did not find any evidence of a power-law behavior in the flight lengths, in agreement with the survival frequency distributions. Since the presence of non-uniform turn angle

distribution of move step-lengths within a flight and two different types of flights, we propose that the epithelial random walk is a BCRW comprising of two alternating modes with varying degree of correlations, rather than a simple persistent random walk. A BCRW model correctly matches the super-diffusivity in the cell migration paths in the absence of any biasing cues (haptotaxis or chemotaxis) as indicated by simulations based on the BCRW model.

4.2 Background

Cell migration is an important process for a wide range of domains from bacteria to mammals. For prokaryotes (e.g., bacteria), migration is important to locate food sources [1]. Similar goals may apply to unicellular eukaryotes (e.g., *Dictyostelium*). In contrast, in "higher" multi-cellular eukaryotes (e.g., mammals) cell migration is involved in physiological processes as well as pathogenic conditions such as cancer metastasis [11]. Mammalian cell migration is generally thought of as having a "purpose" (such as embryogenesis [28] and immune response [75]) other than locating nutrients and it is believed that these cells follow orders from a higher "programming center". When these orders are misinterpreted or disregarded, cancer may occur. This work, instead, is informed by a different premise: namely, that individual cell migration in random motility conditions can be interpreted as a problem of how to efficiently perform a search to locate randomly distributed "target items" (such as nutrients and growth factors) which could only be detected in limited vicinity. This is analogous to animal foraging problem where animals come to adopt an optimal search strategy to locate food.

Random walk (RW) theories have been used to model animal displacements to explain optimal foraging, predator-prey relationships, etc. For long-times, animal

movements can be modeled as uncorrelated RWs with normal diffusion (mean squared displacement (MSD), $< \left(\vec{r}(t) - \vec{r}(0)\right)^2 >$ scaling as t^{α} where, $\alpha = 1$) [27, 76], where $\vec{r}(t)$ is the position of the animal at time t and the average (< >) is over all the members of the population. Anomalous diffusion arises when $\alpha \neq 1$, with $\alpha < 1$ corresponding to sub-diffusive motion, $\alpha > 1$ to super-diffusive motion and 'ballistic motion' for the case of $\alpha = 2$. These relationships were derived in Chapter I.

The directional persistence in animal movements has been modeled using correlated random walks (CRWs) or Lévy Walks (LWs) [77]. CRWs have an exponentially decreasing distribution of move step-lengths (distance traveled in one sampling time) [78] and the shape of the turn angle distribution between these move step-lengths controls the directional memory. LWs or flights [79-81] are RWs wherein long flights can be separated by shorter jumps. These walks are described by the power-law probability distribution function for the flight step-length l, given by $P(l) \approx l^{-\mu}$, $1 < \mu < 3$ where μ is the 'Lévy index'. The MSD in LWs always scales as t^{α} where $\alpha > 1$ while a CRW eventually loses super-diffusivity reaching normal diffusion once the correlation is lost. Lévy motion converges to Brownian motion for $\mu \geq 3$.

LWs have been frequently used to model animal displacements in ecology. It has been shown that the efficiency of animal searches incorporating LWs is higher than those using CRWs [77] since the chance of returning to the same place with Lévy flights is less [82], optimizing the predator-prey encounter [83]. Simulations also revealed that for animal foragers feeding on randomly distributed target sites an inverse square power-law distribution of flight lengths in Lévy motion is an optimal solution [82]. Subsequently, experimental studies also reported that organisms ranging from birds [84] to mammals

[78] adopt Lévy motions with $\mu \approx 2$. LWs have been reported in diverse species from marine predators [78], spider monkeys [85], micro-zooplankton [86], soil amoebas [87], freshwater *Hydra* cells [88] and humans [89]; initially, albatrosses were thought to exhibit Lévy behavior [84].

Recently, however, the biological existence of Lévy flights has been questioned and it has been suggested that not all the reported experimental studies follow Lévy behavior [90-93]. It has also been shown that combination RWs such as composite Brownian walks (CBWs) may have a higher search efficiency than LWs and these composite, two-search–mode walks can generate patterns that look similar to LWs [90, 94]. Of particular note is the recent work showing albatross motion is inconsistent with LW behavior [92]. The survival distributions (cumulative frequency of lengths greater than a given length) can correctly identify true Lévy behavior. Also, methods where weights of two competing models (Lévy versus exponential) are calculated (maximum likelihood estimates along with Akaike weight calculations [91, 92] could be useful to identify the true model to describe the observed search patterns.

The persistent random walk model (PRW) [49] (a form of CRW) has often been used to model mammalian cell migration. We are not aware of any reported attempt to decipher the search pattern of individual mammary epithelial cells in low-cell density conditions in the absence of any biasing cues. Does the random motility of eukaryotic, mammary epithelial cells follow Lévy statistics or not? Recent studies have indicated that the search strategy of *Dictyostelium* (eukaryotic cell) in the absence of external cues is a persistent cell motion [95, 96]. Van Haastert and coworkers also reported that starved amoeboid cells exhibit correlated random walk food search strategy by extending their

run lengths [97]. The method of bimodal analysis [98] developed as part of this dissertation work (Chapter II), segregates the motion of cells into directional or re-orientation phases based on nucleus tracks of epithelial cells analogous to the segregation of amoeboid tracks into runs (based on splitting pseudopods) and turns (based on *de novo* pseudopods) in the recent work by Van Haastert and coworkers [96, 97, 99]. We report here that the epithelial cell migration paths on 2-D plastic substrates in the absence of any chemo-attractant gradients follow general features of a bimodal correlated random walk model (BCRW).

The BCRW could be thought of as a modified CRW comprising of two alternating modes with varying degree of correlations. This is analogous to an intermittent search strategy having a fast phase oblivious to the presence of any target and a slow responsive search phase to locate the target [94]. Some of the salient characteristics of this proposed BCRW are: i) flights follow an exponential distribution; ii) move step-lengths comprising the flight are correlated through turn angles randomly drawn from a distribution such as a Gaussian distribution and iii) move step-lengths within the flight are randomly drawn from an exponential distribution.

4.3 Materials and methods

4.3.1Bimodal analysis ([98], Chapter II) to identify directional and re-orientation flights

We use the results of the bimodal analysis [98] method developed by us to analyze the random migration data of three cell types derived from the MCF-10A human mammary epithelial cells, expressing the pBabe vector alone (pBabe), or the normal (neuN) or

transforming (neuT) versions of the rat Her 2/Neu oncogene. The migration of cells was followed under random motility conditions without the presence of any externally added chemo-attractant gradients, using time-lapse video-microscopy. The details of the cell culture routine used, cell motility experiments performed and the bimodal analysis technique are elaborated in Chapter II and reference [98]. Briefly, the cells were followed for at least two hours in all the experiments and at least five sets of experiments were performed. We use the bimodal analysis results of data collected with a resolution of 40x (1 pixel ≡ 0.163 μm) and a video-microscopy sampling interval of 0.5 minutes. Trajectories of cells that were immotile (less than two cell diameters), adherent to other cells, or undergoing mitosis were not considered for the analysis.

The bimodal analysis [98] segregates the cellular trajectories of individual mammalian cells, specifically MCF-10A cells (human mammary epithelial cells), into two alternating modes (directional and re-orientation phases) based on a framework similar in spirit to that used in the analysis of bacterial motility [29, 31]. An example neuT trajectory with the directional and re-orientation flights is depicted in Fig. 4.1 (top panel). A directional flight length is the summation of all the consecutive move step-lengths during the directional phase and similarly, a re-orientation flight length is the summation of a series of all the move step-lengths during the re-orientation phase [77]. We define net flight length as the displacement during the given flight.

4.3.2 Survival frequency distributions

The survival frequency of flight lengths is defined as the cumulative frequency of flight lengths greater than any given threshold. For an exponential distribution $P(x) = Ae^{-\lambda x}, x \in [a,b]$; the cumulative distribution function (cdf) (between the bounds

a,b) for flight lengths less than any x is given by, $1-cdf=(A/\lambda)e^{-\lambda x}$. The bounds in our data were $a=0$ and $b\approx 20\mu m$. Taking logarithm on both sides, we get,

$$\ln(1-cdf)=\ln(A/\lambda)-\lambda x \qquad (4.1)$$

Equation (4.1) is of the form $y=mx+c$, and hence a plot of $1-cdf$ versus x on log-linear scale yields a straight line for an exponential distribution. The slope $m=-\lambda$, is the inverse of the average value of x. A bin size of $1\,\mu m$ was used to bin the flights.

4.3.3 Logarithmic binning of flights

The presence of Lévy behavior was investigated using the logarithmic binning with normalization method (LBN method) described in the Sims et. al. paper [93]. Logarithmic binning involves increasing the bin sizes in a geometric sequence so that the size of the k^{th} bin is 2^k where k was varied from -2,-1,0,1,2,3,... The normalized frequency was calculated as the ratio of observed frequency to the product of bin width (for a given bin) and number of data points.

4.3.4 Statistical analysis

All statistical analysis was done in MATLAB software package (MathWorks, Natick, MA). The Lilliefors test (lillietest.m) revealed that the data were non-paramteric. A two-sample Kolmogorov-Smirnov test (kstest2.m in MATLAB) was used to determine statistical significance between the mean net displacements in the directional (d_d) and re-orientation (d_r) phases for a given cell type. A p-value <0.05 indicates significant difference. Statistical analysis for estimating the fitting parameter for exponential distribution (λ) from the survival frequency distributions along with associated r^2 (correlation coefficient) was performed using regstats.m in MATLAB, which also gives

the p-values associated with the slopes using t-test. The mean value reported in Tables 4.1 and 4.2 for a given cell type is the mean of mean value for each cell (pBabe (n=15), neuN (n=15), neuT (n=12)) in the population while error bars are standard deviations in the means.

The PRW model-fit of the experimental data was performed by fitting the experimental MSD using the following equation: $\left\langle d(t)^2 \right\rangle = 2n\mu\left[t - P(1-e^{-t/P})\right]$, where $\left\langle d(t)^2 \right\rangle$ is the MSD, P is the persistence time and μ the random motility coefficient, for a system with n dimensions. The squared relative difference error (RDE) for a given model i is defined as, $(RDE(t))_i^2 = [(MSD_{\exp}(t) - MSD_i(t))/(MSD_{\exp}(t))]^2$, where model $i = PRW, BCRW$ and $MSD_{\exp}(t)$ is the experimental MSD at a given time t.

4.3.5 Maximum likelihood estimates (MLE) and Akaike weights

We used likelihood estimates and Akaike weights [91, 92] to determine which of the two models (exponential or power law) fit our experimental data. The probability density functions for the two models and the corresponding maximum likelihood estimate of the model parameter are as follows [92, 100]:

Power law model

$$f_1(x) = Cx^{-\mu}, x \geq a \tag{4.2}$$

$$\mu = 1 - n\Big/\left(n\log a - \sum_{j=1}^{n}\log x_j\right) \tag{4.3}$$

Exponential model:

$$f_2(x) = \lambda e^{-\lambda(x-a)}, x \geq a \tag{4.4}$$

$$\lambda = 1\Big/\left(\sum_{j=1}^{n} x_j/n - a\right) \tag{4.5}$$

One parameter was estimated for each of the two models considered (exponential (λ) and power law (μ)) using equations 4.3 and 4.5. The equations used for calculating Akaike weights are same as the ones detailed in box1 in [92]. Table 4.3 shows the MLE of parameters for both models along with the Akaike weights for the flight lengths of the three cell types. The exponential model is highly favored in all cases.

4.3.6 BCRW model and simulations

The BCRW could be thought of as a modified CRW comprising of two alternating modes with varying degree of correlations. This is analogous to an intermittent search strategy having a fast phase oblivious of the presence of any target and a slow responsive, search phase to locate the target [94]. Some of the salient characteristics of this proposed BCRW are: i) flights follow an exponential distribution; ii) move step-lengths comprising the flight are correlated through turn angles randomly drawn from a distribution such as a Gaussian distribution and iii) move step-lengths within the flight are randomly drawn from an exponential distribution.

4.3.6.1 BCRW simulations

The PRW fit gives a persistence time of around 10 minutes indicating early loss of super-diffusivity unlike the experimental mean squared displacement. Hence, we performed simulations of the epithelial cell migration based on the proposed BCRW framework to investigate the nature of diffusive properties of such a system in a long time limit. In our simulations for the BCRW exhibited by epithelial cells, exponential flights were generated by sampling an exponential distribution $P(l) = e^{(-l/\lambda)}/\lambda$ where l is flight length and λ is the mean flight length. In order to generate the flight lengths from the

exponential distribution, the inversion method was used, *i.e.*, flight length was generated from the exponential distribution by inserting a uniform random number, $0 \le r \le 1$, into the inverse of the cumulative distribution of the exponential function, $l = -\lambda \ln(r)$. In the BCRW, the λ in the directional (λ_1) and reorientation (λ_2) phases can be different. Moreover, because the flight length is of finite size, the maximum flight length, $l_{\max}$, can be defined according to the particular cell type and the occurrence of an undesirably long flight length can be avoided. We also had a minimum cut-off for the flight length, $l_{1\min}$ and $l_{2\min}$, for directional and re-orientation flight, respectively.

The step-lengths in a flight are not straight-line move step-lengths but are correlated through a series of turning angles from a distribution such as the Gaussian distribution $P(\theta) = \exp\left(-(\theta - \theta_0)^2 / 2\sigma^2\right)\sigma\sqrt{2\pi}$ where θ is the turning angle (*i.e.*, deviation from the previous direction), θ_0 the mean turning angle (in our BCRW simulation $\theta_0 = 0$), and σ the standard deviation of the distribution. Standard deviation, σ, in the Gaussian distribution function determines directionality or persistence of step movement, *i.e.*, smaller σ makes the Gaussian distribution narrow and the path more persistent. In the BCRW, two standard deviation values, σ_1 and σ_2, were used in directional and re-orientation flights, respectively. In addition, a correlation between two neighboring directional phases is described by using the Gaussian distribution of turning angles between two directional flights with a standard deviation, σ_3.

The step-lengths, x, within the flights are randomly drawn from an exponential distribution $P(x) = e^{(-x/\lambda)}/\lambda$ where λ is the mean move step-length in flights. In order to generate the move step-lengths from the exponential distribution, the inversion method

was used as before. To test the validity of the BCRW model, the experimental mean squared displacement of the cells is compared with that obtained from the simulation. We find that all the individual step lengths as well as flight lengths in the cellular tracks are exponentially distributed and we use this information to perform a simulation based on proposed BCRW framework.

The turn angles between the individual steps in each flight type is associated with certain degree of persistence or 'ρ' parameter associated with a wrapped Cauchy distribution [77]. The turn angle distribution within the directional flights is narrow compared to the spread out re-orientation flight angle distributions as illustrated later on in the Chapter. This implies a higher value of ρ (more persistence) associated with directional flights. We find that a Gaussian distribution provided a better fit to the angle distributions compared to a wrapped Cauchy distribution. A Gaussian distribution has been used earlier to fit the turning angles [101, 102]. We related the standard deviation of the Gaussian distribution to degree of persistence, a higher value indicating lesser persistence. The neuT cell type was found to be more persistent as the turn angle distribution between the directional flights has the least standard deviation compared to pBabes and neuNs. The standard deviation of turn angle distribution in a directional flight is smaller than that of a re-orientation flight. This was incorporated in the BCRW simulations.

4.3.6.2 Simulation parameters

In order to obtain mean squared displacement of cells from a BCRW simulation, we generated 100 independent trajectories during simulated 2500 minutes in length, which is not feasible in an experimental situation, however this gives an important insight into the

characteristics of cell motility. Parameter values used in the BCRW simulation of neuN cell type are as follows: $\lambda_1 = 4.39\mu m$, $\lambda_2 = 4.58\mu m$, $l_{\max} = 16\mu m$, $l_{1\min} = 2\mu m$, $l_{2\min} = 0.5\mu m$ $\sigma_1 = 0.08$, $\sigma_2 = 2.75$, $\sigma_3 = 0.5$, and $\lambda = 0.53\mu m$.

4.4 Results and discussions

We segregated epithelial cell migration tracks into alternating directional and re-orientation modes using our *bimodal analysis* method [98]. Some example trajectories with the directional and re-orientation flights flagged are depicted in Fig. 4.1 (*top*: neuT and *bottom*: pBabe cell type). The direction changes between consecutive directional flights in epithelial cell random migration was found to be non-instantaneous and the cell was found to spend considerable time in the re-orientation phase. The fundamental idea of a BCRW is applicable for epithelial cell migration, as we have two types of alternating flights (directional and re-orientation flights) with a Gaussian distribution for the turn angles within each flight type and an additional one between two neighboring directional flights. We analyzed the random migration data of MCF-10A pBabe, neuN and neuT human mammary epithelial cells with respect to the distribution of flight lengths (both total distances, 'flight' and net displacement, 'net flights'), within the above-described general framework of a BCRW to test its applicability to mammalian cell migration.

We had earlier reported that the mean d/t ratios (ratio of displacement to distance for a given flight) in directional phases are higher than those of re-orientation phases [98]. Specifically, we find that the mean displacements (net flight length) during the directional phases (d_d) are higher than those during re-orientation phases (d_r) (Table 1) while the mean total distance covered in directional phase (t_d) is not statistically different from that during re-orientation phase (t_r) (Table 4.2). The trends in the net displacements

are also implicated in the box plot of the displacements during the different flights for the three cell types (pBabe (n=15), neuN (n=15), neuT (n=12)) (Fig. 4.2).

In order to test the presence of any Lévy statistics in the flight lengths, we used three different methods to analyze the distribution of flights. The first method uses the cumulative distribution/rank frequency plots (flight lengths greater than a given threshold) also referred to as survival distribution [90, 100]. We use the information that the survival distribution would be a straight line on a log-linear scale (probability versus flight length) for an exponential distribution while a true power-law distributed data would be revealed as a straight line on a log-log scale. Likewise, we tested the survival distributions of directional and re-orientation flight distances (referred to as 'flight length') and displacements (referred to as 'net flight length') for the three cell types. Intriguingly, we found that the flight length survival distributions (both directional and re-orientation) (Fig. 4.3a, *left* panel) for all cell types on a log-linear scale fitted well with a straight line (statistics, Table 4.4). Similarly, the net flight lengths (Fig. 4.3b, *right* panel) also exhibited similar trends (statistics, Table 4.4). This revealed that the flight lengths/net flight lengths of individual human mammary epithelial cells in random motility assays deprived of any directional bias follow exponential probability. This is in contrast to the recent report of foraging behavior of large animals such as sharks as a whole organism [78] which showed Lévy behavior. Our result is, however, consistent with the search strategy in *Dictyostelium* that was reported to be lacking any Lévy statistics [95, 97] and with the revised results on motion of albatrosses [92]. This may indicate the differences in movement patterns of individual eukaryotic cells from those of the organism (as a whole) that comprise these cells. Motile flagellated prokaryotic

bacterial cells have Poisson distributed runtimes [29] and, given the essentially constant speed with which the bacterial cells move, the run length distribution of bacteria can also be expected to be exponentially distributed.

The slope, λ of the straight-line fits (Table 4.4) on the log-linear survival distributions represents the inverse of the mean flight length. A higher λ would indicate a smaller mean flight length. The λ value was found to be higher for the re-orientation net flight compared to the directional net flight consistent with the results in Table 4.1, giving confidence in the straight-line fits.

We also used logarithmic binning with normalization method (LBN [93]) to analyze 1140 flights (directional and re-orientation, identified using bimodal analysis [98]) from a total of 42 cells of 3 cell types. The LBN method minimizes errors in identifying Lévy flight behavior, as simple non-normalized frequency linear binning can give erroneous results wrongly identifying Brownian RWs as LWs [90, 93]. As expected from the results from survival distributions, we do not see the signature power-law linear relationship on log-log scale for both flights (Fig. 4.4) and net flights (Fig. 4.5). An exponential distribution fitted to the λ (obtained from survival distributions in Figs. 4.3a and b), is indicated by the bold, black curve in Figs. 4.4 and 4.5. One can see that the experimental data (filled circles) clearly fit the exponential distribution much better than a LW model. We also used likelihood estimates and Akaike weights [91, 92] to determine which of the two models (exponential or power law) fit our experimental data (Table 4.3). The exponential model was favored having higher Akaike weights.

The BCRW model for the epithelial cells differs from a simple CRW such as the often-used PRW model for mammalian cell migration. The PRW model equation (see

methods) is based on a velocity-jump process with instantaneous relaxation period [40] which would be true for bacterial migration. Instead in the BCRW, the re-orientation phase acts as a relaxation period with finite time and has a correlation much smaller than that present in the directional phase. The re-orientation phase is not completely diffusive and the angle changes during this phase are non-uniform. A cell is not stationary during the re-orientation phase and the total distance traveled during this phase is similar to that traveled during directional phase (Table 4.2). But the net displacement (Table 4.1) is higher in the directional phase compared to the re-orientation phase giving rise to higher directionality ratio in this phase [98]. We performed a simulation based on the proposed BCRW to predict the diffusive properties of such a RW and compare with the experimental cellular tracks and also a simple CRW using the PRW model-fit of the experimental data.

By comparison to the PRW model, the BCRW model can pinpoint the factor controlling the directional persistence, either the mean flight lengths ($1/\lambda_{mean}$) or correlations in the turn angle distribution [77]. The migratory differences in the cell types may exist in differences in the correlations within the different flight types and between the directional flights. The neuT cell type was found to be more persistent and pBabe less [98]. The angle change distributions within the directional and re-orientation flights (Fig. 4.6) for the three cell types confirm a high degree of correlation within directional flights. As the three cell types have similar value of the exponent λ, for both the flight types and similar within-flight turn angle distribution; it is the turn angle distribution between the directional flights that seems to control the persistence behavior in a cell type.

The 2-hour experimental MSD plot of these cells has a slope greater than 1 indicating prolonged super-diffusive motion (Fig. 2.15 in Chapter II and Fig. 12 in reference [98]). This further indicates that the probabilistic migration strategy adopted by the cells has super-diffusive properties that cannot be attributed to a simple CRW. A fit of the experimental MSD with a PRW model gives a persistence time of around 10 minutes by creating an early transition to diffusive regime (Fig. 4.7). We find through simulations parameterized by our experiments (neuN cell type), that the BCRW model has super-diffusive properties around experimental time-scale but converges to normal diffusive regime in long-time limit. A simulated composite bimodal CRW incorporating directional and re-orientation phases through the BCRW framework recreates the experimental MSD trend where super-diffusive behavior is maintained over the observed experimental time-scale. We compared the squared relative difference error (see statistical methods) from the PRW model-fit and our BCRW model fit (see *inset* Fig. 4.7). The BCRW model does a better job in fitting the experimental MSD in the transition regime (10 to 60 minutes) compared to the PRW. We also computed the random motility coefficients of the MCF-10A panel of cell lines from the diffusive regime of the MSD trends. Similar to the results from cellular dynamics simulations (discussed in previous Chapter), we find that the neuT cells have higher random motility coefficient (14.5 $\mu m^2/\min$) compared to the pBabe cells (8.7 $\mu m^2/\min$) along with the neuN cells having a value of 12 $\mu m^2/\min$.

4.5 Conclusions

The search strategy of epithelial cells in random migration conditions is found to be an intermittent search process (ballistic motile regions (directional) followed by less-

persistent search periods (re-orientation)). We find no indication of power law behavior in the flight lengths in these regions for the single cell random migration data. The BCRW model provides a new conceptual framework for improved modeling of epithelial cell migration. Our results show that mammary epithelial cells exhibit a bimodal CRW. The BCRW framework model was found to fit the experimental data better compared to a simple CRW modeled using the PRW model. This model could predict the observed prolonged super-diffusivity in experimental trajectories, and will form the basis for more realistic simulations of mammalian cell motility with no prior assumptions regarding the diffusive properties of these cells.

Table 4.1: Statistical significance to compare between the net distances traveled in the directional (d_d) and re-orientation (d_r) phases using the nonparametric, two-sample Kolmogorov-Smirnov test in MATLAB (kstest2.m). A p-value <0.05 indicates significant difference. A similar analysis was repeated for total distances traveled during the directional flights (t_d) and re-orientation flights (t_r) and is shown in Table 2.

	Cell type		
	pBabe	neuN	neuT
d_d [1,3] (micron)	3.09±1.08	3.3±1.33	3.92±1.9
d_r [2,3] (micron)	2.79±1.22	2.43±0.97	2.85±0.77
p-values (n [4])	0.026 (214)	0.001 (187)	0.0326 (169)

[1] Mean net distance traveled during directional phase

[2] Mean net distance traveled during re-orientation phase

[3] Mean value reported is the mean of mean values for each cell (pBabe (n=15), neuN (n=15), neuT (n=12)) while error bars are standard deviation in the means

[4] Sample size for the two groups, which is the number of directional or re-orientation phases

Table 4.2: Statistical significance to compare between the average total distances traveled in the directional (t_d) and re-orientation (t_r) phases using the nonparametric, two-sample Kolmogorov-Smirnov test in MATLAB (kstest2.m). A p-value <0.05 indicates significant difference.

	Cell type		
	pBabe	neuN	neuT
t_d [1,3] (micron)	3.43±1.24	3.78±1.52	4.37±1.99
t_r [2,3] (micron)	4.62±1.73	5.76±4.07	4.86±1.73
p-values (n[4])	0.158 (214)	0.027 (187)	0.417 (169)

[1] Mean total distance traveled during directional phase

[2] Mean total distance traveled during re-orientation phase

[3] Mean value reported is the mean of mean values for each cell (pBabe (n=15), neuN (n=15), neuT (n=12)) while error bars are standard deviation in the means

[4] Sample size for the two groups, which is the number of directional or re-orientation phases

Table 4.3: Maximum likelihood estimates (MLE) of λ (parameter for exponential model) and μ (parameter for power-law model) using maximum likelihood method and Akaike weights for each model for the flight lengths data of the three cell types. The exponential model is highly favored in all cases as indicated by higher Akaike weights.

Cell type (mode)	MLE for model parameter			Akaike weights	
	λ	μ	n	Power law	Exponential
pBabe (Directional)	0.322	1.5	214	0	1
pBabe (Re-orientation)	0.237	1.468	214	0	1
neuN (Directional)	0.289	1.485	187	0	1
neuN (Re-orientation)	0.198	1.453	187	0	1
neuT (Directional)	0.237	1.455	169	0	1
neuT (Re-orientation)	0.219	1.452	169	0	1

Table 4.4: Statistical analysis for estimating the fitting parameter for exponential distribution (λ) from the survival frequency distributions (regstats.m in MATLAB) with r^2 (correlation coefficient) and p-value associated with the slope using t-test indicated.

Cell type (mode)	Flights				Net flights			
	Slope (-λ)	r^2	p value	n	Slope (-λ)	r^2	p value	n
pBabe (Directional)	-0.327	0.993	3.37e-13	214	-0.372	0.978	8.13e-09	214
pBabe (Re-orientation)	-0.221	0.980	5.53e-16	214	-0.387	0.996	1.67e-12	214
neuN (Directional)	-0.255	0.984	3.70e-12	187	-0.293	0.979	1.17e-10	187
neuN (Re-orientation)	-0.187	0.989	3.49e-17	187	-0.437	0.991	1.75e-09	187
neuT (Directional)	-0.249	0.996	1.29e-17	169	-0.239	0.990	1.03e-16	169
neuT (Re-orientation)	-0.208	0.997	3.35e-19	169	-0.372	0.956	3.83e-08	169

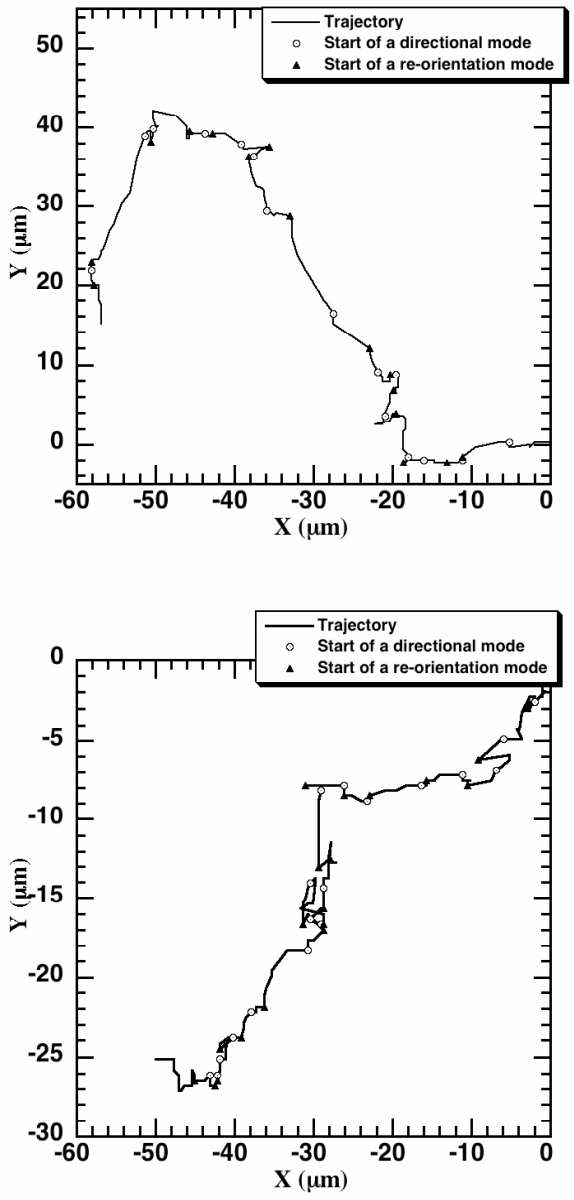

Figure 4.1: Flagging directional and re-orientation flights using bimodal analysis [98].An experimental 2-hour neuT (*top*) and pBabe (*bottom*) cell trajectory with the directional and re-orientation flights flagged using bimodal analysis. The cell track starts at origin (0,0) with the start of a directional flight indicated by an open circle and the start of re-orientation denoted by a filled triangle. A directional flight length is the summation of all the consecutive move step-lengths during the directional phase and similarly, a re-orientation flight length is the summation of a series of all the move step-lengths during the re-orientation phase. The net flight length (directional/re-orientation) refers to the net displacement from start to end during the flight.

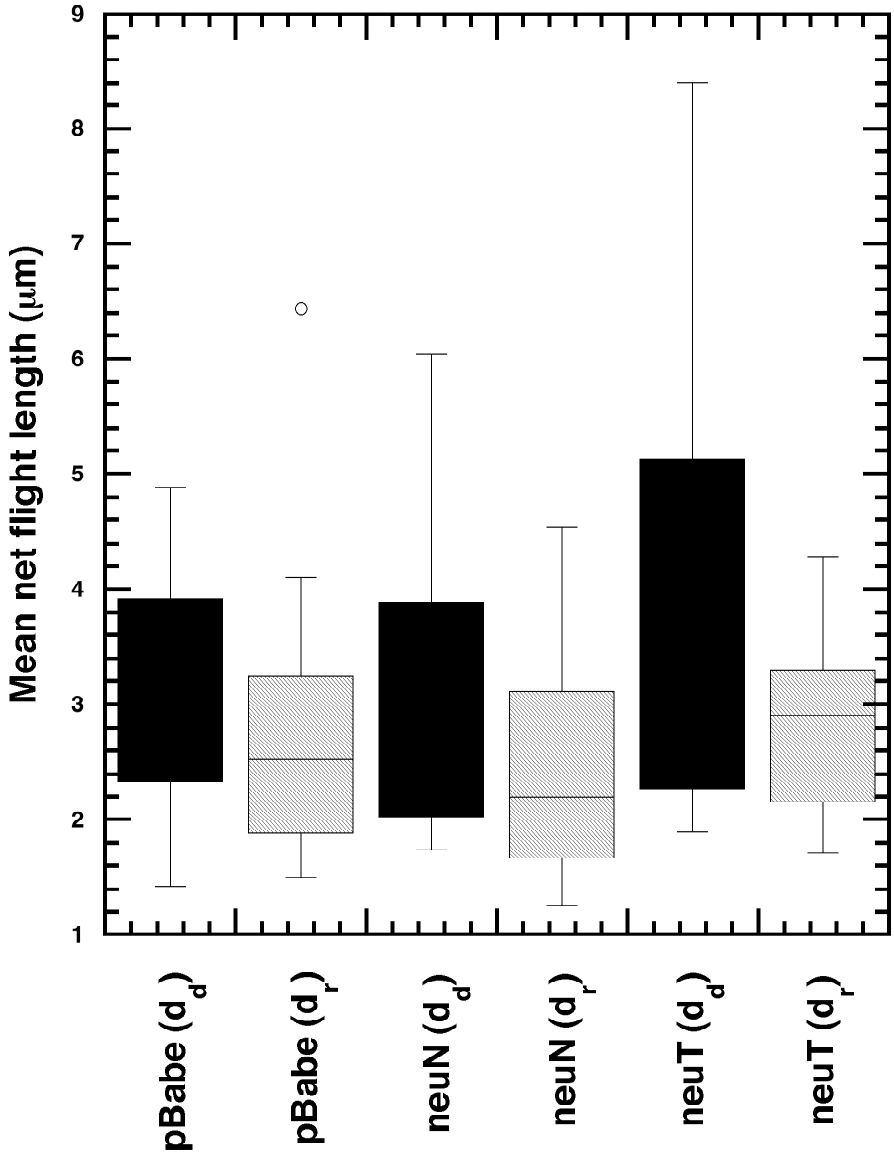

Figure 4.2: Net flight length during the directional and re-orientation phases for the three cell types. Box plots of the mean net flight lengths during the directional (d_d) and re-orientation (d_r) phases for the three cell types (pBabe (n=15), neuN (n=15), neuT (n=12)). The distance traversed in directional flights is more than during re-orientation flights (statistical analysis in Table 4.1).

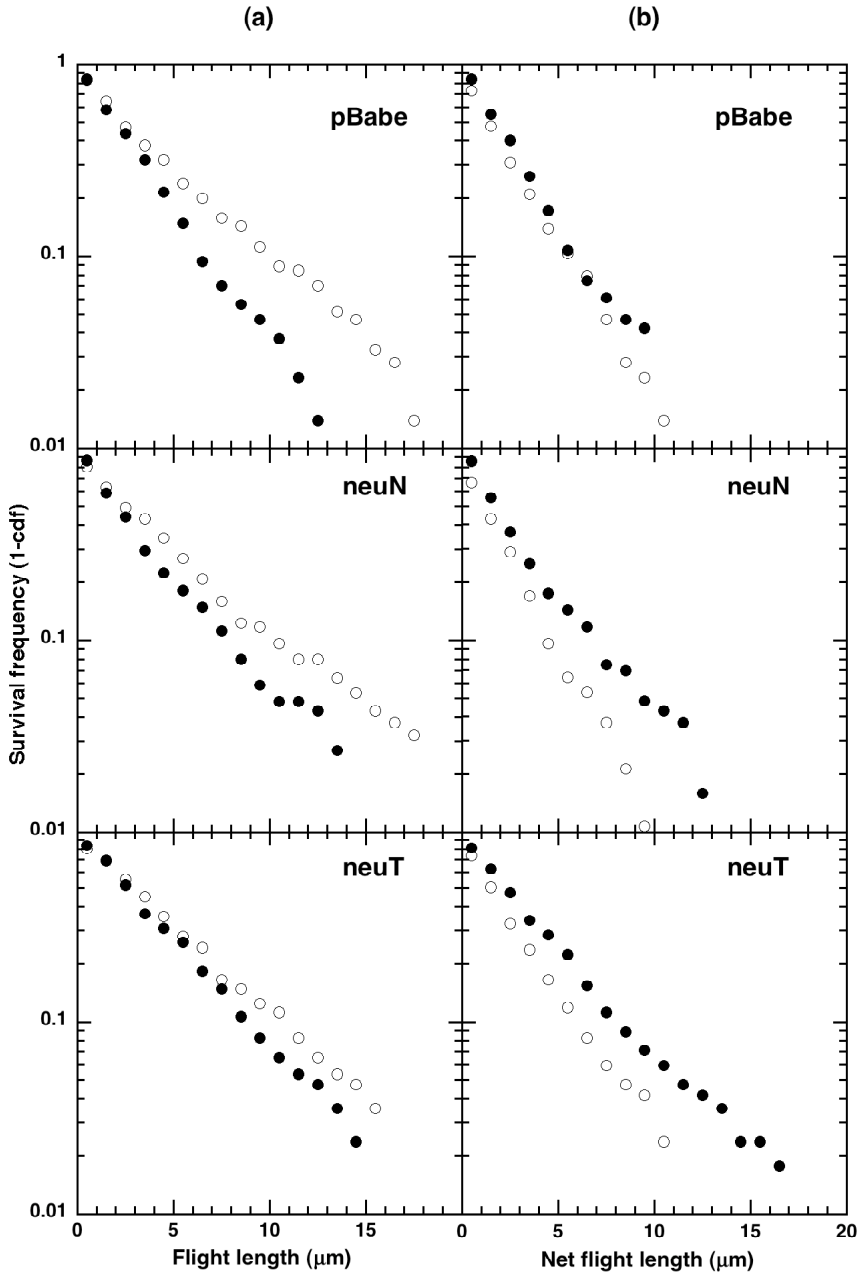

Figure 4.3: Survival frequency (log-linear) plots for the three cell types in different modes. 4.3a (*left* panel), the flight length survival frequency plots, filled circles (directional mode) and open circles (re-orientation mode). 4.3b (*right* panel), the net flight length survival frequency plots, filled circles (directional mode) and open circles (re-orientation mode). The straight-line behavior on the log-linear plots (survival frequency on log scale versus the lengths (flight/net flight) on linear scale) is indicative of exponential distribution of the lengths. The slopes ($-\lambda$ for exponential distribution) along with statistical analysis are shown in Table 4.4.

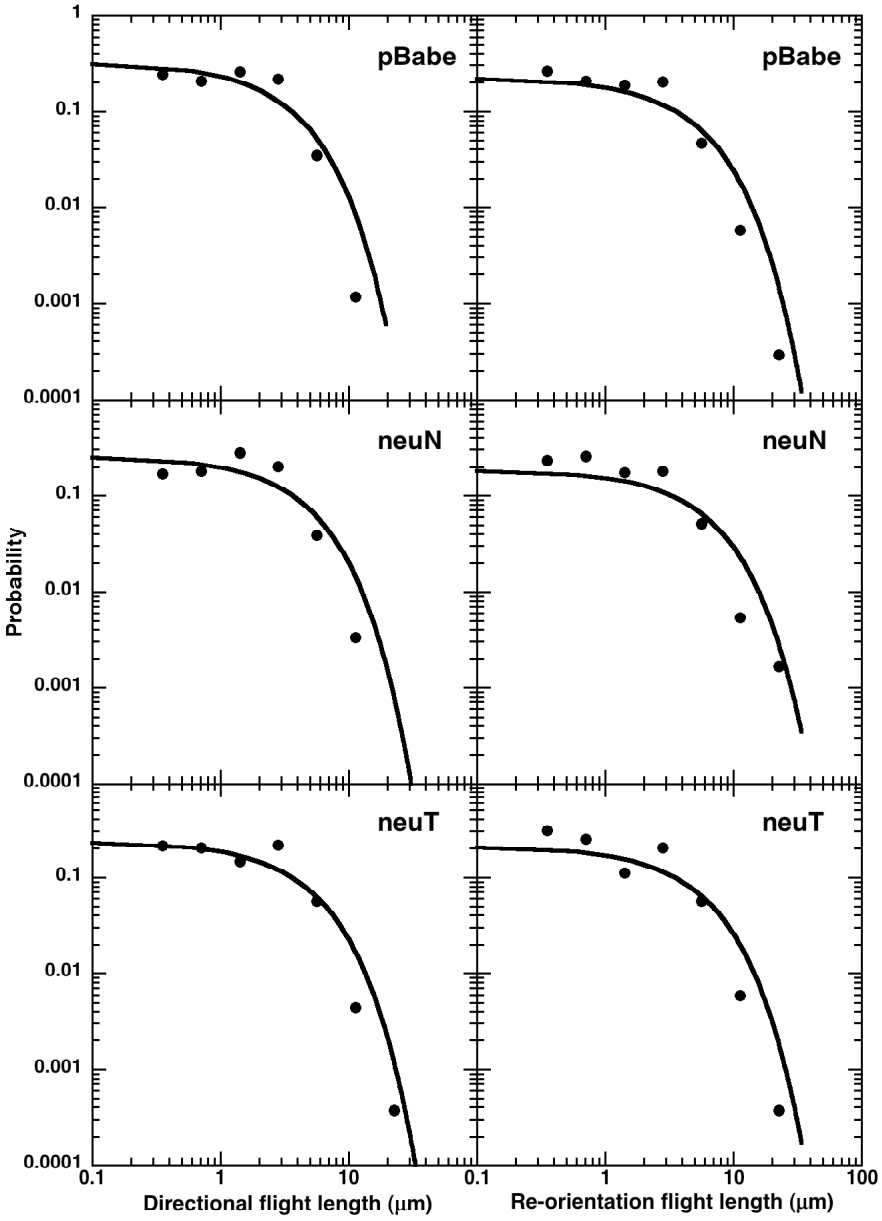

Figure 4.4: Log-log frequency plots using the logarithmic binning with normalization method along with a fitted exponential function. The logarithmically binned flight length distributions on log-log scale for the three cell types. The directional flight lengths are shown in the left panel while re-orientation flight lengths are on the right. An exponential distribution fitted to the λ (obtained from corresponding survival distribution) is shown in bold curve in black. The fitted exponential distribution is in good agreement with the experimental data points.

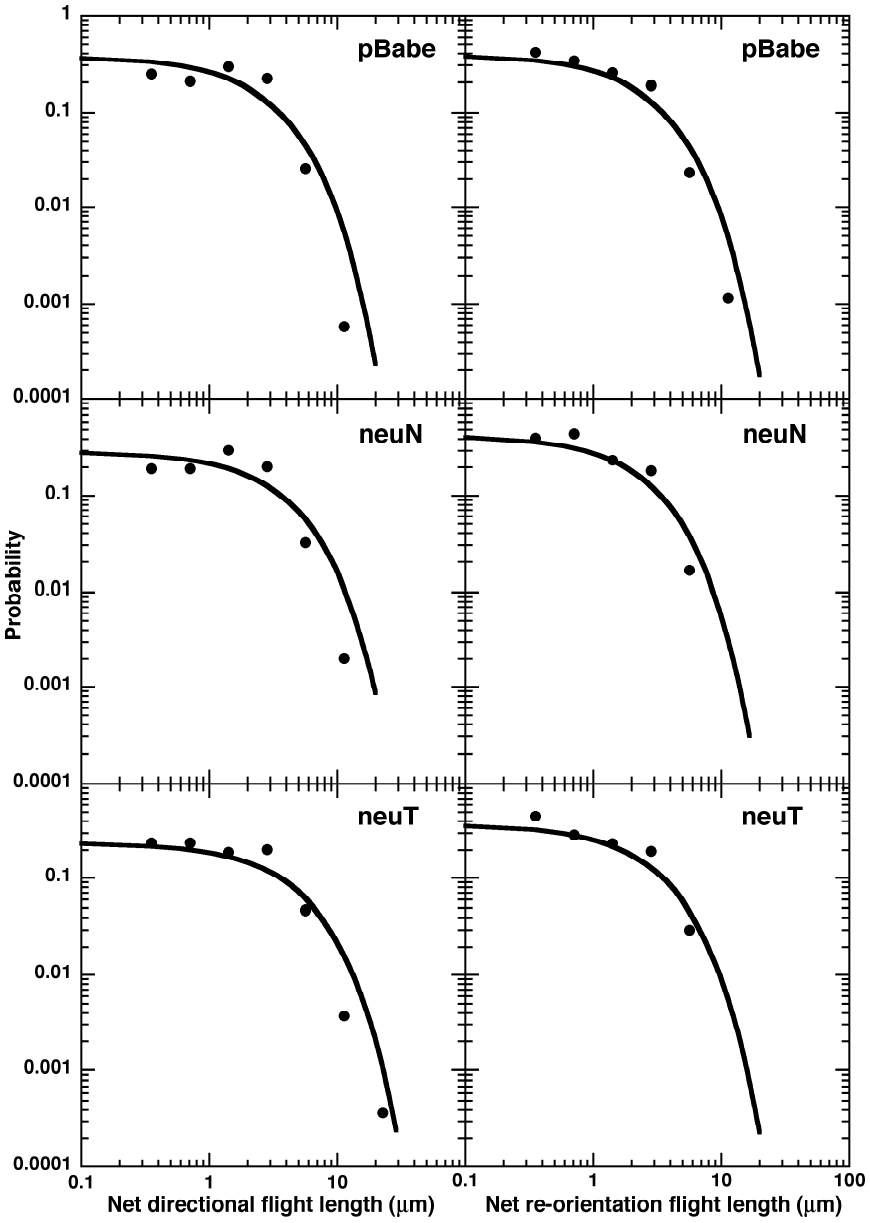

Figure 4.5: Log-log frequency plots using the logarithmic binning with normalization method along with a fitted exponential function. The logarithmically binned net flight length distributions on log-log scale for the three cell types. Directional net flights lengths are shown in the *left* panel while re-orientation net flight lengths are on the *right*. An exponential distribution fitted to the λ (obtained from corresponding survival distribution) is shown in bold curve in black. The fitted exponential distribution is in good agreement with the experimental data points.

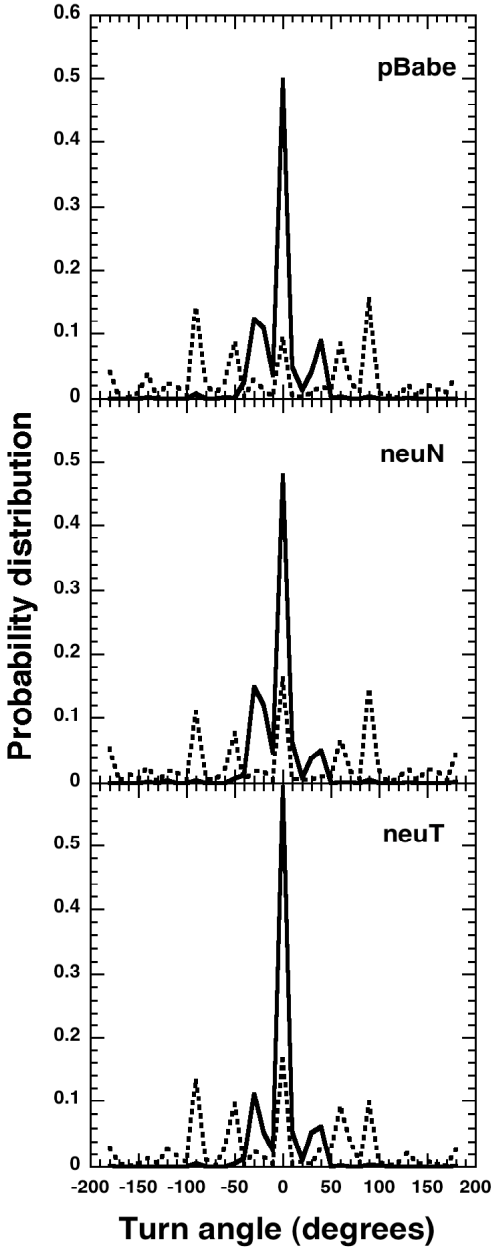

Figure 4.6: Probability distributions of the turn angles within the directional and re-orientation flights. *Top*, pBabe, *middle*, neuN and *bottom*, neuT cells. The solid line shows the turn angle distribution during directional flights while the broken lines during re-orientation flight. The directional flights display higher persistence compared to the re-orientation flights that have a more flatter turn angle distribution.

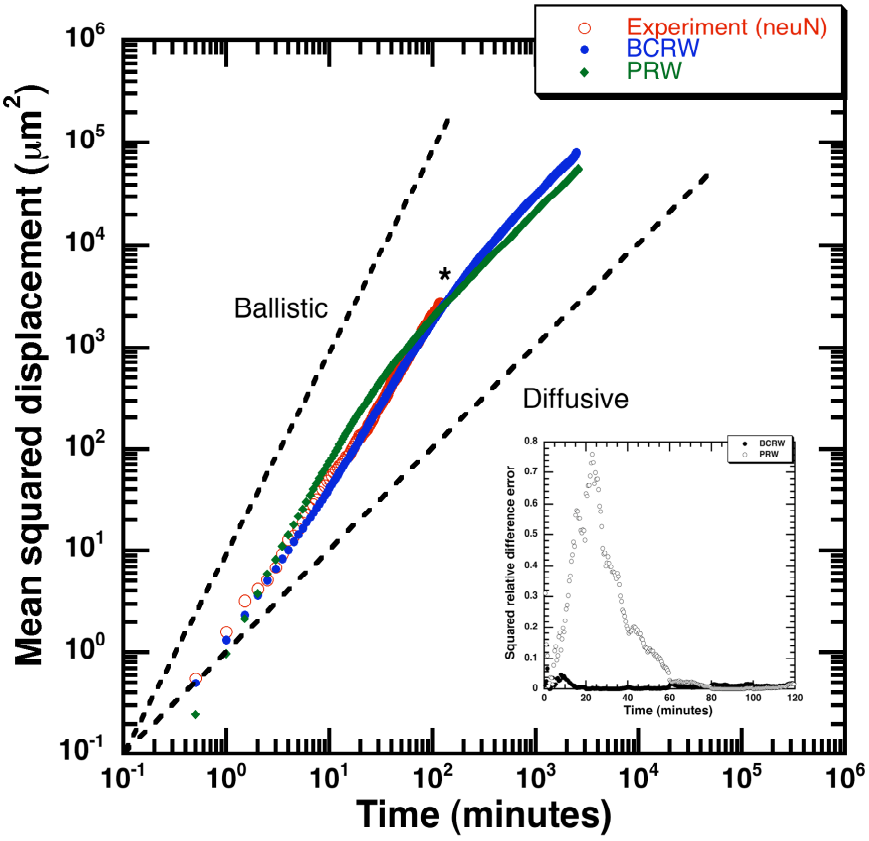

Figure 4.7: Super-diffusive behavior in mean squared displacement trends. Simulated mean squared displacement versus time from a simulation based on BCRW model (blue) compared to the experimental neuN data (red). The bimodal correlation contributes to prolonged super-diffusivity (high persistence) observed in epithelial cells under consideration (neuN cell type). The "*" indicates transition to the diffusive regime in the BCRW model. A fit of the experimental data using a PRW model (green) has been overlaid. *Inset:* Comparison of BCRW and PRW model predictions with the experimental mean squared displacement. The squared relative difference error (difference normalized using the experimental mean squared displacement at a given time) for predictions from BCRW and PRW model. The BCRW model predictions are in good agreement with the experiments.

CHAPTER V

A GENERAL SCALING LAW GOVERNING NON-DIRECTED AND CHEMOTACTIC CELL MOTILITY

5.1 Abstract

A general scaling law describing the eukaryotic cell motility in eclectic range of cell lines namely, *Dictyostelium,* human mammary epithelial, fibrosarcoma and neutrophils is shown here. We used our bimodal analysis technique to analyze non-directed and chemotactic motility of four different cell lines from two species. A scaling relationship was found between the mean directional mode time and the mean re-orientation mode time for all the different types of cells tested under different experimental conditions and these mean mode times were revealed to be inversely related. The emergence of this general relationship indicates the possibility of unifying the different multi-scale processes giving rise to the entire range of eukaryotic cell motility by a general, cellular-scale framework.

5.2 Background

The importance of eukaryotic cell motility, both in normal physiological functions such as embryogenesis as well as pathological conditions, was illustrated in the introductory Chapter I. It was discussed how, in spite of obvious cell-level differences amongst motile eukaryotic cells reflected in cell morphology, persistence, and cell speed, several similarities exist in sub-cellular processes giving rise to motility. At the sub-cellular

level, cell motility is initiated by F-actin based protrusions resulting in structures such as pseudopodia or lamellipodia in cells. Even at the cellular level, all the different types of cells share similarities. They might be moving in fairly straight persistent paths for sometimes followed by moving in random fashion at other times. This behavior of persistent motion interspersed with cellular turns prompted us to develop the bimodal analysis methodology described in detail in Chapter II. We also know that cells continue to be motile with or without the presence of any external gradients and the directional and re-orientation modes exist in both non-directed (random migration, absence of any external gradient) and during directed (chemotactic, presence of external gradients) migration. Hence, there is a possibility of the existence of a unifying principle explaining this diversity in eukaryotic cell motility leading to the conservation of directional persistence and re-orientations in different cell types. The two forms of motility (non-directed[49] and chemotaxis [55]) have been often studied separately; however, we use bimodal analysis in this work to provide a common framework to study different forms of motility simultaneously and determine some shared parameters that modulate the emergent form of motility. Unlike the persistent random walk model (PRW), in bimodal analysis the directional and re-orientation modes are defined as separate processes and the time spent in these modes can be estimated individually.

In order to arrive at any conserved principle describing the full range of *Dictyostelium* motility patterns in different stages, the data from non-directed (so called 'vegetative' and 'developed' states, see methods) and chemotactic motility (in pipette and microfluidic systems) of *wt* (wild type) cells migrating on untreated glass surfaces was analyzed using bimodal analysis. Additionally, we also applied bimodal analysis to 17

different experimental conditions for *Dictyostelium* comprising of either a genetic mutant (cells lacking a signal transduction molecule considered to be important for chemotaxis) or an established regulator of cellular cytoskeleton (see Table 5.1). To compare between different cell types from a different species, we further compared the *Dictyostelium* results from bimodal analysis to that of human mammary epithelial cells, neutrophils and fibrosarcoma cells. The work presented in this Chapter was a collaborative effort with Scott Gruver (Chung lab, Department of Pharmacology). All the *Dictyostelium* data presented here came from Chung lab (Department of Pharmacology). The mammary epithelial data is the same as that described previously in Chapter II. The fibrosarcoma data was collected in Webb lab (Department of Biological Sciences). The neutrophils were a kind gift from Richmond lab (Department of Cancer Biology). The author performed all the bimodal analysis.

5.3 Materials and methods

5.3.1 Cell culture

HL5 medium supplemented with glucose and antibiotics was used to culture *Dictyostelium* cells, axenically. Cells grown on Petri dishes were resuspended and grown in suspension culture for all the assays with these cells. Particularly, for 'vegetative' non-directed motility, cells in an overnight suspension culture were transferred to microfluidic channels or glass bottom dishes for further time-lapse imaging. For developed non-directed and directed assays, cells were cultured in suspension for three days. 1.5 x 10^8 cells were washed three times and re-suspended in 30mL of Na/K phosphate buffer. cAMP (cyclic adenosine monophosphate) (either 12.5 nM or 125 nM)

was then delivered to the cells every 6 minutes for 5 hours . Mutant *Dictyostelium* cells were obtained from the *Dictyostelium* stock center and are listed in Table 5.1. The culture of MCF-10A (mammary epithelial) cells and HL-60 (neutrophils) cells is described in Chapter II or [98] and [103], respectively. HT-1080 (fibrosarcoma) cells were cultured in Dulbecco's Modified Eagle's Medium supplemented with 10% FBS.

5.3.2 Cell motility assays and cell tracking

The imaging of *Dictyostelium* cells and the details of the pipette and microfluidic assays are described in the work by Gruver et al., in [104]. All the assays in the microfluidic device used the same flow rate as in [104]. Except for $g\alpha 2^-$ and aca^- mutants (allowed to develop for longer periods), for all *wt* cells and all other mutants, developed non-directed and micropipette assays were performed after five hours of pulsing with cAMP. All time-lapse images for *Dictyostelium* were obtained every three seconds using 20x DIC optics and MetaMorph. The cell displacements were obtained using the "track objects" function in MetaMorph. Cells were tracked for a minimum of 10 minutes but were often tracked for up to one hour. Blebbistatin (BLEBB) was used at a concentration of 6μM and nocodazole (NOCO) at a concentration of 15μM.

For neutrophils (HL-60) substrates were pre-treated with 100μg/mL fibronectin for one hour. All experiments used 20x DIC optics and were imaged every 5 seconds for at least 20 minutes. Cell centroids were tracked with MetaMorph "track objects" function. The motility assays for MCF-10A cells has been previously described in Chapter II and [98]. Briefly, cells were imaged every 0.5 minutes using 40x phase contrast optics and cells were manually tracked using "track points" MetaMorph option. Fibrosarcoma cells (HT-1080) in suspension were plated on culture dishes pre-treated

with 2.5μg/mL fibronectin. Images were obtained using a 10x phase contrast objective every 2 minutes. Cell centroids were manually tracked using the "Measure XYZ distance" function in MetaMorph. Cells were tracked for a period of 4 to 6 hours.

5.3.3 Bimodal analysis

Bimodal analysis, which segregates a cell path into alternating persistent and re-orientation modes, is fully described in Chapter II and [98]. Briefly, the first step in isolating directional and re-orientation modes requires the determination of the instantaneous direction change, ϕ, for every time point, t. The values of $\phi(t)$ are then compared to an empirically defined cut-off angle, ϕ_{cut}, with time points with values of $\phi(t) < \phi_{cut}$ comprising directional mode. A second criteria was then applied, requiring at least three successive time points with $\phi(t) < \phi_{cut}$ before defining a directional mode. For re-orientation modes, a criteria of $\phi(t) > \phi_{cut}$ for two successive modes was used. In the present work, the value for ϕ_{cut} was set to 45˚. The turn angle, θ, is computed as the angle between two successive directional modes. The overall direction of a directional mode was determined using a multi-point linear regression of all the data points in that particular mode.

5.3.4 Statistical analysis

All statistical analysis was done in MATLAB software package (MathWorks, Natick, MA). The Lilliefors test (lillietest.m) was used to test if the data were parametric or non-parametric. A two-sample Kolmogorov-Smirnov test (kstest2.m in MATLAB) was used to compare between the two cell-types if the data were non-parametric; otherwise the t-test (ttest2.m in MATLAB) was used. A p-value <0.05 indicates significant differences.

Slopes (scaling exponents β) were compared by ANCOVA (function aoctool.m in MATLAB). The comparison *p*-value (shown in Table 5.1, estimated by ANCOVA) was computed by the pair-wise comparisons of slope for each mutant/treatment compared to the estimate for *wt*. These comparisons were done via a two-tailed test and hence at a 5% significance level, values in the range $0.025 < p < 0.975$ were considered significant.

5.4 Results and discussions

A conceptual model of eukaryotic single cell bimodal motility illustrating the switching between the directional and re-orientation modes is shown in Fig. 5.1. The 'polarity tendencies' in the cell could arise due to the different lamellae on the cell circumference for an epithelial cell (pseudopods for a *Dictyostelium*). The directional mode would then correspond to a mode with a prominent leading edge resulting in a highly polarized morphology while in the re-orientation mode, a cell could be speculated to possess several competing polarities leading to a net reduction in resulting polarity.

An example *wt Dictyostelium* cell track (in the absence of any external bias) with the directional and re-orientation modes flagged using bimodal analysis is shown in Fig. 5.2. The beginning of the re-orientation mode is indicated by a red triangle while its end by a green circle. Using bimodal analysis, we estimated the mean mode times (spent in the directional and re-orientation modes) by *wt Dictyostelium* in six different motility assays (vegetative, developed (three different cAMP concentrations), pipette chemotaxis and microfluidic chemotaxis). A plot of mean directional mode time, $\langle t_d \rangle$, of the *wt* cells (n=446) versus the mean re-orientation mode time, $\langle t_r \rangle$, of the cells revealed that the two are inversely correlated as illustrated in Fig. 5.3. This suggests that an increase in the directional mode time is achieved by decreasing the time spent in re-orientation modes,

indicating that the molecular processes governing the two modes are linked. A log-log plot of the data shown in Fig. 5.3 linearizes this non-linear relationship, revealing the scaling relationship shown in Fig. 5.3 inset. As discussed in Chapter II, the criteria for locating directional modes constraints the smallest directional mode time possible to three successive frames. This bias results in a slight non-linearity (Fig. 5.3, inset) for smaller values of $\langle t_d \rangle$ for which corresponding $\langle t_r \rangle$ tends to be overestimated by the analysis. Nonetheless, this inverse scaling relationship evident on the log-log scale enables us to conveniently describe the non-directed to chemotactic *Dictyostelium* motility as well as describing the cell-to-cell variability by means of a common scaling exponent of $\beta \approx -1.11 \pm 0.09$ (estimate ± standard error) (Fig. 5.3, inset). The inverse scaling relationship obtained here is exactly opposite to the positive scaling relationship between search and motion phases (analogous to our re-orientation and directional modes, respectively) reported in animal foraging [105] which is an example of other scaling relationships possible. We compared the mean mode times for non-directed (vegetative and developed assays) to chemotactic (pipette and microfluidic assays) motility of *wt* *Dictyostelium* cells in Fig. 5.4 on a log-log scale and fitted a line with slope given by $\beta \approx -1.11$ (estimated from the entire *wt Dictyostelium* cell population). It can be seen that scaling exponent of $\beta \approx -1.11$ could describe the entire range of *wt* *Dictyostelium* motility in different assays (Fig. 5.4). As the directional persistence in the cells increases going from non-directed to chemotactic motility, the position on the line in Fig. 5.4 slides towards the right, indicating decrease in $\langle t_r \rangle$ for an increase in $\langle t_d \rangle$. This is consistent with previous findings where developed *Dictyostelium* have been reported to move in more coordinated fashion compared to those in vegetative state [106] and also,

that *wt* cells performed efficient chemotaxis in microfluidic chambers compared to that in pipette assay [104].

In Figs. 5.5a, b, and c, we compared the directional mode time, re-orientation mode time and turn angle distributions for the *wt Dictyostelium* cell population in four different assays, namely, vegetative non-directed, developed non-directed, pipette chemotaxis and microfluidic chemotaxis. We find that the directional and re-orientation mode time distributions for the different assays are qualitatively the same and are exponentially distributed indicative of a Poisson process with a constant rate of re-orientation. However, there are quantitative differences between different assays; for directional mode time (Fig. 5.5a), there is an increase in the mean mode time from the non-directed vegetative system to chemotaxis microfluidic system. The trend is reversed for re-orientation mode time (Fig. 5.5b), with a decrease in mean mode time from the non-directed to chemotaxis systems. This suggests that the inherent mechanism that lets the cells switch between the directional and re-orientation modes is same for both non-directed and chemotaxis, the differences being in the quantitative balance between these two modes. A comparison of the turn angle (angle change between successive directional modes) distribution for the *Dictyostelium* cells in different assays reveals that the cells are inherently persistent with all cells having a peak around zero degrees. Nonetheless, the high level of persistence in chemotaxis compared to non-directed motility is reflected in the spread (standard deviation) of the turn angle distributions. It can be seen that the non-directed motility has more broadly dispersed distributions with smaller peaks compared to chemotaxis assays.

In an attempt to study the effect of different mutations or pharmacological treatment on the emergent scaling relationship, we looked into the relationship between the mean mode times for 17 different *Dictyostelium* genetic mutants (cells lacking signal transductions molecules or established cell cytoskeletal regulators) or cells with pharmacological inhibitors in vegetative non-directed, developed non-directed and the pipette chemotaxis assays. We found that all the 17 perturbations retained the scaling relationship between the mean modes times suggesting that the two alternating modes are a robust cellular property. Table 5.1 shows the sample sizes (n) for each perturbation along with the emergent scaling exponent, β ± standard error. A comparison of the β obtained for a particular mutation/treatment value to that of *wt* cells was made using ANCOVA to test for significant difference in the scaling exponent. The associated p-values of such a comparison are indicated in Table 5.1. Out of 17, we could identify only four perturbations ($p>0.975$, namely loss of gsk3, pten or wasp and treatment with blebbistatin) where the scaling exponent was found to be statistically different from the *wt* cells.

We also looked into the existence of similar scaling relationship in the non-directed motility of three other cell types, namely, human mammary epithelial cells expressing two forms of Her-2 oncogene, human neutrophils and human fibrosracoma cells. We found the similar inverse scaling relationship between $\langle t_r \rangle$ and $\langle t_d \rangle$ as found in *Dictyostelium* (Fig. 5.6). The differences in the cell types in terms of the time scales of the molecular processes responsible for producing motility and mean cell speeds is reflected in the different mean mode times obtained. In spite of these differences, all these three cell lines were found to possess a scaling exponent, β, similar to that found

for *Dictyostelium* (ANCOVA was used for statistical comparison and no significant differences were found in the slopes of the three human cell lines). A common scaling exponent of $\beta \approx -0.94 \pm 0.11$was found to describe the four eclectic eukaryotic cell lines; implying a common scaling law of $\langle t_r \rangle \sim \langle t_p \rangle^{-0.94}$ to describe these eukaryotic cells.

5.5 Conclusions

In summary, a general scaling law describing the relationship between directional and re-orientation modes in diverse cell lines and genetic mutations was shown indicating the presence of a common mechanism that regulates persistence in eukaryotic cells. Since the same scaling relationship could describe both non-directed and chemotactic motility, it can be speculated that the two forms of motility evolve from similar molecular processes, chemotaxis being a more specialized form of non-directed motility resulting from the formation of more directional protrusions triggered by chemottractant induced signal transduction.

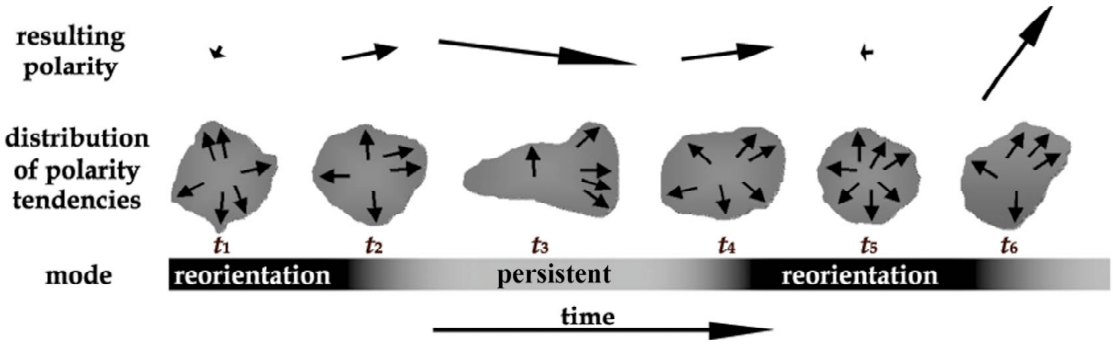

Figure 5.1: A conceptual model for bimodal motility in a eukaryotic cell (*courtesy* Scott Gruver, Department of Pharmacology). This figure illustrates the switching of cell between re-orientation and directional modes with time (t1, t2 and so on).

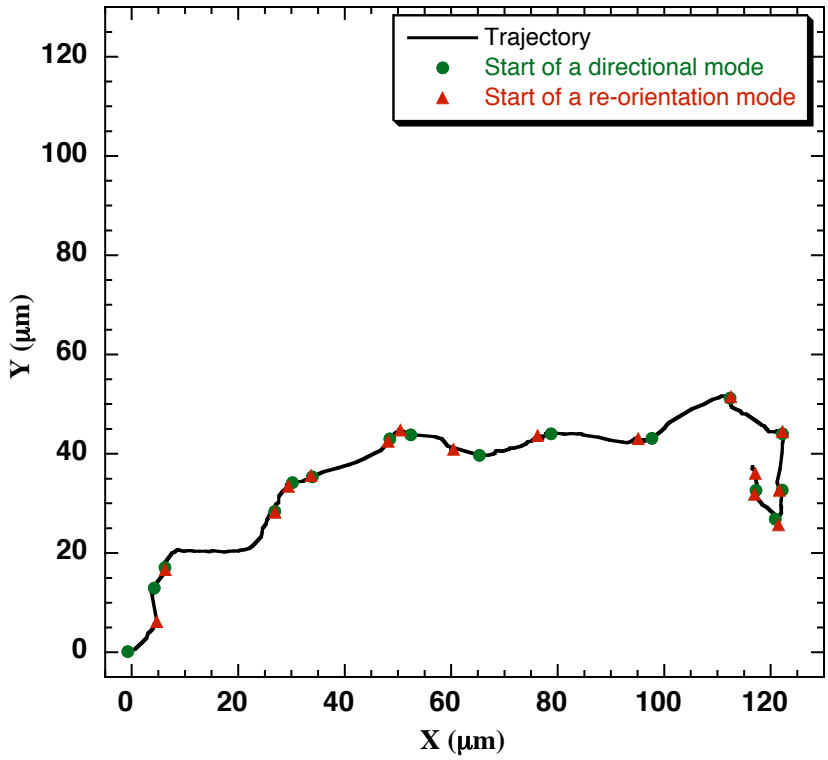

Figure 5.2: Application of bimodal analysis to a *wt Dictyostelium* cell exhibiting non-directed motility, i.e., the absence of any external bias. The circle indicates start of a directional mode and the end of this mode (beginning of re-orientation mode) is indicated by a triangle. The cell was imaged every 3 second.

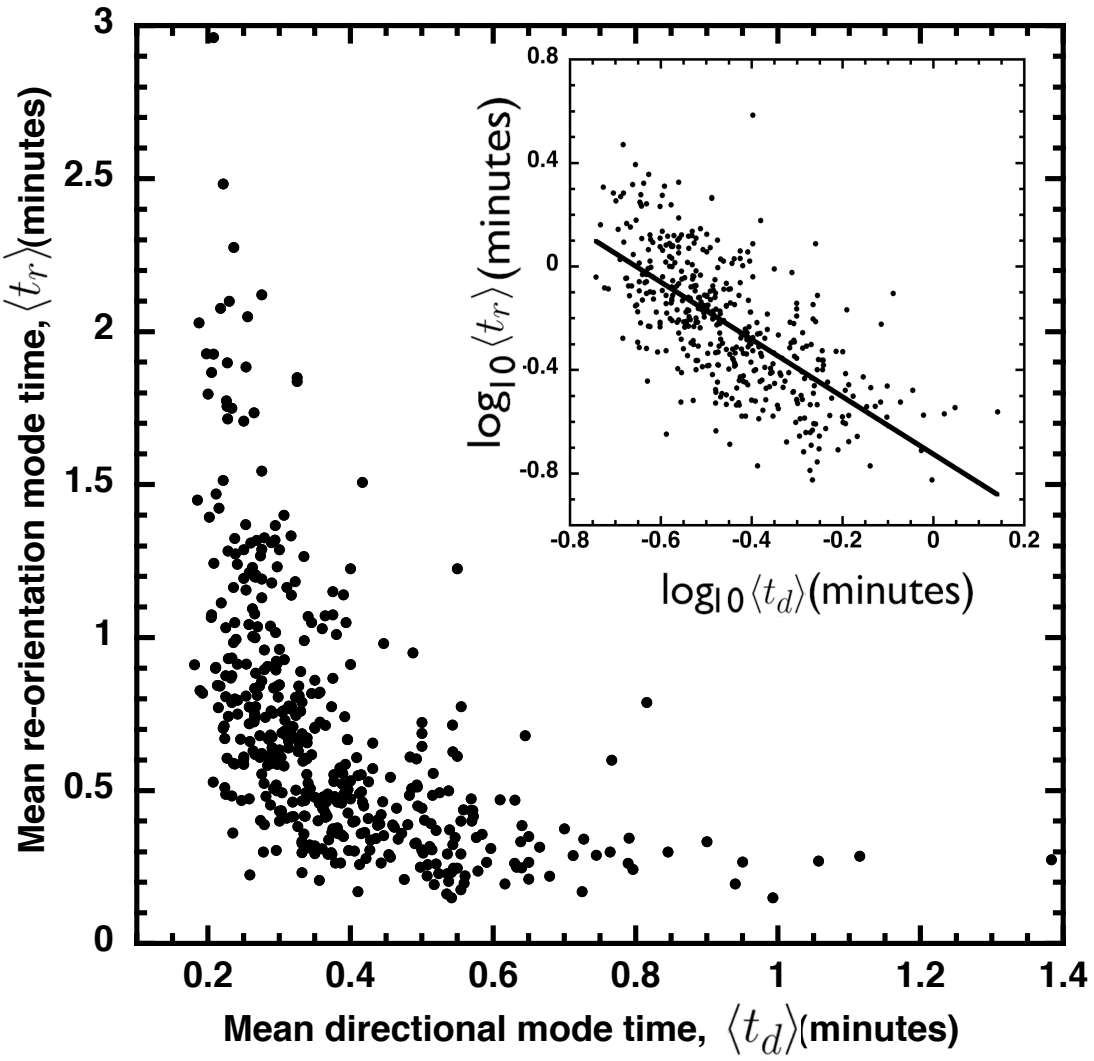

Figure 5.3: The existence of a scaling law between the mean directional mode ($\langle t_d \rangle$) and mean reorientation mode ($\langle t_r \rangle$) times for *wt Dictyostelium* cells tracks from six different motility assays covering the random (non-directed) and chemotactic (directed) *Dictyostelium* cell motility. The non-linear relationship between the mean mode times is represented in the figure while the inset plot linearizes this into a scaling law with an exponent, $\beta \approx -1.11 \pm 0.09$.

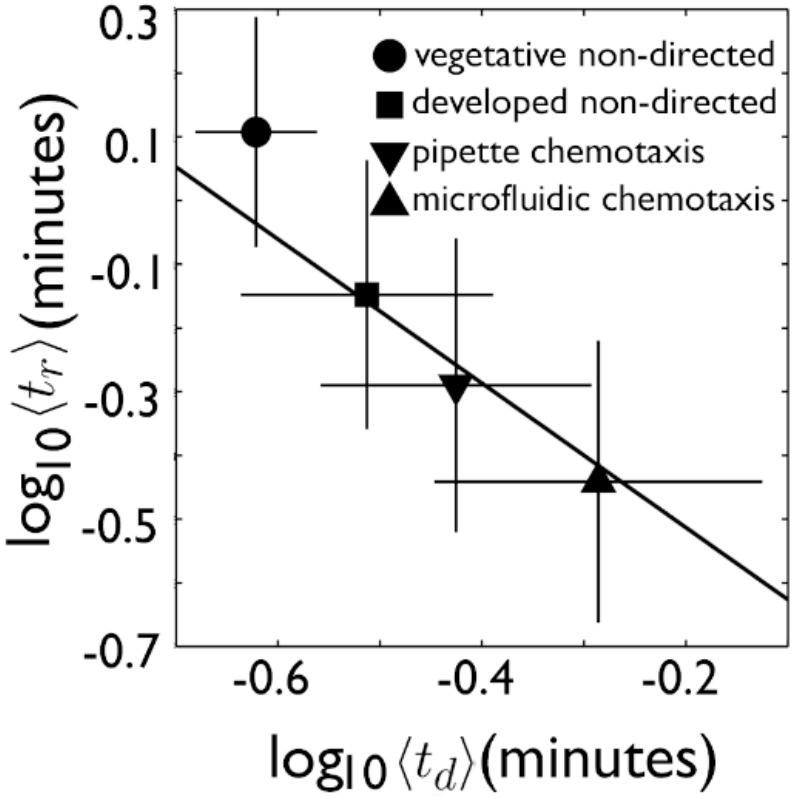

Figure 5.4: The emergent scaling law to describe the entire range of *Dictyostelium* motility, from non-directed to chemotactic cell motility. Each data point represents the average over the entire population in the given motility assay. The scaling exponent derived in Fig. 5.3 (inset) was used to fit the data with a line, shown in black.

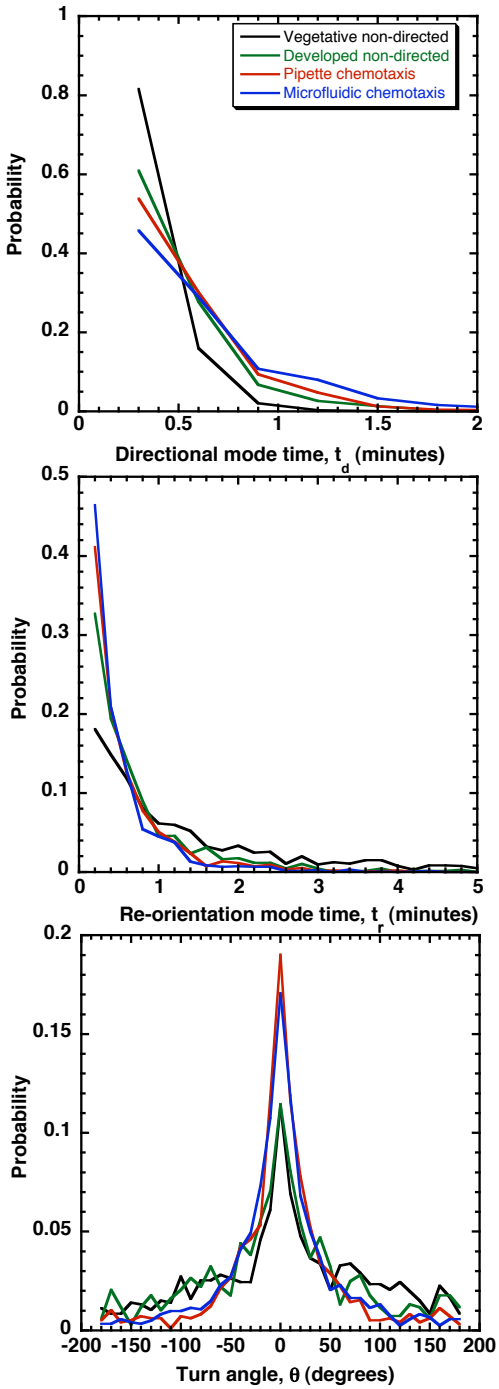

Figure 5.5: The probability distributions of the time spent in directional modes, t_d (top), re-orientation modes, t_r (middle) and turn angle, θ between the directional modes.

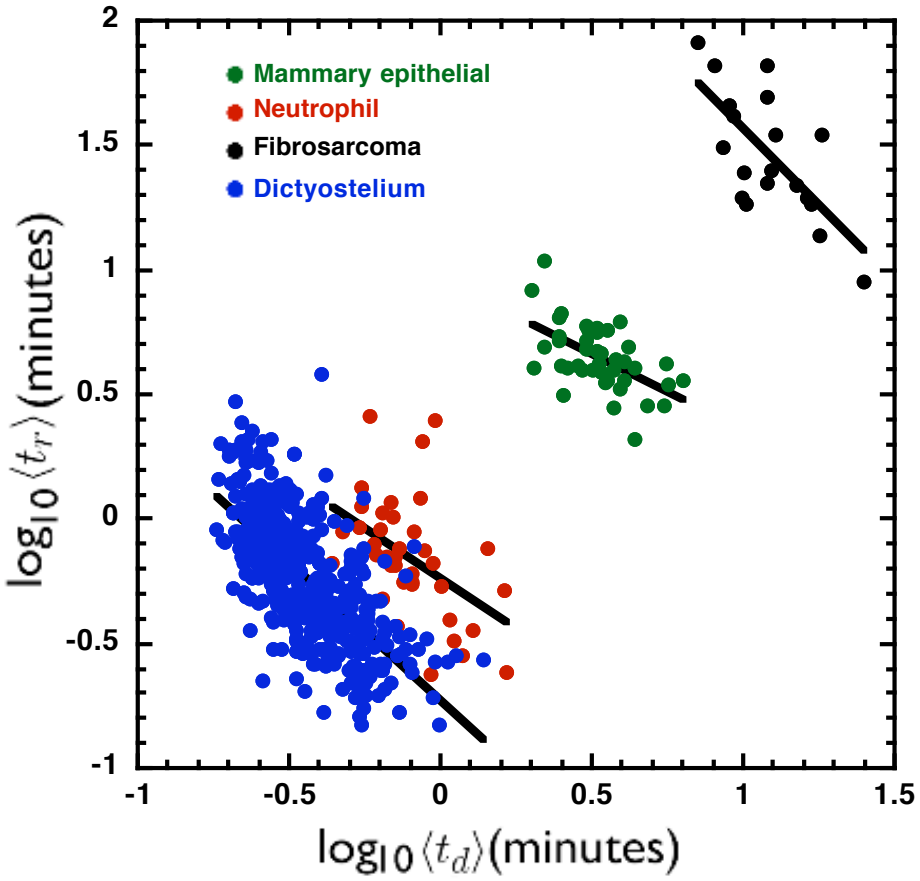

Figure 5.6: A general scaling mechanism (obtained from bimodal analysis) describing the motility of four different cell types, namely, *dictyostelium*, human mammary epithelial, fibrosarcoma and neutrophils. The solid black lines indicate linear fits for each data set. A common scaling equation of $\langle t_r \rangle \sim \langle t_p \rangle^{-0.94}$ was found to describe the motility of these cell lines.

Table 5.1: The scaling exponent, β, for different cell lines (n= cell number) and genetic mutations or pharmacological treatments. The p-values indicate comparison between scaling exponent for *wt Dictyostelium* cells and a perturbation via ANCOVA.

Cell line	***n***	***β***	**s.e.**[1]	***p***
Dictyostelium				
wt	446	-1.11	0.09	-
aca −	40	-1.20	0.40	0.590
erk−	34	-1.25	0.41	0.630
gα2−	39	-1.22	0.39	0.614
gca/sga−	37	-1.65	0.28	0.973
gsk3−	34	-1.80	0.23	0.998
ins6pk−	41	-1.12	0.33	0.515
pi3k1/2−	286	-1.10	0.10	0.483
pka − *cat*−	26	-1.22	0.36	0.618
pldA/C−	16	-1.61	0.37	0.910
pldB−	48	-1.17	0.33	0.580
pten−	249	-1.85	0.12	0.999
wt+BLEBB[2]	38	-1.92	0.36	0.988
wt+NOCO[3]	54	-0.82	0.20	0.067
racC−	54	-0.91	0.17	0.124
scar −	38	-1.31	0.36	0.710
vasp −	60	-1.16	0.24	0.581
$wasp^{TK}$	35	-2.14	0.34	0.999
Human Cells				
Neutrophils (HL-60)	39	-0.82	0.19	NA[4]
Mammary epithelial (MCF-10A)	42	-0.60	0.20	NA
fibrosarcoma (HT-1080)	19	-1.22	0.24	NA

[1] not applicable
[2] standard error in the estimation of scaling exponent β
[3] concentration of 6 μM
[4] concentration of 15 μM

CHAPTER VI

MAMMARY EPITHELIAL CELLS IN TEMPORAL GRADIENTS OF EGF

6.1 Abstract

Single cell migration tracks of human mammary epithelial cells (expressing different versions of promigratory tyrosine kinase receptor Her-2) exposed to a time-increasing concentration of epidermal growth factor (EGF) were analyzed to study the effect of temporal gradients of EGF. The temporal gradient was quantified experimentally (using FITC-dextran of molecular weight similar to EGF) and using simulations. A time-increasing concentration of EGF was found in the vicinity of cells tracked for the experimental time scale under consideration (~6 hours). We found that the EGF stimulation led to a chemo-kinesis effect with an increase in speed for MCF-10A neuN while a decrease for MCF-10A neuT along with no change for the control MCF-10A pBabe. We did not find any significant chemotactic effect due to the temporal EGF gradients suggesting that mammary epithelial cells (in the *vitro* conditions under consideration) may not be using temporal sensing. There was no difference in the mean squared displacement trends of cells in starvation medium (no exogenous EGF or serum addition) and those in temporal gradient of EGF suggesting similar random motility coefficients for both the conditions.

6.2 Background

A cell (prokaryotic or eukaryotic) has the ability to sense the gradient of a chemoattractant and perform directed migration called as chemotaxis. The sensing of this gradient can occur either temporally or spatially. This is illustrated in Fig. 6.1. In spatial sensing (top, Fig. 6.1), the cell senses a chemoattractant gradient spatially across its body by measuring the back and front concentration at a given time, thereby responding to this difference, i.e., the spatial gradient, $\frac{\partial c}{\partial x}$, where; c is the concentration and x is the spatial scale across the cell; more generally, in more than one dimension, the spatial gradient is given by ∇c. In temporal sensing (Fig. 6.1, bottom), the cell keeps track of the concentration of a molecule such as a chemokine or a growth factor at different times and uses the consecutive-time, concentration difference to sense the gradient. In this mechanism, the cell is measuring what it called as substantial derivative of concentration, i.e., $\frac{Dc}{Dt}$, where t is time. The substantial derivative is given by $\frac{Dc}{Dt} = \frac{\partial c}{\partial t} + \vec{v}\nabla c$; where $\vec{v}$ is the mean cellular velocity. Hence, cells that sense $\frac{Dc}{Dt}$, can appear to respond to a spatial gradient when $\vec{v}\nabla c >> \frac{\partial c}{\partial t}$, when in fact they are sensing temporally (i.e., through change in the concentration as they move).

In order to find the sensing mechanism in bacteria, Macnab and Koshland [107] rapidly mixed suspensions of bacterial cells (*Salmonella typhimurium*) and attractants and observed that cells exposed to positive gradients swam without tumbling for 5 minutes and those exposed to negative gradients tumbled continuously for about 12 seconds showing that *Salmonella* bacteria sense temporal gradients. Berg and Brown [108] later

showed that *E. coli* also sense temporal gradients by subjecting *E.coli* to time increasing or decreasing($\frac{\partial c}{\partial t} \neq 0$), spatially homogenous ($\nabla c = 0$), concentration of L-glutamate by the reversible enzymatic action of alanine amino-transferase on L-alanine.

A key finding in bacterial chemotaxis is that the turn angle distribution is unaffected by the presence of a chemoattractant, while the run time distribution is modulated (bacteria extend their run times when moving in directions of increasing chemoattractant concentration) [29], thus resulting in biased movement towards increasing chemoattractant concentration. Moreover, by demonstrating that the same run time increases were induced by a spatially homogeneous but time-varying chemoattractant concentration, Berg [108, 109] showed that *E. coli* were responding to the substantial derivative of the chemoattractant concentration, so that the chemosensing mechanism in bacteria is related to the time rate of change in bound receptors on the cell surface. This rules out the possibility that in *E. coli* the chemosensory mechanism is based on the differences in the number of bound receptors over the cell surface (i.e., a direct sensing of the chemoattractant gradient by spatial comparison). A mathematical analysis of chemosensing by Berg and Purcell [110] shows that despite the small cell size (~ 1 μm) spatial sensing of a chemoattractant gradient is possible for *E. coli*; specifically, taking into account fluctuations in chemoattractant concentration on the spatial scale of a cell, Berg and Purcell derived expressions for the minimum time required for temporal sensing, $T_{\text{sensing}}^{\text{temporal}}$, and for spatial sensing, $T_{\text{sensing}}^{\text{spatial}}$, given by

$$T_{\text{sensing}}^{\text{temporal}} > \frac{1}{2}\left[\pi a D\left(\frac{Ns}{Ns+\pi a}\right)\left(\frac{\bar{c}c_{1/2}}{\bar{c}+c_{1/2}}\right)\left(\frac{1}{\bar{c}}\frac{\partial \bar{c}}{\partial t}\right)^2\right]^{-1/3} \tag{6.1}$$

$$T_{\text{sensing}}^{\text{spatial}} > \left[\frac{1}{2}\pi a^3 D \left(\frac{Ns}{Ns + \pi a} \right) \left(\frac{\bar{c} c_{1/2}}{\bar{c} + c_{1/2}} \right) \left(\frac{1}{\bar{c}} \frac{\partial \bar{c}}{\partial x} \right)^2 \right]^{-1} \tag{6.2}$$

where a is the radius of the cell, D is the self-diffusion coefficient of the chemoattractant, N is the number of receptors on the cell surface, s is the cell-receptor radius, $\bar{c}$ is the equilibrium concentration of the chemoattractant, $c_{1/2}$ is the dissociation constant for the receptor-chemoattractant binding and x is the direction in which the chemoattractant gradient exists. For temporal gradients created by the movement of the cell, $\left(1/\bar{c}\right)\left(\partial \bar{c}/\partial t\right) = \left(v/\bar{c}\right)\left(\partial \bar{c}/\partial x\right)$, where v is the cell speed. For typical values of these parameters for *E. coli* responding to an aspartate gradient, Berg and Purcell found $T_{\text{sensing}}^{\text{temporal}} > 0.4 - 1.4$ s (depending on magnitude of chemoattractant gradient) and for spatial sensing, $T_{\text{sensing}}^{\text{spatial}} > 1.7$ s. Since the run lengths of flagellated bacteria are typically of the order of 1 s and longer, this analysis suggests that a bacterium could use either temporal or spatial sensing; however, because the swimming motion of a bacterium causes the cell body to rotate, the resulting disturbance to the surrounding liquid medium would create fluctuations in the chemoattractant gradient much larger than the gradient itself, thus ruling out the spatial sensing mechanism.

To perform a similar analysis for eukaryotic cells, we use the experimental conditions of Sai *et al*. [111] for the study of chemotaxis of HL-60 cells stably expressing CXCR2 receptor in a microfluidic-device-generated-gradients of CXCL8 chemokine. For these cells in this chemotaxis assay,

$$a = 7.5\mu m, D = 10^{-6} cm^2/s, \bar{c} = 1.25nM, c_{1/2} = 1.5nM,$$
$$(1/\bar{c})(\partial \bar{c}/\partial t) = (\upsilon/\bar{c})(\partial \bar{c}/\partial x) = 2 \times 10^{-4} s^{-1}.$$

Taking $Ns/(Ns+\pi a)=0.5$ (a typical value), and using these values in equations (6.1) and (6.2), we find that $T_{\text{sensing}}^{\text{temporal}} > 1$ min and $T_{\text{sensing}}^{\text{spatial}} > 18$ s. We note that the larger size of these cells (compared to bacteria) results in the time threshold for spatial sensing being less that that for temporal sensing; this is the reverse of the situation for bacteria, in which the time threshold for spatial sensing is greater than that for temporal sensing. From the bimodal analysis of the MCF-10A cells reported in Chapter II, we find that the mean directional-mode time duration of these epithelial cells ranges in several minutes compared to bacterial run times of seconds. Hence both temporal and spatial sensing mechanisms remain feasible for these eukaryotic cells.

It is generally believed that mammalian cells (particularly epithelial cells) that are spatially much larger (~15-20 μm) compared to bacterial cells (1 μm), can sense chemotactic gradients via spatial sensing mechanism and hence they have been subjected to steady (via microfluidic chambers, [112-114]) spatial gradients to observe chemotaxis. However, so far the possibility of temporal sensing in epithelial cells has not been ruled out and to our knowledge not been measured. Metastatic epithelial cells such MDA-MB-231 have been shown to perform chemotaxis towards non-linear spatial gradients of epidermal growth factor (EGF) created via micro-fluidic chambers [112-115]. In this work, we asked the question: "Can mammary epithelial cells sense a temporal gradient of EGF?" We used the same panel of cell lines (as mentioned in Chapter II) expressing the different versions of Her-2 receptor. EGF has been known to promote migration in epithelial cell lines before [116, 117] and hence we chose this molecule as a ligand for our experiments with MCF-10A mammary epithelial cell lines. As mentioned earlier, EGF has been used previously to study chemotaxis in metastatic breast cancer cell line,

MDA-MB-231 cells in microfluidic chambers [112]. In this work, we describe an experimental arrangement to subject MCF-10A cells to time increasing concentration of EGF. We also show that the concentration of EGF in the immediate vicinity of the cells observed is more or less spatially uniform within an hour of starting the EGF injection.

6.3 Materials and methods

6.3.1 Cell culture

The cell lines used in the motility experiments were a kind gift of Dr. Joan Brugge and were derived from the MCF-10A human mammary epithelial cells to express the pBabe vector alone (pBabe), or the normal (neuN) or transforming (neuT) versions of the rat Her-2/Neu oncogene [58, 59]. All the cells were cultured in DMEM/F-12 50/50 media (Mediatech, Herndon, VA) supplemented with horse serum (2%, GIBCO/Invitrogen, Carlsbad, CA), cholera toxin (0.1μg/mL, Calbiochem, La Jolla, CA), insulin (10μg/mL, GIBCO/Invitrogen, Carlsbad, CA), hydrocortisone (0.5μg/mL, Sigma, St. Louis, MO) and EGF (20ng/mL, GIBCO/Invitrogen, Carlsbad, CA) as described by protocol in work by Debnath and coworkers [60]. The cells were maintained in a humidified atmosphere supplemented with 5% CO_2 and were split every 3 to 4 days.

6.3.2 Cell motility assay

The migration of cells was followed under different conditions: with and without the presence of any externally injected EGF (Invitrogen, Carlsbad, CA) at 50 ng/ml using a Harvard apparatus pump 11 pico plus syringe pump (Harvard Apparatus, Holliston, MA) at a flow rate of 0.1 $\mu l/\text{min}$. All the three cell types (MCF-10A pBabe, neuN and neuT) were plated overnight at a low density of 10,000 cells on 60 mm tissue culture dishes in

full growth medium to avoid interacting cell populations. The cells were thoroughly washed with starvation medium (SM, which is defined as the full growth medium minus horse serum and EGF) and the media replaced with SM, a couple of hours before the start of the experiment.

The cells were monitored using the phase-contrast optics in a Zeiss Axiovert 200M inverted microscope with a monochrome, cooled CCD camera (CoolSNAP HQ, Roper Scientific, Trenton, NJ) equipped with temperature-controlled, humidified chamber. Cellular images were captured using MetaMorph (Molecular Devices Corporation, Sunnyvale, CA) for data acquisition and analysis. The time-lapse images were collected at a magnification of 10x (1 pixel $\equiv 0.98\ \mu m$) and using a sampling time interval of 0.5 minute. All the cells were equilibrated in the humidified, temperature controlled (37 ^{0}C) microscope chamber for half an hour before data collection. In all experiments, the cells were followed for at least seven hours and the cells at the center of the dish were monitored. The control consisted of following the cells for the first two hours with SM continuously injected at 0.1 $\mu l/\min$. This was followed by monitoring cells with continuous injection of EGF containing medium (SM + 50 ng/ml of EGF) for at least 5 hours.

6.3.3 Temporal gradient experimental setup

The experimental setup to create a temporal gradient for epithelial cells is illustrated in Fig. 6.2. The cells were plated on a 60 mm cell culture dish overnight, media changed to SM and transferred to the humidified chamber of the CO_2 microscope. A slot was made at the corner of the tissue culture dish lid to house the tubing connected to a syringe filled with appropriate medium on a Harvard pump. Since the diffusion coefficient of EGF

molecule ($10^{-7} cm^2/\text{sec}$) is much greater than the random motility of the cells ($10^{-9} cm^2/\text{sec}$), it can be expected that there is not much spatial inhomogeneity in the immediate vicinity of the cells observed (at the center of the dish), so that $\frac{Dc}{Dt} \approx \frac{\partial c}{\partial t}$.

6.3.2.1 Gradient quantification via experiment

We quantified the EGF (Mol. Wt: 6.6 kDa) concentration profile across the tissue culture dish using a dummy molecule, FITC-dextran (Mol. Wt. 10kDa, Sigma Aldrich, St. Louis, MO). The same experimental setup as shown in Fig. 6.2 was used but without any cells and FITC-dextran was used instead of EGF. A stock solution of 0.1 mg/ml was used to make a standard curve. Sample triplicates in a 96-well plate were used to measure the FITC fluorescence (excitation 488 nm, emission 530 nm) using a Perkin-Elmer 96-well, Wallac1420 plate reader. Samples were taken every 30 minutes for at least 3 hours from two positions (Fig. 6.3) on the cell culture dish, namely, the cell monitoring position (center, *c*) and a position at the top (*t*), in the vicinity of the center. The concentration of FITC-dextran measured with increasing time is shown in Fig. 6.3 and we can see that the gradient is not very different in the two positions and the concentration is increasing with time. It can be seen from Fig. 6.3 that $\frac{\partial c}{\partial t} \approx 60 \frac{ng}{ml.hr}$ and referring to the top view of the dish shown in Fig. 6.3, $\frac{\partial c}{\partial x}$, between points *c* and *t* after 3 hours, can be calculated as follows:

$$\frac{\partial c}{\partial x} \approx \frac{c_t - c_c}{x_t - x_c} \approx \frac{10 ng/ml}{20 mm} \approx 0.5 \times 10^{-3} \frac{ng}{ml.\mu m}$$

$$v \approx 60\mu m/hr \;;\; v\nabla c = 0.03\frac{ng}{ml.hr} \;;\; v\nabla c \Big/ \frac{\partial c}{\partial t} \approx 0.0005$$

Therefore, the spatial inhomogenity in the vicinity of the cells tracked is negligible and a time varying concentration of EGF is formed.

6.3.2.1 Gradient quantification via simulation

The gradient profile was simulated using 'pdepe' funtion in MATALB (MathWorks, Natick, MA). There is symmetry in radial direction, (1-D problem) with a source term present as EGF is being added continuously at a fixed molar flow rate.

The parabolic partial differential equation to be solved in rectangular coordinates is:

$$\frac{\partial c}{\partial t} = D\frac{\partial^2 c}{\partial x^2} + S \tag{6.3}$$

where, c is the concentration of EGF, x is the length scale and S is the source term. The dish has 3 ml of initial volume. S is the molar flow rate of EGF that is given by,

S=Pump speed (v_{pump}) ($ml/\min$)*source concentration (S_c) pg/ml

$$S = 0.0001ml/\min \times 16666pg/ml = 1.66pg/\min$$

Non-dimensionalization:

$\bar{c} = c/(0.01 * S_c)$

$\bar{x} = x/L$, where L is the diameter of the cell culture dish (6 cm)

$\bar{t} = t/\tau$, where τ is the simulation time step, which is 1 min.

Equation (6.3) can be re-written as:

$$\frac{\partial \bar{c}}{\partial \bar{t}} = (D * \tau / L^2)\frac{\partial^2 \bar{c}}{\partial \bar{x}^2} + v_{pump} * \tau \tag{6.4}$$

Equation (6.4) was solved using the partial differential solver 'pdepe', in MATLAB using following initial and boundary conditions:

I.C.: $\bar{c}(\bar{x}, t = 0) = 2 * heaviside(\bar{x} - 1)$,

where 'heaviside' function in MATLAB was used so that for any variable x, heaviside(x) has the value 0 for x < 0, 1 for x > 0, and 0.5 for x = 0.

B.C: $\frac{\partial \bar{c}}{\partial \bar{x}}(\bar{x}_{=0,1}, t) = 0$

The concentration profiles after 1 min, 1 hour, 3 hour and 6 hours are shown in Figs. 6.4 a, b, c and d respectively, (concentration $\equiv \bar{c}$ and distance $\equiv \bar{x}$, time $\equiv \bar{t}$). We can see that the concentration at the center of the dish ($\bar{x} = 0.5$) increases with time as we move from Figs 6.4 a, b, c to d. This is consistent with experimentally measured time increasing concentration of FITC-dextran as shown in Fig. 6.3.

6.3.4 Cell tracking

Each cell was tracked by following the cell nucleus using the "track points" function in MetaMorph (i.e., the manual tracking option). Only single cells were considered for the analysis. Cells that remained stationary, or moved outside the viewing area, underwent cell division during the course of the experiment, did not migrate over a distance of at least 2 cell bodies (<30 μm) or that adhered to other cells were excluded from the tracking procedure. Applying this criterion, ~60% of the cells were retained.

6.3.5 Bimodal analysis

Bimodal analysis (which segregates a cell track into alternating directional and reorientation modes) is described in detail elsewhere (see Chapter II and ref. [98]). Briefly, the directional and re-orientation modes were flagged by first computing instantaneous direction change (ϕ) at each frame (time point) and then applying a cut-off (ϕ_{cut}) to flag the modes. A cut-off value of ϕ_{cut} = 45° and 'r3 criterion' (ϕ value at three

successive frames determines a directional mode) was used for all the data analysis. The choice of $\phi_{cut} = 45°$ (cut-off value) is heuristic in nature and is discussed elsewhere [98]. This cut-off value best succeeded in flagging the re-orientation mode for the different cell types under consideration. The turn angle, θ (the angle change between successive directional modes) was computed using multi-point linear regression of all the data points constituting a directional mode. The details of all the rules used to locate the modes can be found in ref. [98] and Chapter II.

6.3.6 Statistical Analysis

All statistical analysis was done in MATLAB software package (MathWorks, Natick, MA). The Lilliefors test (lillietest.m) was used to test if the data were parametric or non-parametric. A two-sample Kolmogorov-Smirnov test (kstest2.m in MATLAB) was used to compare between the two cell-types if the data were non-parametric; otherwise the t-test (ttest2.m in MATLAB) was used. A p-value <0.05 indicates significant differences.

6.4 Results and discussions

Wind rose plots of some of the cells selected for analysis is shown in Fig. 6.5. A few trajectories for pBabe and neuT cells (5 each) are illustrated. The left panel shows the control tracks in the presence of SM while the right panel shows trajectories with EGF stimulations. All the cell tracks shown here correspond to experimental time of 2 hours. We can see that under both conditions (with and without temporal EGF gradient), both the cell types display the same degree of persistence behavior qualitatively. As expected and reported in Chapter II, we do see that the neuT cells are more persistent compared to pBabes. We further looked at the effect on the mean cell speed for the three cell types.

The mean cell speeds represented in the form of a box plot are shown in Fig. 6.6. The light shaded columns represents the control while filled column indicates cells in 4 to 5 hours of EGF temporal gradient. Applying a two-sample Kolmogorov-Smirnov test at 5% significance level, we found that there was no significant difference in the mean cell speed for pBabe cells in both control and EGF treatment (p=0.1224, n=10 (control) and n=13 (EGF)). However, for neuT cell type, there was a slight decrease in the mean cell speed with the exposure to EGF temporal gradient (p=0.0283, n=21 (control) and n=29 (EGF)). Conversely, for neuN cell type, there was an increase in the mean cell speed with EGF stimulation (p=0.0083, n=32 (control) and n=25 (EGF)). Hence, we find that the temporal gradient of EGF has a chemokinetic effect in the two different versions of Her-2 cell lines (namely, neuN and neuT). But, no chemotactic effect was found from the visual inspection from the wind rose plots.

We performed bimodal analysis (Chapter II, [98]) of the filtered cells (according to criteria described in the cell tracking section in materials and methods) to reveal any differences in the amount of time the cells spend in directional and re-orientation modes with and without EGF temporal gradient. Our motivation for application of bimodal analysis was driven by the hypothesis that the cells would be expected to spend more time in directional mode (in comparison to cells in control condition) in the situation where they were actually sensing the time-increasing concentration of EGF. A decrease in time spent during re-orientation mode with exposure of temporal gradient of EGF would also imply a temporal sensing component to chemotaxis. Fig. 6.7 depicts the mean mode times for both directional and re-orientation modes for the three cell types (pBabe (top), neuN (middle) and neuT (bottom)). We did not find any significant differences in

the mean mode times between the control and EGF treatment conditions, indicating no temporal sensing component in chemotaxis due to EGF. The amount of EGF being added via the temporal gradient setup was confirmed to be enough to saturate 45% of cellular surface receptors after 5 hours of EGF injection, using the formula:

$$N_b = \frac{N_t * S}{K_d + S}$$

derived by Rivero and coworkers [19] where N_b is the number of bound cell-surface receptors, N_t is the total number of receptors, S is the substrate concentration ($S = 100 pg/ml$ after 1 hour of EGF injection in our experimental setup) and K_d is the receptor-ligand dissociation equilibrium constant (we assume $K_d = 0.1nM = 600 pg/ml$[118], for EGF with molecular weight of 6kDa). Thus, for the values of S and K_d after 5 hours of EGF injection,

$$\frac{N_b}{N_t} = \frac{500 pg/ml}{600 pg/ml + 500 pg/ml} = 0.45$$

The mean squared displacement trends also indicated that there was no influence on the directional persistence (i.e., any temporal sensing chemotactic effect) in cells. Fig. 6.8 show the mean squared displacement trends for the three cell types (a: pBabe, b: neuN and c: neuT). The control trends (indicated in green) last for 2 hours while the trends for EGF treatments last approximately for 3.33 hours (shown in brown). We can see that both the trends have the same persistence, and there does not seem to be any chemotactic effect due EGF temporal gradient on the persistence in the cells.

EGF stimulation has been found to increase or decrease cell speed and directional persistence depending on the extra cellular matrix conditions. In our case, we just found a chemokinetic effect and no chemotactic effect due to the temporal gradient of EGF. It

has been found that in Chinese hamster ovary cells transfected with EGF receptor (EGFR), EGF stimulation led to a slight decrease in cell speed in the presence of fibronectin coating on 2D substrates [45]. In Fibroblasts as well, it was reported that EGF could increase or decrease cell speed depending on the underlying substrate composition [119]. The same authors (Maheshwari and coworkers, [48]) showed that in human mammary epithelial cells expressing EGFR, the mode of presentation of soluble factors such as EGF ligand could decide the resulting cell speed and directional persistence after EGF stimulation. It was found that the exogenous addition of EGF to EGFR expressing cells led to a decrease in the cell speed explaining our results with the MCF-10A neuT cell line. On the other hand, the increase in cell speed for neuN cell line could be speculated to be due to the presence of some form of autocrine EGF growth factor signaling [48].

It has been reported that EGFR receptor stimulation by EGF can lead to increased actin polymerization rate in the leading edge[120, 121]. It can be speculated that spatial sensing might be playing crucial role in the degree of actin polymerization, which in turn could be directly proportional to the number and distribution of bound receptors. The actin polymerization rate and its spatial localization would determine the polarity of the cell, depending on which directional or re-orientation modes are flagged, thus, making spatial sensing important for establishing cellular polarity via actin cytoskeletal re-arrangement. During chemotaxis, the bound EGF receptors could be localized to a preferential leading edge contributing to extension of directional mode and/or early termination of a re-orientation mode. This could fit into the scaling relationship discussed in Chapter V by increasing the directional mode time and or decreasing the re-orientation

mode time via spatial sensing of EGF. Hence, there is a possibility of connecting non-directed and chemotactic epithelial cell motility (induced by EGF via spatial sensing) by a general scaling mechanism as was shown for *Dictyostelium*.

6.5 Conclusions

We did not find any significant chemotactic effect of a temporal gradient of EGF on mammary epithelial cells in the *in vitro* conditions we studied. This suggests that these cells may not be employing temporal sensing in the *in vitro* conditions under consideration. However, this does not rule out the possibility of temporal sensing in the *in vivo* conditions or a differently modulated *in vitro* condition. Recently, it was reported that EGF induced strong increase in directional persistence in conjunction with optimum matrix density in 3D matrices while in 2D, EGF stimulation led to a decrease in directional persistence [122].

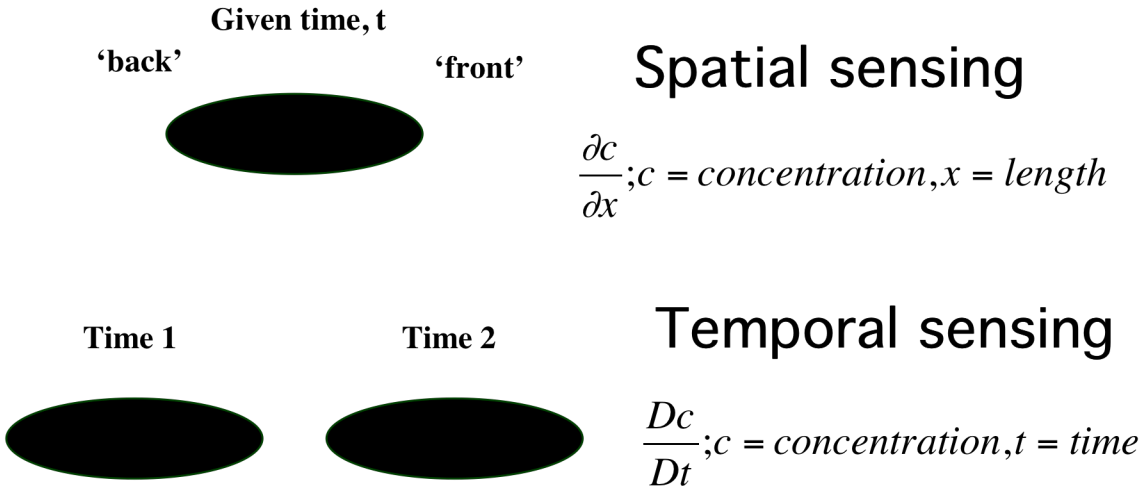

Figure 6.1: The different mechanisms employed by a cell to sense a chemoattractant gradient. The spatial sensing is illustrated at the top while temporal sensing (used during bacterial chemotaxis) is depicted at the bottom.

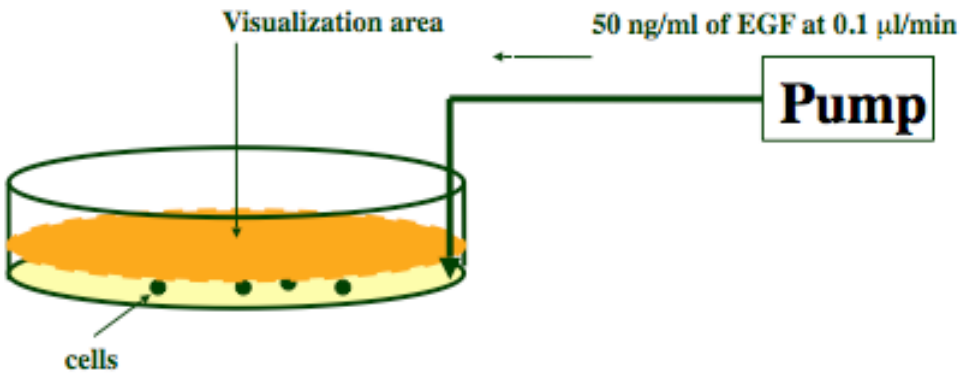

Figure 6.2: Experimental setup to subject epithelial cells to time-increasing concentration of EGF.

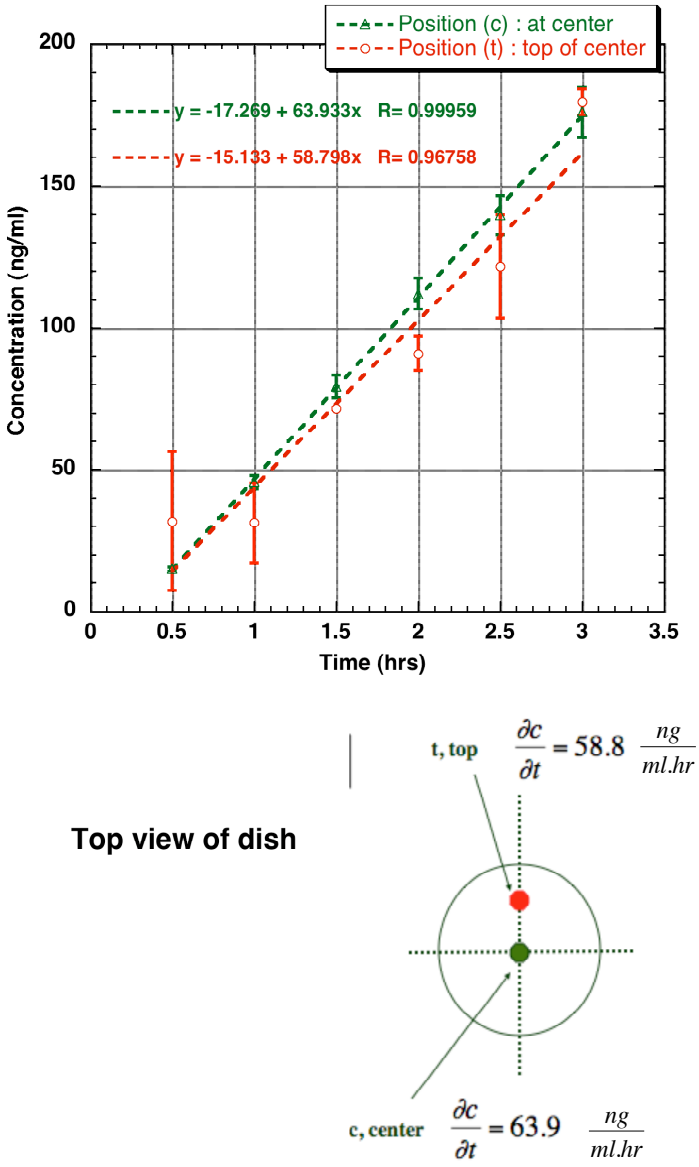

Figure 6.3: Gradient quantification experimentally using FITC-dextran (10kDa) molecule. The top view of the cell culture dish with points of measurement, *t*, top and *c*, center located. The microscope visualization area was located in the location indicated by *c*.

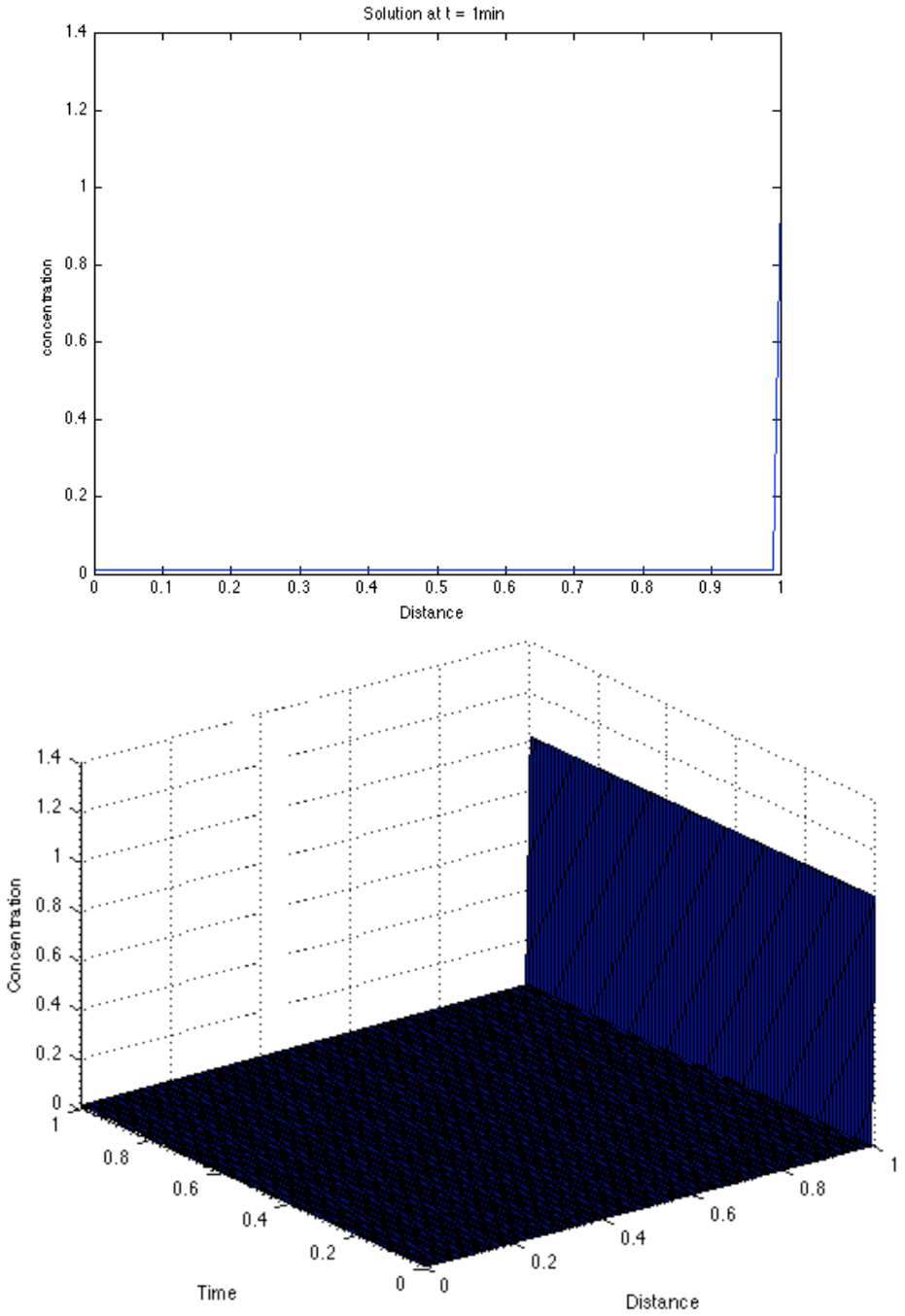

Figure 6.4a: Gradient quantification using simulations. Simulated concentration profiles across the cell culture dish as a function of non-dimensionalized concentration ($\bar{c}$) and distance ($\bar{x}$) after 1minute of EGF injection.

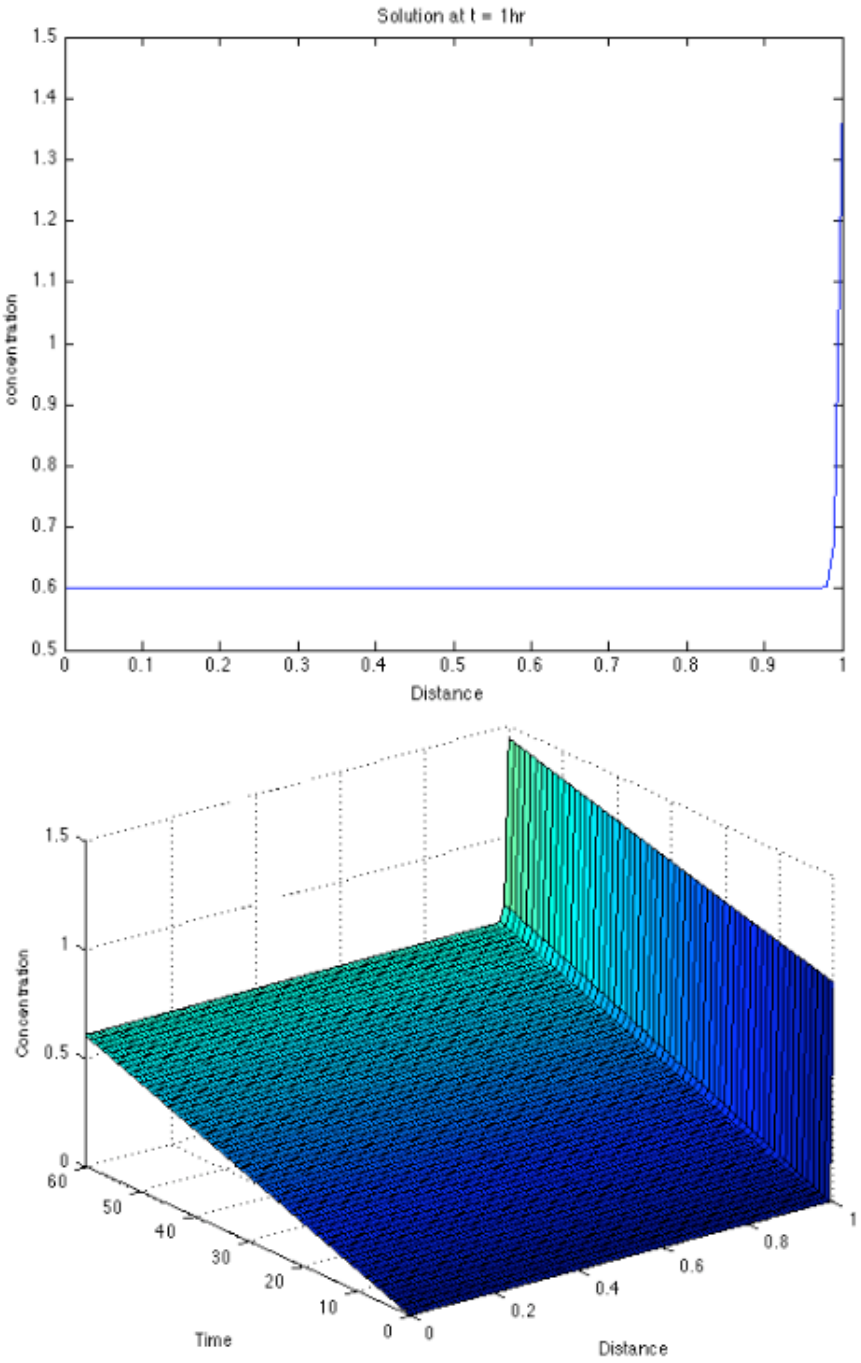

Figure 6.4b: Gradient quantification using simulations. Simulated concentration profiles across the cell culture dish as a function of non-dimensionalized concentration ($\bar{c}$) and distance ($\bar{x}$) after 1 hour of EGF injection.

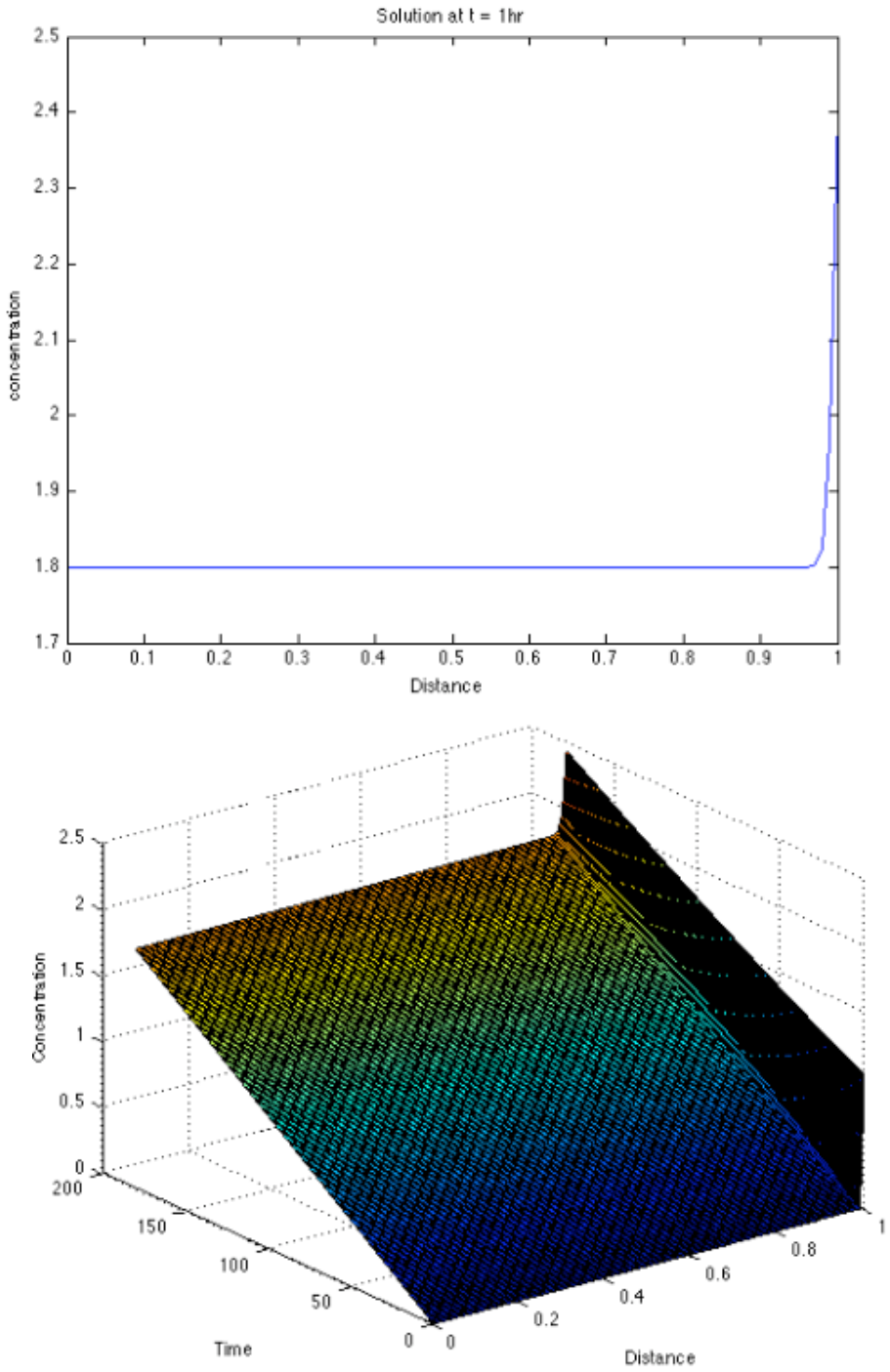

Figure 6.4c: Gradient quantification using simulations. Simulated concentration profiles across the cell culture dish as a function of non-dimensionalized concentration ($\bar{c}$) and distance ($\bar{x}$) after 3 hours of EGF injection.

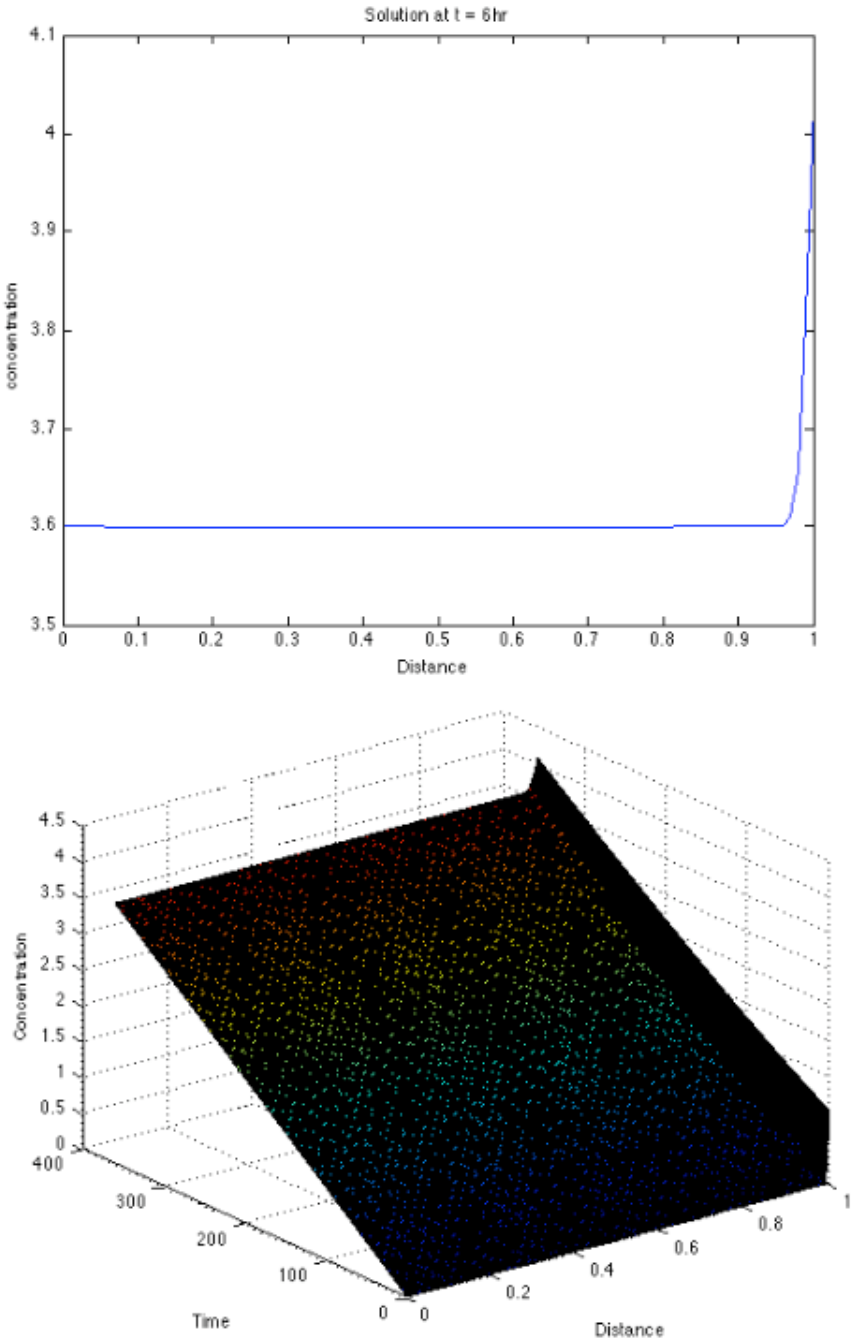

Figure 6.4d: Gradient quantification using simulations. Simulated concentration profiles across the cell culture dish as a function of non-dimensionalized concentration ($\bar{c}$) and distance ($\bar{x}$) after 6 hours of EGF injection.

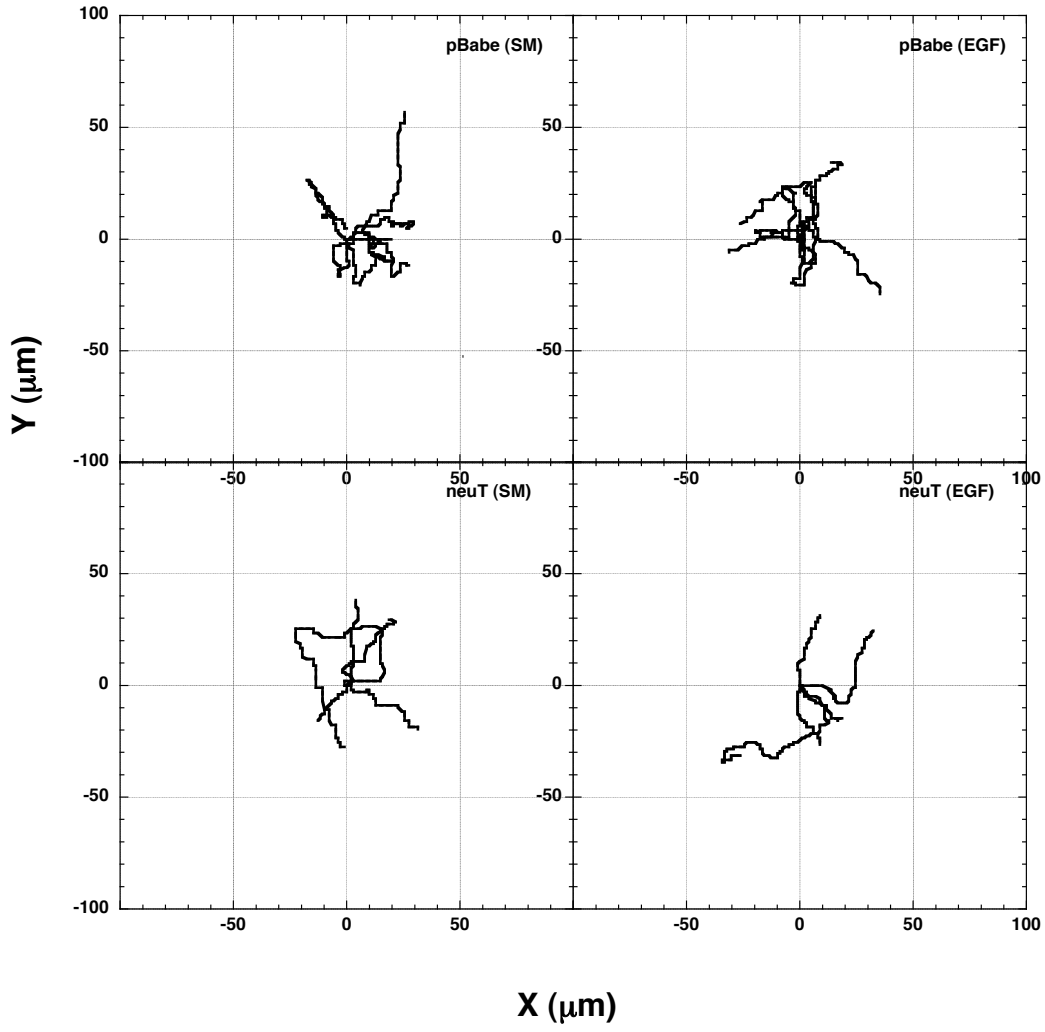

Figure 6.5: Wind rose plots of pBabe and neuT trajectories without EGF gradient, i.e., in SM (shown in left panel) and with EGF temporal gradient (shown in right panel). All the trajectories correspond to an experimental time of 2 hours.

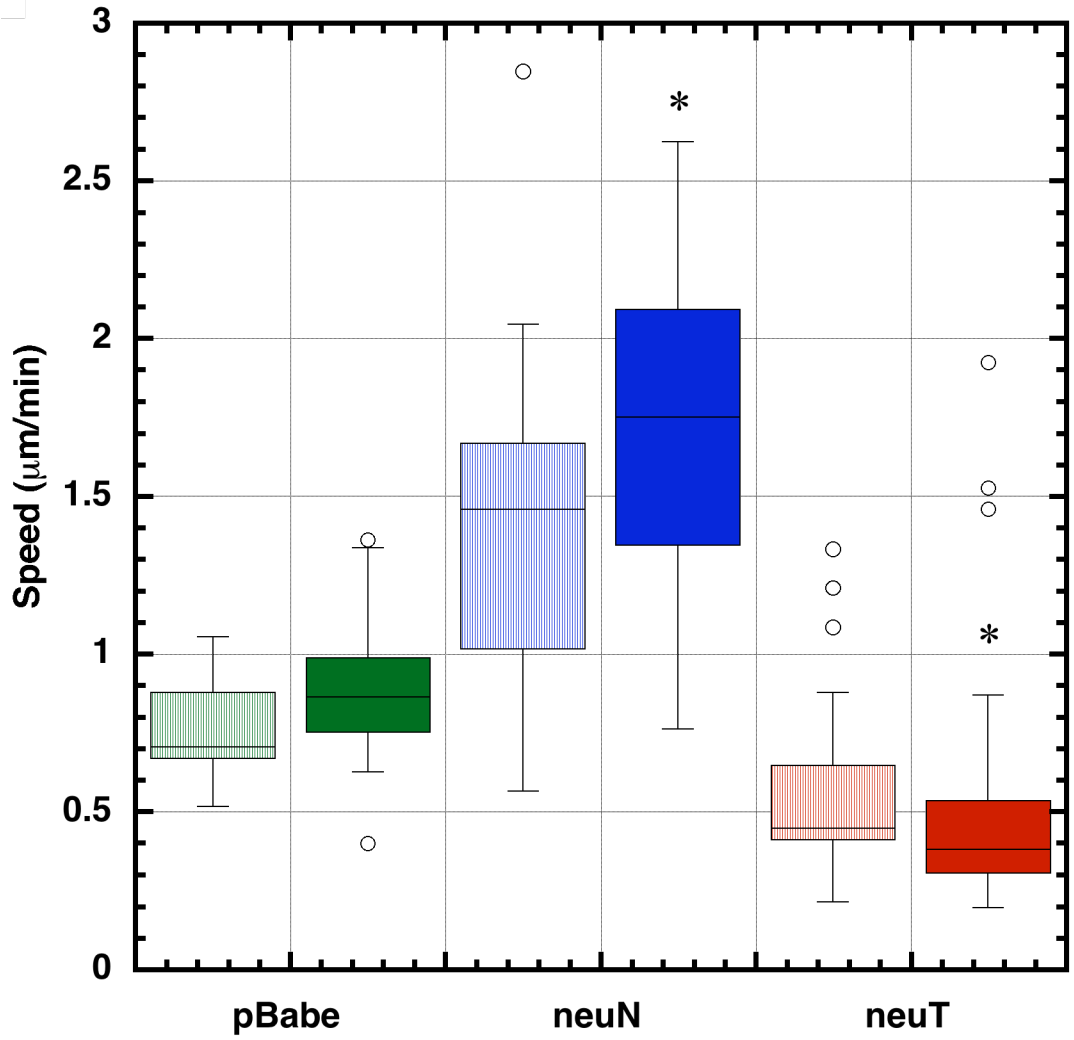

Figure 6.6: Mean cell speed for the three cell types with and without EGF stimulation. The light-shaded columns indicate the control cell speeds while filled columns indicate the cells speeds after EGF treatment. A two-sample Kolmogorov-Smirnov test at 5% significance level indicated an increase in cell speed for neuN while a decrease for neuT in comparison with respective controls.

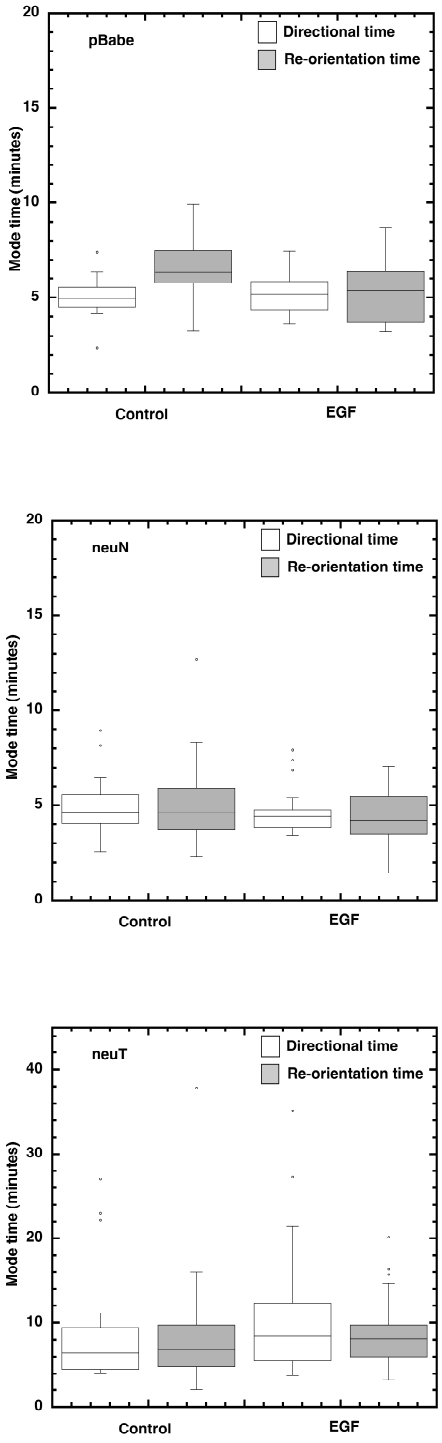

Figure 6.7: Mean directional mode and re-orientation mode times for the three cell types with (EGF) and without EGF stimulation (control). No significant differences were found in the mode times with and without EGF stimulation.

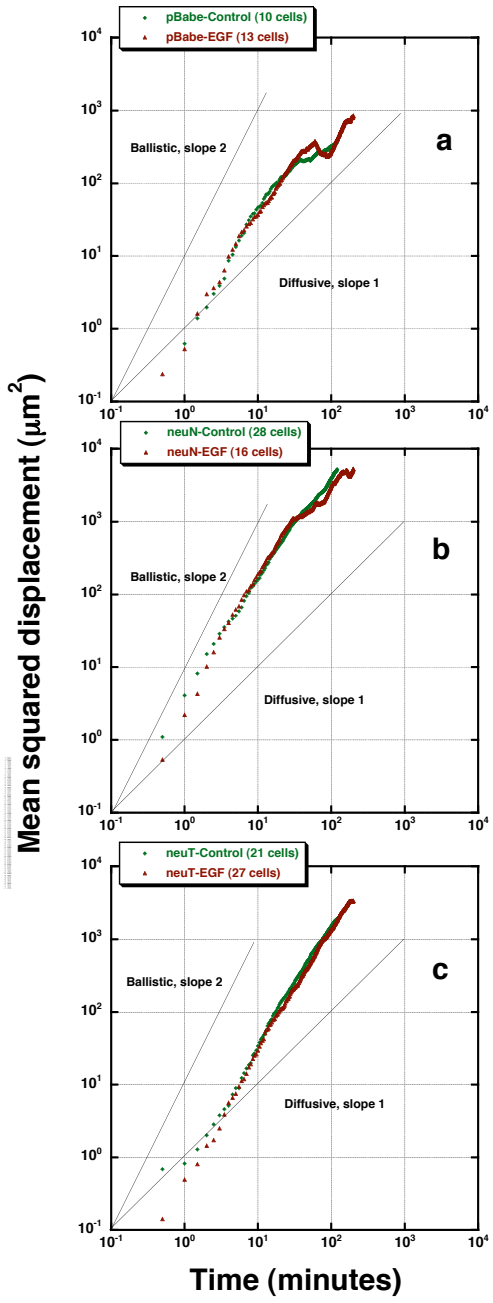

Figure 6.8: Mean squared displacement trends for the three cells types with and without EGF stimulation. The control trend is for 2 hours while the EGF stimulation one is for approximately 3.33 hours. The number of cells for each case has been indicated in the plot.

CHAPTER VII

BIMODAL ANALYSIS OF PROSTATE CANCER CELL RANDOM MIGRATION ON LAMININ-332 SUBSTRATE

7.1 Abstract

The bimodal analysis technique we developed (and described in Chapter II) was used to quantify the differences between single cell migration of wild type and mutant prostate cancer cells (low matriptase-expressing LNCaP cells and matriptase-overexpressing LNCaP cells, respectively). The single cell migration experiments were performed on substrates coated with laminin-332. Matriptase overexpression in the prostate cancer cells leads to a more persistent and faster phenotype. It was found that matriptase overexpression resulted in increased persistence as indicated by the wind rose plots and mean squared displacement trends. This can be attributed to the shorter time duration of re-orientation modes (which serves as a phase to randomize the cell trajectory) in matriptase cells (compared to the wild type cells), thus, contributing to the increased overall persistence in this phenotype. The directionality ratio of the displacement to the distance traversed (d/t ratio) in the re-orientation mode was found to be higher in the matriptase cell type resulting in a "more persistent" re-orientation mode confirming the increased persistence in this cell type. The matriptase mutation also contributed to a slightly faster phenotype as indicated by the increase in the mean cell speed. Again, this

could be explained by the fact that these cells spend less time in re-orientations and hence can travel further via the directional modes.

7.2 Background

Prostate cancer is the second leading cause of cancer death in men in USA [123] and the metastasis of the primary tumor to remote sites such as bone is the main cause of mortality [124]. An important step in metastasis is the break down of basement membrane and the remodeling of the extra-cellular matrix (ECM) [125]. The role of cell surface matrix proteinases in degradation of ECM molecules (such as laminin) leading to subsequent increase in cell migration has been reported in literature [126]. Laminin-332 (Ln-332), which was previously known as laminin-5, is known to be an important component of ECM [127]. It was recently reported to be a substrate for type II transmembrane serine protease, hepsin [128]. It was found that hepsin-overexpressing prostate cancer cells exhibited increased migration on Ln-332 substrates due to efficient proteolytic cleavage of the Ln-332 substrate. The overexpression of the type II transmembrane serine proteases such as hepsin and matriptase have been associated with progression of prostate cancer [129, 130].

In this work, we have quantified the difference in single cell motility between low-matriptase expressing prostate cancer cells and matriptase overexpressing cells using bimodal analysis. Bimodal analysis (Chapter II) was used to decipher the cause of phenotypic difference due to matriptase overexpression in terms of directional and re-orientation modes in an effort to pinpoint any crucial parameter contributing to increased migration associated with protease overexpression. Also, the single cell parameters obtained from the analysis will be useful in the development of more realistic

computational models of prostate cancer progression. This work was done in collaboration with Manisha Tripathi (Quaranta lab).

7.3 Materials and methods

7.3.1 Cell culture

LnCaP (low matriptase expressing, *wt*) and matriptase-overexpressing (*mt*) prostate cancer cells were created by Dr. Daniel Kirchhofer at Genentech and were cultured in RPMI 1640 medium supplemented with 10% fetal bovine serum, 500 $\mu g/ml$ Geneticin (Invitrogen), 0.5 $\mu g/ml$ puromycin (Sigma), and 1% glutamine/penicillin/streptomycin and incubated with 5% CO_2 and 37^{O}C.

7.3.2 Cell motility assay

The migration of cells was followed under random motility conditions without the presence of any externally added chemo-attractant gradients. All the three cell types were plated overnight at a low density of 20,000 cells on 60 mm dishes coated with Ln-332 (10 $\mu g/ml$) to avoid interacting cell populations.

The cells were monitored using the phase-contrast optics in a Zeiss Axiovert 200M inverted microscope with a monochrome, cooled CCD camera (CoolSNAP HQ, Roper Scientific, Trenton, NJ) equipped with temperature-controlled, humidified chamber. Cellular images were captured using MetaMorph (Molecular Devices Corporation, Sunnyvale, CA) for data acquisition and analysis. The time-lapse images were collected at a magnification of 10x (1 pixel $\equiv$0.98 μm) and using a sampling time interval of 1 minute. All the cells were equilibrated in the humidified, temperature controlled (37 ^{0}C) microscope chamber for half an hour and media was replaced with

fresh growth media before data collection. The cells were followed for at least twelve hours in all the three sets of experiments.

7.3.3 Cell tracking

Each cell was tracked by following the cell nucleus using the "track objects" function in MetaMorph. Only single cells were considered for the analysis. Cells that remained stationary, or moved outside the viewing area, underwent cell division during the course of the experiment, did not migrate over a distance of at least 2 cell bodies (<20 μm) or that adhered to other cells were excluded from the tracking procedure. Applying this criterion, ~60% cells were retained.

7.3.4 Bimodal analysis

Bimodal analysis (which segregates a cell track into alternating directional and re-orientation modes) is described in detail elsewhere (see Chapter II and ref. [98]). Briefly, the directional and re-orientation modes were flagged by first computing instantaneous direction change (ϕ) at each frame (time point) and then applying a cut-off (ϕ_{cut}) to flag the modes. A cut-off value of $\phi_{cut} = 45°$ and 'r3 criterion' (ϕ value at three successive frames determines a directional mode) was used for all the data analysis. The choice of $\phi_{cut} = 45°$ (cut-off value) is heuristic in nature and is discussed elsewhere [98]. This cut-off value best succeeded in flagging the re-orientation mode for the different cell types under consideration. The turn angle, θ (the angle change between successive directional modes) was computed using multi-point linear regression of all the data points constituting a directional mode. The details of all the rules used to locate the modes can be found in ref. [98] or Chapter II.

7.3.4 Statistical Analysis

All statistical analysis was done in MATLAB software package (MathWorks, Natick, MA). The Lilliefors test (lillietest.m) was used to test if the data were parametric or non-parametric. A two-sample Kolmogorov-Smirnov test (kstest2.m in MATLAB) was used to compare between the two cell-types if the data were non-parametric; otherwise the t-test (ttest2.m in MATLAB) was used. A p-value <0.05 indicates significant differences.

7.4 Results and discussions

After filtering the cells to be used in the analysis (according to the constraints mentioned in the 'cell tracking' section above), wind rose plots were made to examine the persistence in the cell types qualitatively. Some example 12-hour trajectories of *wt* and *mt* cells (8 cells, each in different color) are shown in Fig. 7.1. These wind rose plots ($200\,\mu m$ X $200\,\mu m$) indicate that the *mt* cells (Fig. 7.1, bottom) are more persistent and travel farther compared to the *wt* cells (Fig. 7.1, top). The black dotted circle on the wind rose plots indicates the root mean squared dispersal. The mean cell speed (total distance traveled divided by time averaged over all cells) for *mt* cell type was found to be higher when compared to wt cells ((p=0.0034), n=32 (*wt*), n=35 (*mt*)). This is shown in the box plot in Fig. 7.2. Lilliefors test (lillietest.m function in MATLAB) was initially applied and the mean cell speed data for the cells were found to be distributed parametrically.

Bimodal analysis was applied to the cells tracks and mean directionality (d/t) ratios (ratio of direct displacement (d) to total distance (t) for a given mode) were computed. For correctly segregated directional and re-orientation modes (as discussed in Chapter II), the average ratio for directional modes for a given cell type (d_{wt} or d_{mt}) can be expected to be closer to 1 (highest possible directionality indicating greater

persistence) while for re-orientation modes (r_{wt} or r_{mt}) the values are expected to be smaller than those for directional modes. Figure 7.3 displays the mean d/t ratios for the two cell types and it can be seen that the ratio is higher in directional mode compared to re-orientation mode for both cell types [*wt* (p= 8.2554e-158, n=490), *mt* (p= 7.0964e-241, n=816)] confirming the existence of two distinct modes in the cell paths. The re-orientation mode ratio of *mt* cell type was found to higher [(p=6.0854e-10), n=490 (*wt*), n=816) (*mt*)] compared to that for *wt* cells indicating that the *mt* cells are more persistent than *wt* cells during this mode. This is also reflected in the mean mode time values for the cells as shown in Fig. 7.4. The error bars are the standard deviations in the mean values. The mean re-orientation time for *mt* cell type was found to be less than that of the *wt* cells, indicating that the re-orientations in the *mt* cells last for lesser duration compared to *wt* cells (that is, *mt* cells spend more time in directional modes compared to *wt* cells), contributing to the increased persistence in the *mt* cells [(p=0.6618e-05), n=490 (*wt*), n=816) (*mt*)]. There was no significant difference in the mean directional mode times for the two cell types. Hence, the re-orientation modes of *mt* cells are more persistent contributing to the overall increased persistence in these cells.

The directional and re-orientation mode time distributions for the prostate cancer cells are found to be exponentially distributed (Fig. 7.5). Hence, the fitting parameter λ, for the mode time (x) distribution ($P(t) = \lambda e^{-\lambda x}$), is the inverse of the mean value of the mode time, x. One can see that the smallest directional mode time possible is around 3 minutes and 1 minute for re-orientation mode (as constrained by the criteria used to perform the analysis (see Chapter II and ref. [98]) since the sampling interval used to collect the time lapse images was 1 minute. It can be seen from Fig. 7.5, bottom, that the

re-orientation mode time distribution for *mt* cells has higher fitting parameter λ and the distribution decays faster compared to *wt* cells, again indicating that mean re-orientation mode time for *mt* cells is smaller than *wt* cells. On the other hand, the difference in the fitting parameters for the directional mode times (Fig. 7.5, top) is not significant as was implicated by the d/t ratios. The turn angle distribution (direction changes between successive directional modes) for the two cell types is shown in Fig. 7.6. We can see that there is no significant difference and inherently both cell types have certain degree of persistence characteristic of mammalian cells. This is also evident from the mean squared displacement trends (Fig. 7.7a) for the two cell types and we can see that on the log-log plot, both the cell types have slopes greater than the diffusive regime (slope 1 line) and less than the ballistic (slope 2 line) indicating super-diffusive behavior in both cells over the experimental time scale considered. However, one can see that the *mt* cells are more persistent and disperse farther compared to *wt* cells (clear from the wind rose plots in Fig. 7.1) which could be due to both higher mean cell speed as well as greater directionality during the re-orientations for the *mt* cells. The *mt* cells have higher super-diffusivity (implicating more persistence) compared to *wt* cells. This is evident in Fig. 7.7b where we can see that the linear–fit of logarithm of mean squared displacements (versus logarithm of time) gives a slope of 1.54 for *mt* cells and a lesser slope of 1.15 for *wt* cells. Hence, the *mt* cells retain more persistence compared to *wt* cells that are only slightly super-diffusive (diffusive regime corresponds to slope=1).

We also examined the scaling law relationship between the mean mode times (established in Chapter V for *Dictyostelium*, mammary epithelial, fibroblasts and leukocytes). It is found that even the prostate cancer cells follow the non-linear

relationship between the directional and re-orientation modes (Fig. 7.8, top). The mean mode times (on a log-log scale) moving from *wt* to *mt cells* display a trend (Fig. 7.8, bottom) similar to that found in the transition from non-directed to directed *Dictyostelium* motility in Chapter V indicating the presence of some general mechanisms of increasing persistence in eukaryotic cells. The more persistent *mt* cells are on the bottom right, meaning that their re-orientation mode times are smaller.

The turn frequency (which could be approximated as the reciprocal of average directional mode time) for both the cell types was found to be same in spite of the *mt* cells being more persistent. This can be explained by noting that even though the number of re-orientations in the *mt* cell type is more than those of *wt* cells, the mean directional mode time remains the same for both the cells. Longer re-orientations (lasting for more time) imply more randomization of the cell trajectory while shorter re-orientations do not allow total loss of previous memory and the persistence in maintained for the cell. Hence, even though *mt* cells have a greater number of shorter re-orientations compared to *wt* cells (with small number of longer re-orientations), their persistence is maintained in comparison to the *wt* cells.

Hence, bimodal analysis permits the determination of the factor contributing to the increased persistence in cells due to matriptase overexpression. We find that the re-orientations mode durations are shortened due to the protease overexpression. One can speculate that the enhanced proteolytic activity in cells permits them to continue moving in the same direction with ease since the cells wander less.

7.5 Conclusions

Bimodal analysis was applied to cell-migration tracks of prostate cancer cells (with and without matriptase overexpression) on Ln-332 substrate. We find that *mt* cells (compared to *wt* cells) exhibit greater persistence and travel farther during the experimental time-scale of 12 hours. This can be attributed to increased speed and greater directionality in re-orientation modes, in the *mt* cell type. Bimodal analysis identified the shortening of re-orientation modes in *mt* cells as a main contributor to the enhanced directionality in *mt* cells.

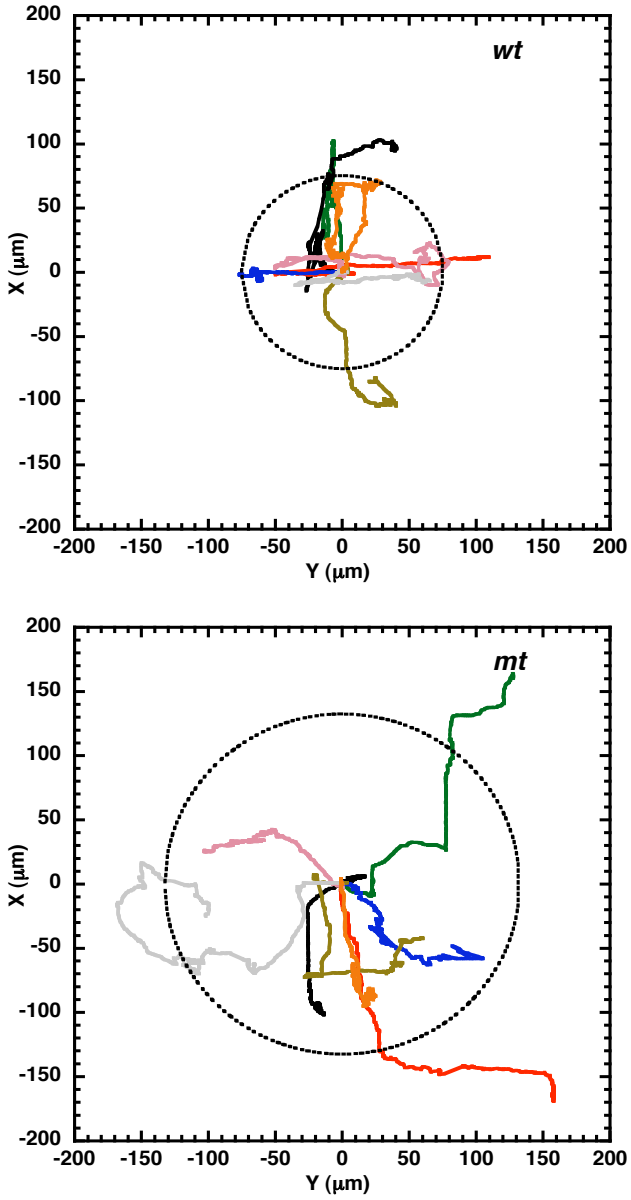

Figure 7.1: Wind rose plots (cell tracks starting from (0,0)) for eight 12-hour trajectories (represented by different color) of *wt* and *mt* cell types each. The plot indicates that *mt* tracks (bottom) display greater persistence and travel farther compared to *wt* tracks (top). The black dotted circle in both plots shows the root mean square dispersal after 12 hours averaged over all cells for each cell type.

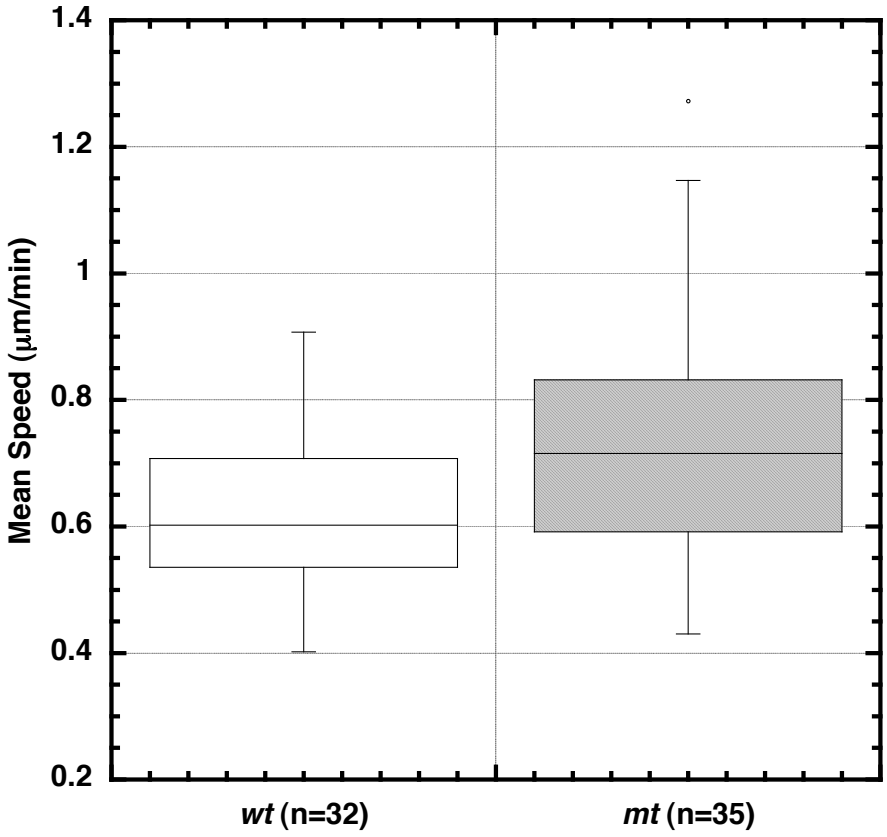

Figure 7.2: Box plots of the mean cell speed for the *wt* (n=32) and *mt* (n=35) cell types. The average cell speed for the *mt* cells was found to be higher between the two cell types (p=0.0034) using two-sample t -test (ttest2.m function in MATLAB) at 5% significance.

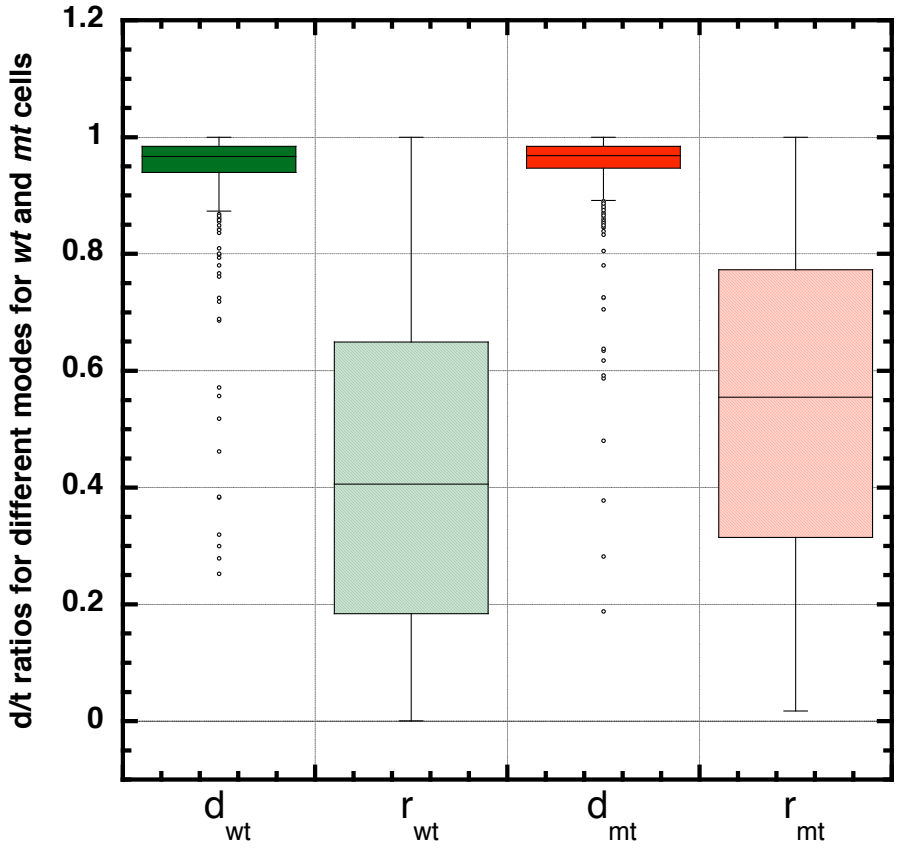

Figure 7.3 Box plots of mean d/t ratios for the two cell types during the directional (d_{wt} or d_{mt}) and re-orientation (r_{wt} or r_{mt}) modes indicating the segregation of the cellular paths into distinct alternating directional and re-orientation modes [*wt* (p= 8.2554e-158, n=490), *mt* (p= 7.0964e-241, n=816)] using two-sample Kolmogorov-Smirnov nonparametric test. The mean d/t ratios during the re-orientation phase for *mt* cell type was found to be greater than that of *wt* cells (p=6.0854e-10) indicating that the re-orientations are more directional i.e., persistent for a *mt* cell type compared to a *wt* cell.

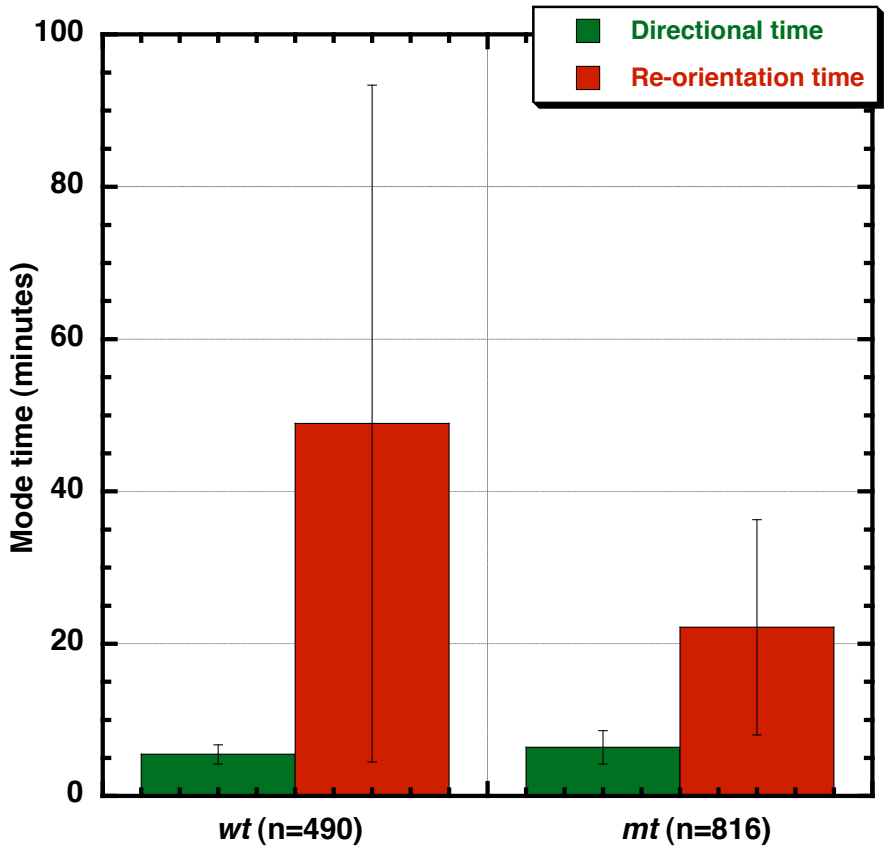

Figure 7.4: Mean directional and re-orientation mode times for the two cell types. Error bars represent the standard deviations in the mean mode times. The mean re-orientation time for *mt* cell type was found to be less than that of the *wt* type, contributing to the increased persistence in the *mt* cells (using nonparametric, two-sample Kolmogorov-Smirnov test, [(p= 0.6618e-05), n=490 (*wt*), n=816) (*mt*)].

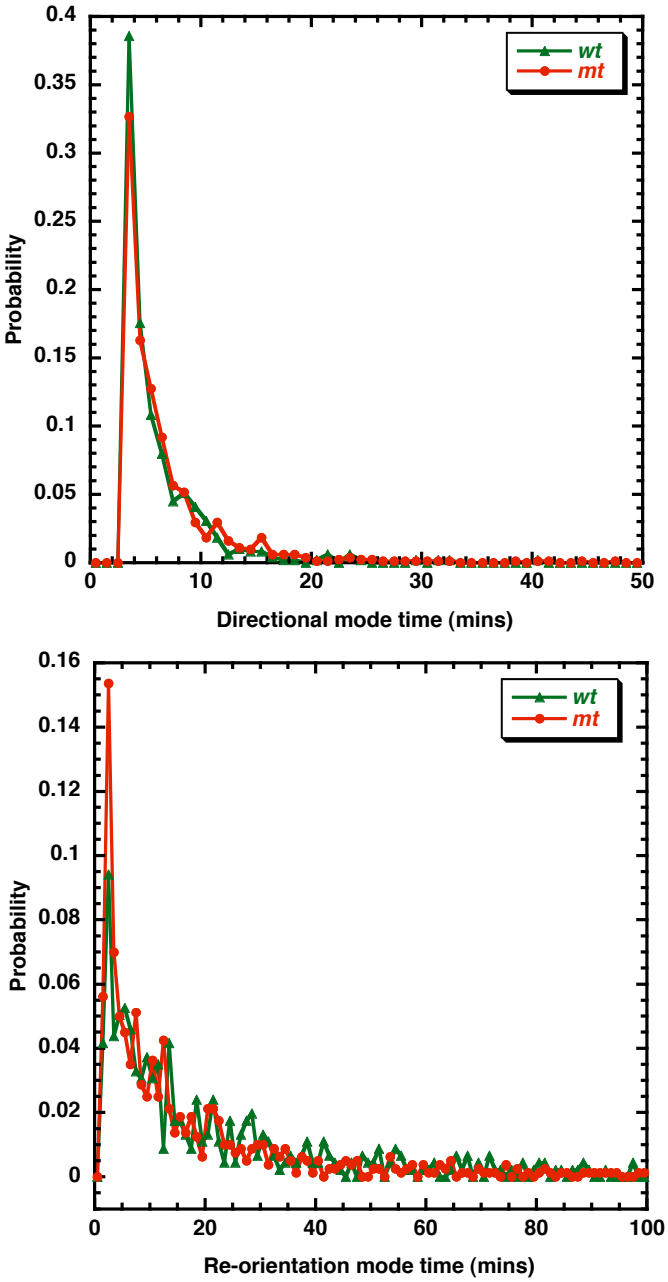

Figure 7.5: (Top) Directional mode time and (bottom) re-orientation mode time distributions for the two cell types. The mode time distributions are exponentially distributed and hence the inverse of the fitting parameter for the distribution is equivalent to the average mode time.

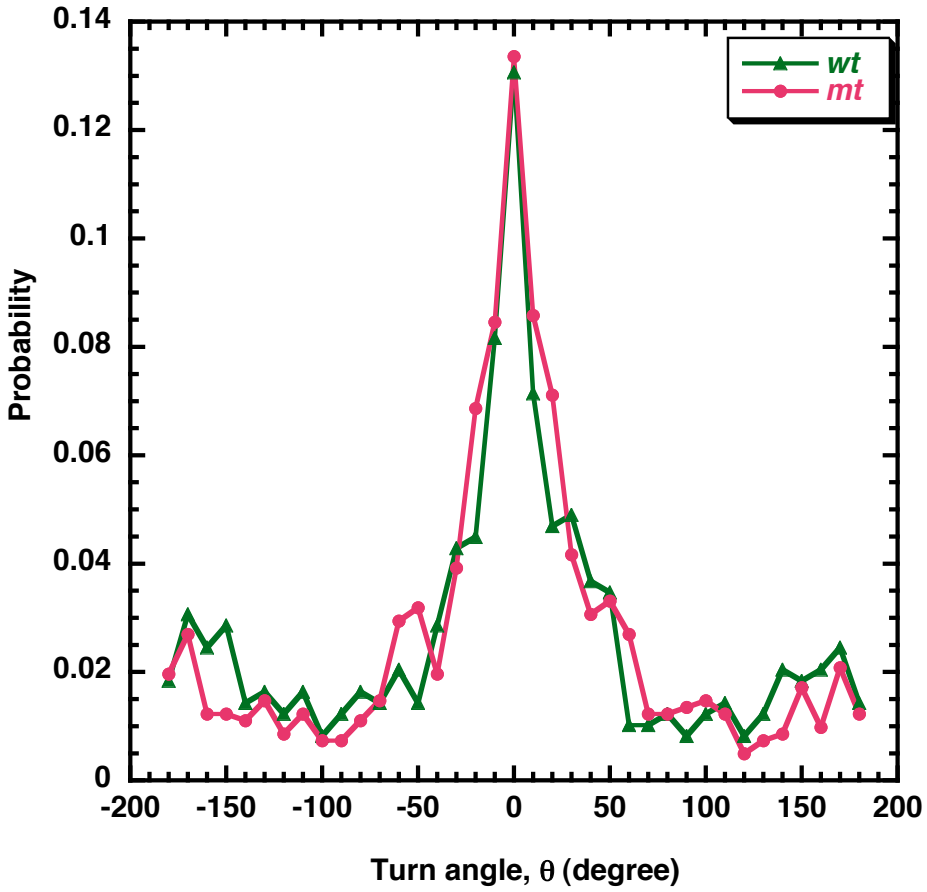

Figure 7.6: The turn angle distribution (between the directional modes) for the two cell types was found to be similar indicating that it is the directionality within the re-orientation modes that seems to control the overall persistence of the cell type.

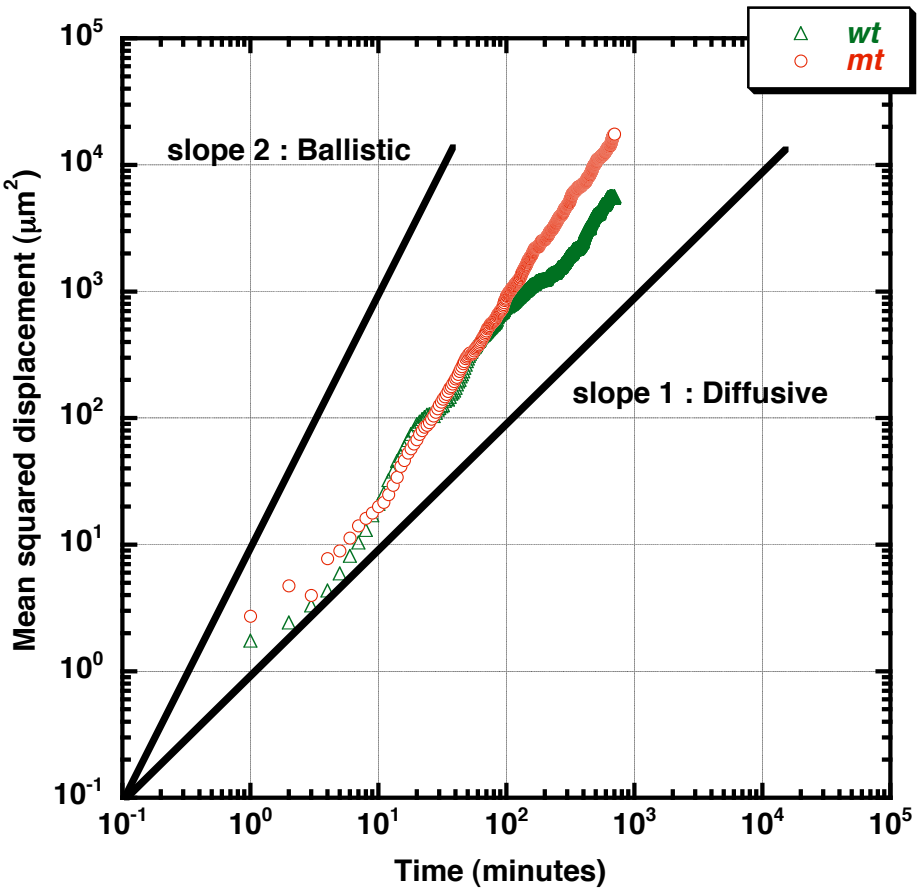

Figure 7.7a: Mean squared displacement trends for the two cell types over the course of 12 hours. Both the *wt and mt* cells display super-diffusive (close to ballistic line) motion at the end of 12 hours. The greater mean squared dispersal after 12 hours in the *mt* cells could be the result of both higher mean cell speed as well as greater directionality during the re-orientations.

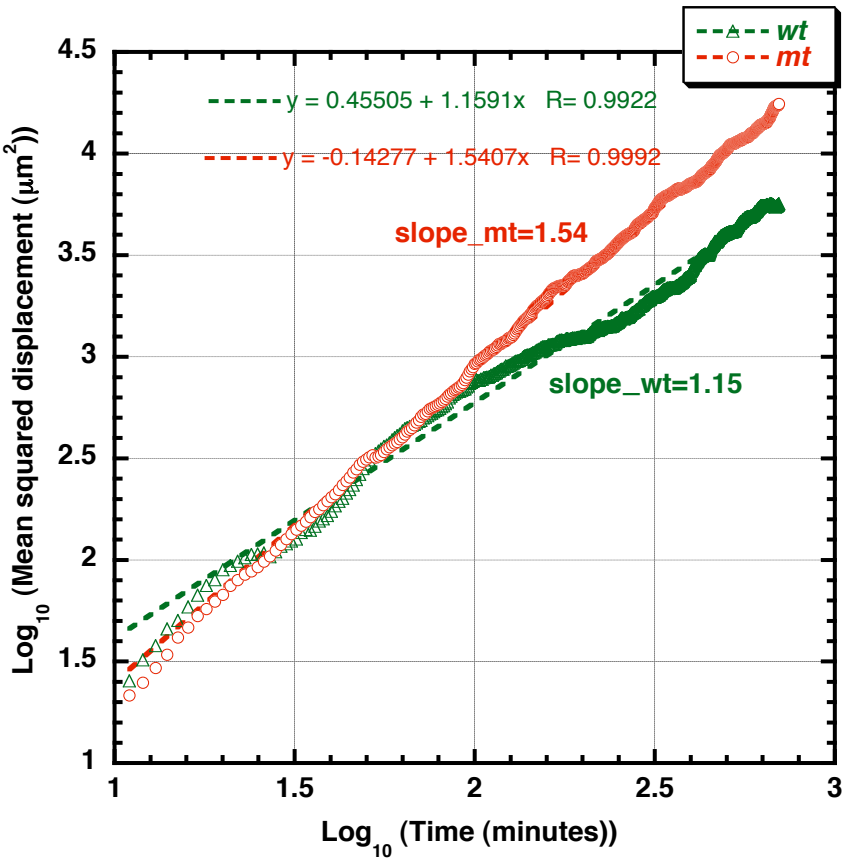

Figure 7.7b: Linear fit of the logarithm of mean squared displacement trends for the two cell types over the course of 12 hours. The *wt* cells are less super-diffusive (slope =1.15) compared to *mt* cells (slope=1.54) at the end of 12 hours.

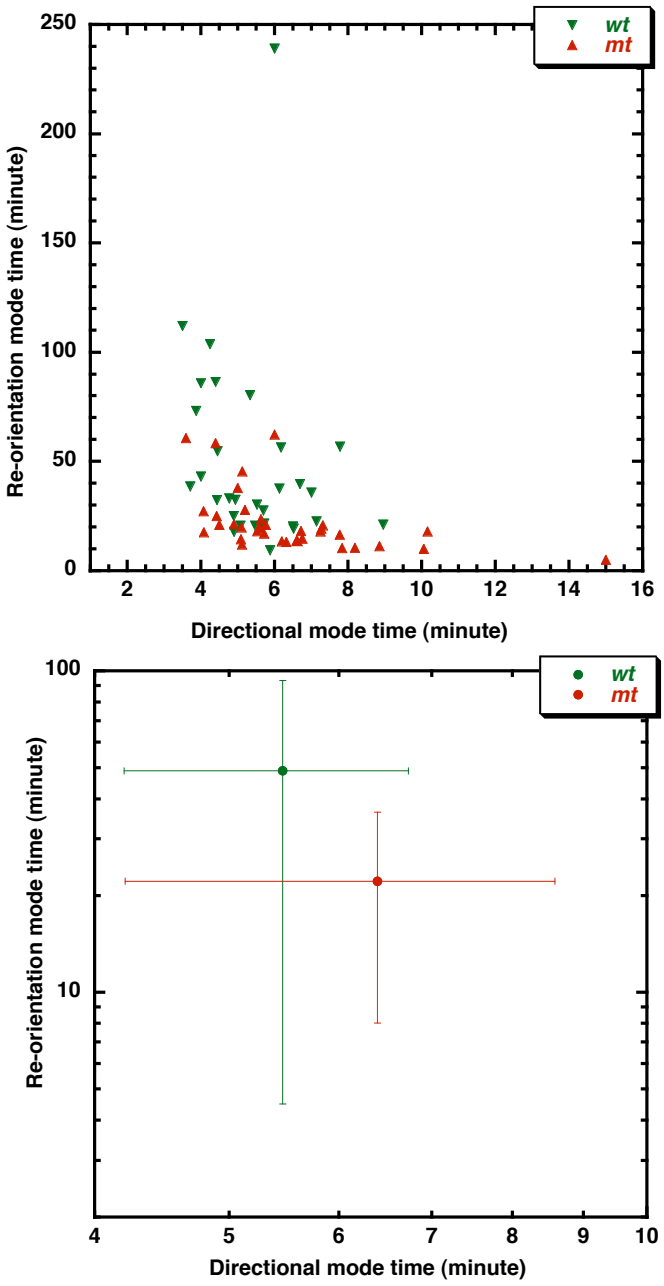

Figure 7.8: Top) Scaling law relationship between the mode times for prostate cancer cells; bottom) the mean mode times on a log-log plot for the two cell types, indicating that the more persistent *mt* cells are on the bottom right, meaning that their re-orientation mode times are smaller.

CHAPTER VIII

SUMMARY AND FUTURE WORK

8.1 Summary

In summary, bimodal analysis, a cellular-scale approach to characterize eukaryotic single cell migration by performing a model-based analysis of single cell video-microscopy data was developed and applied to several eukaryotic cell types. In Chapter II, bimodal analysis framework was initially developed for the MCF-10A cells based on the random motility migration data for these cells. The directional and re-orientation phases were identified and quantified. The single cell dynamics of these cells such as the turn probability and turn angle distribution were computed. This work of application of bimodal analysis to MCF-10A, mammary epithelial cells was published beginning of this year in Annals of Biomedical Engineering [98].

Simulations of mammary epithelial cell random migration using the parameters obtained from bimodal analysis of the MCF-10A panel of cell lines were performed using cellular dynamics (CD) scheme, originally developed for bacterial chemotaxis [35] and the neuT version (oncogenic expression of Her-2) was found to have higher random motility coefficient (described in Chapter III). A bimodal correlated random walk (BCRW) model was developed in an attempt to describe the foraging strategy of single mammary epithelial cells from multi-cellular organisms and a comparison between our BCRW model and persistent random walk model with experiments was made in Chapter IV.

In Chapter V, application of bimodal analysis to other eukaryotic cell types from *Dictyostelium,* neutrophils to fibrosarcoma apart from mammary epithelial cells was illustrated to arrive at a general scaling principle to describe non-directed and chemotactic cell motility. An experimental setup to subject MCF-10A cells to time increasing concentration of chemoattractant was described in Chapter VI and it was found that the temporal gradient did not induce any chemotactic effect on mammalian cells. The quantitative analysis of migration prostate cancer cells expressing different versions of matriptase protease on laminin-5 substrate was performed in Chapter VII and matriptase overexpressing cells were found to be more persistent.

8.2 Potential future work

Bimodal analysis could be modified to characterize single cell migration in three-dimensions, possibly in the *in vivo* environment, upon availability of such a data. One of the challenges will be to sample the cell migration process frequently and at a high resolution for application of bimodal analysis in 3-D. Application in 3-D could help in improved quantification of cell migration through intricate extra-cellular matrix pattern and reveal the effect of a particular cell type specific factor such as the over-expression of a protease on parameters such as turn angle distribution. This would also serve to quantify the differences between the 2-D and 3-D environments.

There is also the possibility of application of bimodal analysis to quantify cell migration in other cell types such as keratinocytes, lymphocytes, etc. Bimodal analysis could also be modified in future to accommodate an additional criterion that would explicitly take into account the cellular morphology, which would help in correlation to spatial distribution of a specific motility related protein such as actin. This could assist in

making a better connection between the observed overall cellular-level behaviors such as change in mean cell speed to the specific molecular process responsible for this outcome. Bimodal analysis could also be used to connect non-directed and chemotactic motility in epithelial cells by a scaling law as was shown for *Dictyostelium*.

The BCRW framework described in this work could be used in a more realistic description of mammalian cell motility for the development of potentially advanced models of tumor progression.

REFERENCES

1. Bray, D., *Cell movements: from molecules to motility*. 2nd ed. 2001: Garland Publishing, NY. 372.
2. Saltzman, W.M., *Tissue Engineering : Engineering Principles for the Design of Replacement Organs and Tissues*. 2004, New York: Oxford University Press.
3. Lauffenburger, D.A. and A.F. Horwitz, *Cell migration: A physically integrated molecular process*, in *Cell*. 1996. p. 359-369.
4. Huang, S., et al., *Symmetry-breaking in mammalian cell cohort migration during tissue pattern formation: Role of random-walk persistence*. Cell Motility And The Cytoskeleton, 2005. **61**(4): p. 201-213.
5. Yam, P.T., et al., *Actin-myosin network reorganization breaks symmetry at the cell rear to spontaneously initiate polarized cell motility*. Journal of Cell Biology, 2007. **178**: p. 1207-1221.
6. Ridley, A.J., et al., *Cell migration: Integrating signals from front to back*. Science, 2003. **302**(5651): p. 1704-1709.
7. Toetsch, S., et al., *The evolution of chemotaxis assays from static models to physiologically relevant platforms*. Integrative Biology, 2009. **1**(2): p. 170-181.
8. Dormann, D. and C. Weijer, *Imaging of cell migration*. EMBO J, 2006. **25**(15): p. 3480-3493.
9. *American Cancer Society : Cancer Facts and Figures 2007*. 2007, American Cancer Society: Atlanta.
10. Hanahan, D. and R.A. Weinberg, *The hallmarks of cancer*. Cell, 2000. **100**(1): p. 57-70.
11. Chambers, A.F., A.C. Groom, and I.C. MacDonald, *Dissemination and growth of cancer cells in metastatic sites*. Nature Reviews Cancer, 2002. **2**(8): p. 563-572.
12. Condeelis, J. and J.E. Segall, *Intravital imaging of cell movement in tumours*. Nature Reviews Cancer, 2003. **3**(12): p. 921-930.
13. Wang, W.G., et al., *Tumor cells caught in the act of invading: their strategy for enhanced cell motility*. Trends In Cell Biology, 2005. **15**(3): p. 138-145.
14. Xue, C.S., et al., *Epidermal growth factor receptor overexpression results in increased tumor cell motility in vivo coordinately with enhanced intravasation and metastasis*. Cancer Research, 2006. **66**(1): p. 192-197.
15. Muller, A., et al., *Involvement of chemokine receptors in breast cancer metastasis*. Nature, 2001. **410**(6824): p. 50-56.
16. Kakinuma, T. and S.T. Hwang, *Chemokines, chemokine receptors, and cancer metastasis*. Journal Of Leukocyte Biology, 2006. **79**(4): p. 639-651.
17. Rembold, M., et al., *Individual cell migration serves as the driving force for optic vesicle evagination*. Science, 2006. **313**(5790): p. 1130-1134.
18. Jourquin, J., et al., *Dispersal of epithelial cancer cell colonies by lysophosphatidic acid (LPA)*. Journal Of Cellular Physiology, 2006. **206**(2): p. 337-346.
19. Rivero, M.A., et al., *Transport Models for Chemotactic Cell-Populations Based on Individual Cell Behavior*. Chemical Engineering Science, 1989. **44**(12): p. 2881-2897.

20. Ford, R.M. and P.T. Cummings, *On the Relationship between Cell Balance-Equations for Chemotactic Cell-Populations (Vol 52, Pg 1426, 1992)*. Siam Journal on Applied Mathematics, 1993. **53**(5): p. 1505-1505.
21. Dickinson, R.B. and R.T. Tranquillo, *Transport-Equations And Indexes For Random And Biased Cell-Migration Based On Single-Cell Properties*. Siam Journal On Applied Mathematics, 1995. **55**(5): p. 1419-1454.
22. Anderson, A.R.A., *A hybrid mathematical model of solid tumour invasion: the importance of cell adhesion*. Mathematical Medicine and Biology-a Journal of the Ima, 2005. **22**(2): p. 163-186.
23. Anderson, A.R.A., et al., *Tumor morphology and phenotypic evolution driven by selective pressure from the microenvironment*. Cell, 2006. **127**: p. 905-915.
24. Selmeczi, D., et al., *Cell motility as persistent random motion: Theories from experiments*. Biophysical Journal, 2005. **89**(2): p. 912-931.
25. Doi, M. and S.F. Edwards, *The theory of polymer dynamics*. 1986, New York: Oxford Univeristy Press.
26. Uhlenbeck, G.E. and L.S. Ornstein, *On the theory of the Brownian motion*. Physical Review, 1930. **36**: p. 823-841.
27. Berg, H.C., *Random Walks in Biology*. 1983, Princeton, New Jersey, USA: Princeton University Press.
28. Le Douarin, N.M., *Cell migrations in embryos*. Cell, 1984. **38**(2): p. 353-360.
29. Berg, H.C. and D.A. Brown, *Chemotaxis in Escherichia-Coli Analyzed by 3-Dimensional Tracking*. Nature, 1972. **239**(5374): p. 500-504.
30. Berg, H.C., *Bacterial Behavior*. Nature, 1975. **254**(5499): p. 389-392.
31. Berg, H.C. and D.A. Brown, *Chemotaxis in Escherichia coli analyzed by three-dimensional tracking. Addendum. .* Antibiotics and Chemotherapy, 1974. **19**: p. 55-78.
32. Frymier, P.D., et al., *3-Dimensional Tracking of Motile Bacteria near a Solid Planar Surface*. Proceedings of the National Academy of Sciences of the United States of America, 1995. **92**(13): p. 6195-6199.
33. Duffy, K.J. and R.M. Ford, *Turn angle and run time distributions characterize swimming behavior for Pseudomonas putida*. Journal Of Bacteriology, 1997. **179**(4): p. 1428-1430.
34. Duffy, K.J., R.M. Ford, and P.T. Cummings, *Residence time calculation for chemotactic bacteria within porous media*. Biophysical Journal, 1997. **73**(6): p. 2930-2936.
35. Frymier, P.D., R.M. Ford, and P.T. Cummings, *Cellular-Dynamics Simulations of Bacterial Chemotaxis*. Chemical Engineering Science, 1993. **48**(4): p. 687-699.
36. Ford, R.M. and P.T. Cummings, *Mathematical models of bacterial chemotaxis*, in *Chapman and Hall Microbiology Series; Mathematical modeling in microbial ecology*, A.L. Koch, J.A. Robinson, and G.A. Milliken, Editors. 1998. p. 228-269.
37. Potdar, A., et al., *Bimodal Analysis of Mammary Epithelial Cell Migration in Two Dimensions*. Ann Biomed Eng, 2009. **37**(1): p. 230-245.
38. Dunn, G.A. and A.F. Brown, *A Unified Approach To Analyzing Cell Motility*. Journal Of Cell Science, 1987. **8**: p. 81-102.

39. Dickinson, R.B. and R.T. Tranquillo, *Optimal Estimation Of Cell-Movement Indexes From The Statistical-Analysis Of Cell Tracking Data*. Aiche Journal, 1993. **39**(12): p. 1995-2010.
40. Othmer, H.G., S.R. Dunbar, and W. Alt, *Models Of Dispersal In Biological-Systems*. Journal Of Mathematical Biology, 1988. **26**(3): p. 263-298.
41. Kouvroukoglou, S., et al., *Endothelial cell migration on surfaces modified with immobilized adhesive peptides*. Biomaterials, 2000. **21**(17): p. 1725-1733.
42. Gail, M.H. and C.W. Boone, *Locomotion Of Mouse Fibroblasts In Tissue Culture*. Biophysical Journal, 1970. **10**(10): p. 980-993.
43. Bergman, A.J. and K. Zygourakis, *Migration of lymphocytes on fibronectin-coated surfaces: temporal evolution of migratory parameters*. Biomaterials, 1999. **20**(23-24): p. 2235-2244.
44. Dimilla, P.A., et al., *Measurement Of Individual Cell-Migration Parameters For Human Tissue-Cells*. AIChE Journal, 1992. **38**(7): p. 1092-1104.
45. Harms, B.D., et al., *Directional persistence of EGF-Induced cell migration is associated with stabilization of lamellipodial protrusions*. Biophysical Journal, 2005. **88**(2): p. 1479-1488.
46. Ionides, E.L., et al., *Stochastic models for cell motion and taxis*. Journal of Mathematical Biology, 2004. **48**(1): p. 23-37.
47. Kumar, N., et al., *A high-throughput migration assay reveals HER2-mediated cell migration arising from increased directional persistence*. Biophysical Journal, 2006. **91**(4): p. L32-L34.
48. Maheshwari, G., H.S. Wiley, and D.A. Lauffenburger, *Autocrine epidermal growth factor signaling stimulates directionally persistent mammary epithelial cell migration*. Journal Of Cell Biology, 2001. **155**(7): p. 1123-1128.
49. Stokes, C.L., D.A. Lauffenburger, and S.K. Williams, *Migration of Individual Microvessel Endothelial-Cells - Stochastic-Model and Parameter Measurement*. Journal of Cell Science, 1991. **99**: p. 419-430.
50. Ware, M.F., A. Wells, and D.A. Lauffenburger, *Epidermal growth factor alters fibroblast migration speed and directional persistence reciprocally and in a matrix-dependent manner*. Journal Of Cell Science, 1998. **111**: p. 2423-2432.
51. Parkhurst, M.R. and W.M. Saltzman, *Quantification Of Human Neutrophil Motility In 3-Dimensional Collagen Gels - Effect Of Collagen Concentration*. Biophysical Journal, 1992. **61**(2): p. 306-315.
52. Rabut, G. and J. Ellenberg, *Automatic real-time three-dimensional cell tracking by fluorescence microscopy*. Journal Of Microscopy-Oxford, 2004. **216**: p. 131-137.
53. Dai, L.S., et al., *A fast and robust quantitative time-lapse assay for cell migration*. Experimental Cell Research, 2005. **311**(2): p. 272-280.
54. Martens, L., et al., *Cell_motility: a cross-platform, open source application for the study of cell motion paths*. Bmc Bioinformatics, 2006. **7**: p. 289-294.
55. Arrieumerlou, C. and T. Meyer, *A local coupling model and compass parameter for eukaryotic chemotaxis*. Developmental Cell, 2005. **8**(2): p. 215-227.
56. Pankov, R., et al., *A Rac switch regulates random versus directionally persistent cell migration*. Journal Of Cell Biology, 2005. **170**(5): p. 793-802.

57. Schneider, I.C. and J.M. Haugh, *Mechanisms of gradient sensing and chemotaxis - Conserved pathways, diverse regulation*. Cell Cycle, 2006. **5**(11): p. 1130-1134.
58. Schechter, A.L., et al., *The Neu Oncogene - An Erb-B-Related Gene Encoding A 185,000-Mr Tumor-Antigen*. Nature, 1984. **312**(5994): p. 513-516.
59. Bargmann, C.I., M.C. Hung, and R.A. Weinberg, *Multiple Independent Activations Of The Neu Oncogene By A Point Mutation Altering The Transmembrane Domain Of P185*. Cell, 1986. **45**(5): p. 649-657.
60. Debnath, J., S.K. Muthuswamy, and J.S. Brugge, *Morphogenesis and oncogenesis of MCF-10A mammary epithelial acini grown in three-dimensional basement membrane cultures*. Methods, 2003. **30**(3): p. 256-268.
61. Dunn, G.A., *Characterising a kinesis response; time averaged measures of cell speed and directional persistence*. Agents and actions supplements, 1983. **12**: p. 14-33.
62. Anderson, A.R.A., et al., *Tumor morphology and phenotypic evolution driven by selective pressure from the microenvironment*. Cell, 2006. **127**: p. 905- 915.
63. Deisboeck, T.S., T. Demuth, and Y. Mansury, *Correlating velocity patterns with spatial dynamics in glioma cell migration*. Acta Biotheoretica, 2005. **53**(3): p. 181-190.
64. Quaranta, V., et al., *Mathematical modeling of cancer: The future of prognosis and treatment*. Clinica Chimica Acta, 2005. **357**(2): p. 173-179.
65. Bray, D., *Cell movements: from molecules to motility*. 2nd ed. 2001: Garland Publishing, NY.
66. Ford, R.M. and P.T. Cummings, *On the Relationship between Cell Balance-Equations for Chemotactic Cell-Populations*. Siam Journal on Applied Mathematics, 1992. **52**(5): p. 1426-1441.
67. Ideker, T., *Building with a scaffold: emerging strategies for high- to low-level cellular modeling*. Trends in Biotechnology, 2003. **21**(6): p. 255-262.
68. Keller, E.F. and L.A. Segel, *MODEL FOR CHEMOTAXIS*, in *J Theor Biol*. 1971. p. 225-&.
69. Barton, J.W. and R.M. Ford, *Determination of Effective Transport-Coefficients for Bacterial Migration in Sand Columns*. Applied and Environmental Microbiology, 1995. **61**(9): p. 3329-3335.
70. Duffy, K.J., P.T. Cummings, and R.M. Ford, *Random-Walk Calculations for Bacterial Migration in Porous-Media*. Biophysical Journal, 1995. **68**(3): p. 800-806.
71. Ford, R.M. and R.W. Harvey, *Role of chemotaxis in the transport of bacteria through saturated porous media*. Advances in Water Resources, 2007. **30**(6-7): p. 1608-1617.
72. Lewus, P. and R.M. Ford, *Temperature-sensitive motility of Sulfolobus acidocaldarius influences population distribution in extreme environments*. Journal of Bacteriology, 1999. **181**(13): p. 4020-4025.
73. Lewus, P. and R.M. Ford, *Quantification of random motility and chemotaxis bacterial transport coefficients using individual-cell and population-scale assays*. Biotechnology and Bioengineering, 2001. **75**(3): p. 292-304.
74. Vigeant, M.A.S. and R.M. Ford, *Interactions between motile Escherichia coli and glass in media with various ionic strengths, as observed with a three-dimensional-*

tracking microscope. Applied and Environmental Microbiology, 1997. **63**(9): p. 3474-3479.
75. Luster, A.D., R. Alon, and U.H. von Andrian, *Immune cell migration in inflammation: present and future therapeutic targets*. Nature Immunology, 2005. **6**(12): p. 1182-90.
76. Viswanathan, G.M., et al., *Necessary criterion for distinguishing true superdiffusion from correlated random walk processes*. Physical Review E, 2005. **72**: p. 011111.
77. Bartumeus, F., et al., *Animal search strategies: A quantitative. random-walk analysis*. Ecology, 2005. **86**(11): p. 3078-3087.
78. Sims, D.W., et al., *Scaling laws of marine predator search behaviour*. Nature, 2008. **451**(7182): p. 1098-U5.
79. Tsallis, C., *Levy distributions*. Physics World, 1997. **10**(7): p. 42-45.
80. Shlesinger, M.F., G.M. Zaslavsky, and U. Frisch, *Lévy Flights and Related Topics in Physics*, ed. M.F. Shlesinger. 1995, Berlin: Springer.
81. Shiesinger, M.F. and J. Klafter, *Levy walks versus Levy flights*, in *On Growth and Form: Fractal and Non-Fractal Patterns in Physics*, H.E. Stanley and O. N., Editors. 1986, Martinus Nijhof Publishers: Amsterdam, The Netherlands. p. 279-283.
82. Viswanathan, G.M., et al., *Optimizing the success of random searches*. Nature, 1999. **401**(6756): p. 911-914.
83. Bartumeus, F., et al., *Optimizing the encounter rate in biological interactions: Levy versus Brownian strategies*. Physical Review Letters, 2002. **88**(9).
84. Viswanathan, G.M., et al., *Levy flight search patterns of wandering albatrosses*. Nature, 1996. **381**(6581): p. 413-415.
85. Ramos-Fernandez, G., et al., *Levy walk patterns in the foraging movements of spider monkeys (Ateles geoffroyi)*. Behavioral Ecology and Sociobiology, 2004. **55**(3): p. 223-230.
86. Bartumeus, F., et al., *Helical Levy walks: Adjusting searching statistics to resource availability in microzooplankton*. Proceedings of the National Academy of Sciences of the United States of America, 2003. **100**(22): p. 12771-12775.
87. Levandowsky, M., B.S. White, and F.L. Schuster, *Random movements of soil amebas*. Acta Protozoologica, 1997. **36**(4): p. 237-248.
88. Upadhyaya, A., et al., *Anomalous diffusion and non-Gaussian velocity distribution of Hydra cells in cellular aggregates*. Physica A, 2001. **293**(3-4): p. 549-558.
89. Brockmann, D., L. Hufnagel, and T. Geisel, *The scaling laws of human travel*. Nature, 2006. **439**(7075): p. 462-465.
90. Benhamou, S., *How many animals really do the Levy walk?* Ecology, 2007. **88**(8): p. 1962-1969.
91. Edwards, A., *Using likelihood to test for Lévy flight search patterns and for general power-law distributions in nature*. Journal of Animal Ecology, 2008. **77**(6): p. 1212-1222.
92. Edwards, A., et al., *Revisiting Levy flight search patterns of wandering albatrosses, bumblebees and deer*. Nature, 2007. **449**: p. 1044-U5.

93. Sims, D.W., D. Righton, and J.W. Pitchford, *Minimizing errors in identifying Levy flight behaviour of organisms*. Journal of Animal Ecology, 2007. **76**(2): p. 222-229.
94. Bénichou, O., et al., *Two-dimensional intermittent search processes: An alternative to Lévy flight strategies*. Physical Review E, 2006. **74**(2): p. 4.
95. Li, L., S.F. Nørrelykke, and E.C. Cox, *Persistent cell motion in the absence of external signals: a search strategy for eukaryotic cells*. PLoS ONE, 2008. **3**(5): p. e2093.
96. Bosgraaf, L. and P.J.M. Van Haastert, *The Ordered Extension of Pseudopodia by Amoeboid Cells in the Absence of External Cues*. PLoS One, 2009. **4**(4): p. Article No.: e5253.
97. Van Haastert, P.J.M. and L. Bosgraaf, *Food Searching Strategy of Amoeboid Cells by Starvation Induced Run Length Extension*. PLoS One, 2009. **4**(8): p. Article No.: e6814.
98. Potdar, A.A., et al., *Bimodal Analysis of Mammary Epithelial Cell Migration in Two Dimensions*. Annals of Biomedical Engineering, 2009. **37**(1): p. 230-245.
99. Bosgraaf, L., P.J.M. van Haastert, and T. Bretschneider, *Analysis of Cell Movement by Simultaneous Quantification of Local Membrane Displacement and Fluorescent Intensities Using Quimp2*. Cell Motility and the Cytoskeleton, 2009. **66**(3): p. 156-165.
100. Newman, M.E.J., *Power laws, Pareto distributions and Zipf's law*. Contemporary Physics, 2005. **46**: p. 323-351.
101. Byers, J.A., *Correlated random walk equations of animal dispersal resolved by simulation*. Ecology, 2001. **82**: p. 1680-1690.
102. Cain, M.L., *Random search by herbivorous insects - A simulation-model*. Ecology, 1985. **66**: p. 876-888.
103. Walker, G.M., et al., *Effects of flow and diffusion on chemotaxis studies in a microfabricated gradient generator*. Lab On A Chip, 2005. **5**(6): p. 611-618.
104. Gruver, J.S., J.P. Wikswo, and C.Y. Chung, *3 '-phosphoinositides regulate the coordination of speed and accuracy during chemotaxis*. Biophysical Journal, 2008. **95**(8): p. 4057-4067.
105. Bénichou, O., et al., *Optimal Search Strategies for Hidden Targets*. Physical Review Letters, 2005. **94**(19): p. 4.
106. Maeda, Y.T., et al., *Ordered Patterns of Cell Shape and Orientational Correlation during Spontaneous Cell Migration*. PLoS One, 2008. **3**(11): p. Article No.: e3734.
107. Macnab, R.M. and D.E. Koshland, *Gradient-sensing mechanism in Bacterial Chemotaxis*. Proceedings of the National Academy of Sciences of the United States of America, 1972. **69**: p. 2509-2512.
108. Brown, D.A. and H.C. Berg, *Temporal Stimulation of Chemotaxis in Escherichia coli*. Proceedings of the National Academy of Sciences of the United States of America, 1974. **71**(4): p. 1388-1392.
109. Berg, H.C. and P.M. Tedesco, *Transient-Response to Chemotactic Stimuli in Escherichia-Coli*. Proceedings of the National Academy of Sciences of the United States of America, 1975. **72**(8): p. 3235-3239.

110. Berg, H.C. and E.M. Purcell, *Physics Of Chemoreception*. Biophysical Journal, 1977. **20**(2): p. 193-219.
111. Sai, J.Q., et al., *The IL sequence in the LLKIL motif in CXCR2 is required for full ligand-induced activation of Erk, Akt, and chemotaxis in HL60 cells*. Journal Of Biological Chemistry, 2006. **281**(47): p. 35931-35941.
112. Saadi, W., et al., *Chemotaxis of metastatic breast cancer cells in parallel-gradient microfluidic chambers*. Faseb Journal, 2005. **19**(5): p. A1505-A1505.
113. Saadi, W., et al., *A parallel-gradient microfluidic chamber for quantitative analysis of breast cancer cell chemotaxis*. Biomedical Microdevices, 2006. **8**(2): p. 109-118.
114. Wang, S.J., et al., *Differential effects of EGF gradient profiles on MDA-MB-231 breast cancer cell chemotaxis*. Experimental Cell Research, 2004. **300**(1): p. 180-189.
115. Jeon, N.L., et al., *Generation of solution and surface gradients using microfluidic systems*. Langmuir, 2000. **16**(22): p. 8311-8316.
116. Matthay, M.A., et al., *Transient Effect Of Epidermal Growth-Factor On The Motility Of An Immortalized Mammary Epithelial-Cell Line*. Journal of Cell Science, 1993. **106**: p. 869-878.
117. Price, J.T., et al., *Epidermal growth factor promotes MDA-MB-231 breast cancer cell migration through a phosphatidylinositol 3 '-kinase and phospholipase C-dependent mechanism*. Cancer Research, 1999. **59**: p. 5475-5478.
118. Stein, R.A., et al., *An analytical approach to the measurement of equilibrium binding constants: Application to EGF binding to EGF receptors in intact cells measured by flow cytometry*. Biochemistry, 2001. **40**(20): p. 6142-6154.
119. Maheshwari, G., et al., *Biophysical integration of effects of epidermal growth factor and fibronectin on fibroblast migration*. Biophysical Journal, 1999. **76**(5): p. 2814-2823.
120. Kempiak, S.J., et al., *Local signaling by the EGF receptor*. Journal of Cell Biology, 2003. **162**(5): p. 781-787.
121. Chan, A.Y., et al., *EGF stimulates an increase in actin nucleation and filament number at the leading edge of the lamellipod in mammary adenocarcinoma cells*. Journal of Cell Science, 1998. **111**: p. 199-211.
122. Kim, H.D., et al., *Epidermal Growth Factor-induced Enhancement of Glioblastoma Cell Migration in 3D Arises from an Intrinsic Increase in Speed But an Extrinsic Matrix- and Proteolysis-dependent Increase in Persistence*. Molecular Biology of the Cell, 2008. **19**(10): p. 4249-4259.
123. *American Cancer Society : Cancer Facts and Figures 2008*. 2008, American Cancer Society: Atlanta.
124. Mundy, G.R., *Metastasis to bone: Causes, consequences and therapeutic opportunities*. Nature Reviews Cancer, 2002. **2**(8): p. 584-593.
125. Gupta, G.P. and J. Massague, *Cancer metastasis: Building a framework*. Cell, 2006. **127**: p. 679-695.
126. Quaranta, V. and G. Giannelli, *Cancer invasion: Watch your neighbourhood!* Tumori, 2003. **89**(4): p. 343-348.
127. Marinkovich, M.P., *Laminin 332 in squamous-cell carcinoma*. Nature Reviews Cancer, 2007. **7**(5): p. 370-380.

128. Tripathi, M., et al., *Laminin-332 Is a Substrate for Hepsin, a Protease Associated with Prostate Cancer Progression*. Journal of Biological Chemistry, 2008. **283**(45): p. 30576-30584.
129. Saleem, M., et al., *A novel biomarker for staging human prostate adenocarcinoma: Overexpression of matriptase with concomitant loss of its inhibitor, hepatocyte growth factor activator inhibitor-1*. Cancer Epidemiology Biomarkers & Prevention, 2006. **15**(2): p. 217-227.
130. Hooper, J.D., et al., *Type II transmembrane serine proteases - Insights into an emerging class of cell surface proteolytic enzymes*. Journal of Biological Chemistry, 2001. **276**(2): p. 857-860.